# SENSOR DEVELOPMENT FOR ESTIMATION OF BIOMASS YIELD APPLIED TO MISCANTHUS GIGANTEUS

BY

LEI ZHANG

DISSERTATION

Submitted in partial fulfillment of the requirements
for the degree of Doctor of Philosophy in Agricultural and Biological Engineering
in the Graduate College of the
University of Illinois at Urbana-Champaign, 2011

Urbana, Illinois

Doctoral Committee:

Associate Professor Tony E. Grift, Chair
Professor Alan C. Hansen
Associate Professor Yuguo Chen
Assistant Professor Luis F. Rodr ́guez
James Lenz, John Deere®

# SENSOR DEVELOPMENT FOR ESTIMATION OF BIOMASS YIELD APPLIED TO MISCANTHUS GIGANTEUS

Lei Zhang
Department of Agricultural and Biological Engineering
University of Illinois at Urbana-Champaign, 2011
Dr. Tony E. Grift, Advisor

## ABSTRACT

Precision Agriculture technologies such as yield monitoring have been available for traditional field crops for decades. However, there are currently none available for energy crops such as *Miscanthus Giganteus* (*MxG*), switch grass, and sugar cane. The availability of yield monitors would allow better organization and scheduling of harvesting operations. In addition, the real-time yield data would allow adaptive speed control of a harvester to optimize performance.

A yield monitor estimates a total amount of biomass per coverage area in $kg/m^2$ as a function of location. However, for herbaceous type crops such as *MxG* and switchgrass, directly measuring the biomass entering a harvester in the field is complicated and impractical. Therefore, a novel yield monitoring system was proposed. The approach taken was to employ an indirect measure by determining a volume of biomass entering the harvester as a function of time. The

volume can be obtained by multiplying the diameter related cross-sectional area, the height and the crop density of *MxG*. Subsequently, this volume is multiplied by an assumed constant, material density of the crop, which results in a mass flow per unit of time. To determine the coverage area, typically the width of the cutting device is multiplied by the machine speed to give the coverage area per unit of time. The ratio between the mass flow and coverage area is now the yield per area, and adding GPS geo-references the yield.

To measure the height of *MxG* stems, a light detection and ranging (LIDAR) sensor based height measurement approach was developed. The LIDAR was applied to scan to the *MxG* vertically. Two measurement modes: static and dynamic, were designed and tested. A geometrical *MxG* height measurement model was developed and analyzed to obtain the resolution of the height measurement. An inclination correction method was proposed to correct errors caused by the uneven ground surface. The relationship between yield and stem height was discussed and analyzed, resulting in a linear relationship.

To estimate the *MxG* stem diameter, two types of sensors were developed and evaluated. Firstly, a LIDAR based diameter sensor was designed and tested. The LIDAR was applied to scan *MxG* stems horizontally. A measurement geometry model of the LIDAR was developed to determine the region of interest. An angle continuity based pre-grouping algorithm was applied to group the raw data from the LIDAR. Based on the analysis of the presentation of *MxG* stems in the LIDAR data, a fuzzy clustering technique was developed to identify the *MxG* stems within the clusters. The diameter was estimated based on the clustering result. Four types of clustering techniques were compared. Based on their performances, the Gustafson - Kessel Clustering algorithm was selected. A drawback of the LIDAR based diameter sensor was that it could only

be used for static diameter measurement. An alternative system based on a machine vision based diameter sensor, which supported the dynamic measurement, was applied. A binocular stereo vision based diameter sensor and a structured lighting-based monocular vision diameter estimation system were developed and evaluated in sequence. Both systems worked with structured lighting provided by a downward slanted laser sheet to provide detectable features in the images. An image segmentation based algorithm was developed to detect these features. These features were used to identify the *MxG* stems in both the binocular and monocular based systems. A horizontally covered length per pixel model was built and validated to extract the diameter information from images. The key difference between the binocular and monocular stereo vision systems was the approach to estimate the depth. For the binocular system, the depth information was obtained based on disparities of matched features in image pairs. The features were matched based on a pixel similarity in both one dimensional and two dimensional based image matching algorithm. In the monocular system, the depth was obtained by a geometry perspective model of the diameter sensor unit. The relationship between yield and stem diameter was discussed and analyzed. The result showed that the yield was more strongly dependent upon the stem height than diameter, and the relationship between yield and stem volume was linear.

The crop density estimation was also based on the monocular stereo vision system. To predict the crop density, the geometry perspective model of the sensor unit was further analyzed to calculate the coverage area of the sensor. A Monte Carlo model based method was designed to predict the number of occluded *MxG* stems based on the number of visible *MxG* stems in images. The results indicated that the yield has a linear relationship with the number of stems with a zero intercept and the average individual mass as the coefficient.

All sensors were evaluated in the field during the growing seasons of 2009, 2010 and 2011 using manually measured parameters (height, diameter and crop density) as references. The results showed that the LIDAR based height sensor achieved an accuracy of 92% (0.3m error) to 98.2% (0.06m error) in static height measurements and accuracy of 93.5% (0.22m error) to 98.5% (0.05m error) in dynamic height measurements. For the diameter measurements, the machine vision based sensors showed a more accurate result than the LIDAR based sensor. The binocular stereo vision based and monocular vision based diameter measurement achieved an accuracy of 93.1% and 93.5% for individual stem diameter estimation, and 99.8% and 99.9% for average stem diameter estimation, while the achieved accuracy of LIDAR based sensor for average stem diameter estimation was 92.5%. Among three stem diameter sensors, the monocular vision based sensor was recommended due to its higher accuracy and lower cost in both device and computation. The achieved accuracy of machine vision based crop density measurement was 92.2%.

*To My Family*

# ACKNOWLEDGEMENTS

This research would not have been possible without many people. I would like to give my special appreciation to those who have educated, inspired, and assisted me in this long process.

First, I wish to express my deepest gratitude and acknowledgement to my advisor, Dr. Tony Grift, not only for his expert guidance, invaluable inspiration, and generous contribution throughout the course of my research, but also for his enthusiastic support and encouragement in my life.

I would also like to thank the members of my dissertation committee, Dr. Alan C. Hansen, Dr. Yuguo Chen, Dr. Rodr ǵuez and Mr. James Lenz, for their invaluable comments, assistance and suggestions on this research. Their knowledge and support have greatly improved the quality of this research.

I greatly appreciate Mr. Larry Meyer and Mr. Tim Mies for their assistance during the field experiments. I am especially grateful to the personnel in the main office of the department of Agricultural and Biological Engineering, Mrs. Ronda Sullivan, Mrs. Robin Fonner, Mrs. Jennifer Black and Mrs. Mary Schultze, for their patient and kind assistance during my studies.

My sincere gratitude also goes to my friends, Dr. Zewei Miao, Mr. Fu Ouyang, Mr. Robert Reis, Mr. Ed Roy, Mr. Phil Johnson and Mr. Yanshui Jiang for their cooperation, help and

friendship: I greatly enjoyed working with them. I would also like to give my special thanks to Nanjun for her irreplaceable supports and encouragements.

Last but not the least, I shall be forever indebted to my parents for their everlasting love, understanding and encouragement, and for being the best parents in the world.

# Table of Contents

# LIST OF FIGURES

# LIST OF TABLES

# CHAPTER 1
# INTRODUCTION

The increased concerns regarding the sustainability of non-renewable fossil energy sources, such as oil, natural gas, and coal, have sparked intensified interest in renewable energy sources, such as sunlight, wind, and bioenergy (Chu *et al.*, 2010). The use of large perennial grasses as feedstocks for biofuel development has received considerable attention because of their wide availability and relatively small impact on the food supply (Arthur *et al.*, 2006; Tilman *et al.*, 2006; Orts *et al.*, 2008; Schmer *et al.*, 2008).

*Miscanthus Giganteus(MxG)* (*Fig.* 1.1) is considered a valuable candidate energy crop due to its high yield, the absence of known diseases, low water use and nutritional requirements, its non-invasive nature and its ability to recycle carbon into the soil (Lewandowski *et al.*, 2000, Naidu *et al.*, 2003, Clifton-Brown *et al.*, 2007). Moreover, *MxG* is a rhizomatous C4 grass species with a high carbon dioxide fixation rate. It is an interesting raw material for industrial bioconversion processes given that it is rich in carbohydrates, which constitute approximately 75% of the dry matter content (Brosse *et al.*, 2009). Among the 15 cultivars of Miscanthus, *MxG* is the most widely cultivated Miscanthus cultivar for commercial production of lignocellulosic biomass. It is currently used in the European Union and United Kingdom as a commercial

energy crop. *MxG* produces more biomass overall than comparable crops, as well as more biofuel products. For example, a 435.6 square meters (one acre) of corn yields around 7,600 kg of grain and 2,862 liters of ethanol. *MxG* is capable of producing up to 20,000 kg of biomass and 12,303 liters of ethanol fuel. Another major benefit of *MxG* is that it is not a food crop. Corn-based ethanol in contrast is based on creating fuel from a product that could be used to feed people and animals. When market forces change the demand for food related crops like corn, prices can fluctuate heavily, affecting the ability of many to purchase food. Since *MxG* is not a food crop, changes in demand will not have a direct effect on the price of food (Paine *et al.* 1996) especially since it can be grown on marginal lands.

**Figure 1.1. *MxG* in the field showing the stem structure and an absence of leaves during the harvesting season.**

Currently, a yield monitoring is non-existent for *MxG*. If it were available, processes such as transportation could be better organized and scheduled, and the variability within or among fields could be measured. Especially in large farms, a yield monitor may remove the manager

from the everyday harvesting operations (Price *et al.*, 2007). In addition, the real-time yield data would allow adaptive speed control of a harvester to optimize performance.

## 1.1 Yield Monitoring Systems

Various approaches based on field measurement and as well as remote sensing have been applied in yield monitoring systems (Lu, 2006). Among these, field measurements are most accurate, but they are limited to a single measurement per season at harvesting time. Remote sensing can provide the spatial distribution of biomass, with a relatively high temporal resolution, synoptic representation where the data is compressed into yield levels, and digital format. However, its accuracy is relatively low compared to direct field measurements. Thus, the combination of field measurement and remote sensing system can provide large-area biomass yield information with high accuracy.

Existing field measurement based yield monitoring systems are mostly indirect. For example, combine harvesters use an impact plate measurement to monitor the yield of grains. The material collides with an impact plate that is fixed on a spring and the deflection of the spring is used as a measure of the mass flow. Other types of combine harvesters use a radiation interruption mechanism to measure the flow of grain. A constant level of radiation is received in the absence of a mass flow, and an intensity decrease is measured which is proportional to the mass flow density. The elevator method is also a solution to measure the biomass yield. This method is based on the volume of grain, which is measured on the paddles of a combine elevator during transportation of grain to the grain tank. However, most of the methods mentioned above are based on analog sensor outputs, which makes them susceptible to vibration, contamination, alignment and temperature drift problems, as well as requiring frequent calibration (Grift, 2003).

For cotton, researchers developed and tested several yield monitors (Durrence *et al.*, 1998; Sassenrath-Cole *et al.*, 1999; Thomasson *et al.*, 1999; Wolak *et al.*, 1999; Vellidis *et al.*, 2003). Some have been commercialized under brand names such as AgLeader (Ames, Iowa), FarmScan (Perth, Western Australia), Micro-Trak (Eagle Lake, Minn.), and Zycom/AGRIplan (Stow, Mass.). Most of these yield monitors use the principle of photo interruption where light attenuation caused by passing cotton particles is measured to estimate the cotton mass flow (Thomasson *et al.*, 2006). Thomasson and Sui (2004) and Sui *et al.* (2004) designed an optical reflectance based mass flow sensor, which was comprised of a unilaterally mounted light source and optical sensors. This design eliminated the requirement for alignment of the sensors.

Yield monitors for other crops like sugar cane and peanuts were also researched. Benjamin *et al.* (2001) discussed a yield monitoring system, which could be fixed on a Cameco sugar cane combine, and a mass scale was applied as a yield sensor. Price *et al.* (2007) developed an optical yield monitor for sugar cane using three optical sensors that were located in the floor of a conveyer. Vellidis *et al.* (2003) developed a peanut yield monitoring system based on load cells to measure the mass. A similar method can also be found in the research of Domingos *et al.* (2005). Their system consisted of a load-cell based scale, which was mounted in the floor of the elevator of a CASE sugarcane combine. In fruit harvesting, a machine vision approach was used to estimate the yield of citrus per tree (Schueller *et al.*, 1999; Whitney *et al.*, 2001; Annamalai *et al.*, 2004). Grift *et al.* (2006) also applied optical sensors to estimate the fruit yield. Their approach was based on a statistical model.

An alternative to field based yield monitoring is remote sensing based yield monitoring. Remote sensing based systems are focused on the above ground biomass (AGB). Liu *et al.* (2010)

developed an approach to integrate crop stressors and crop descriptors derived from optical remote sensing data with a radiation efficiency model. Becker *et al.* (2010) combined a daily surface reflectance dataset developed from NASA's MODerate resolution Imaging Spectro-radiometer (MODIS) with detailed crop statistics to develop an empirical, generalized approach to forecast wheat yields.

## 1.2 Research Objectives and Overview

Based on the morphological properties (stalk diameter, height and stalk density) of *MxG*, which include stalk diameter, crop height and the stalk density, the yield was estimated using the equation:

$$Y = d * \pi \left( \frac{D}{2} \right)^2 * H * \rho \qquad (1.1)$$

Where Y is the estimated yield in the unit of $\frac{kg}{m^2}$, $d$ is the density in number of stems per area ($\frac{\#}{m^2}$), $D$ is the estimated average stem diameter in $m$ and $H$ is the estimated average height in $m$ of the crop and $\rho$ is the material density of the crop in $\frac{kg}{m^3}$.

The purpose of this research was to develop sensors for a yield monitoring system applied to *MxG*. The developed sensors measured morphological properties of *MxG* (stalk diameter, crop height and the stalk density). Redundant measurements (sensors) were developed and evaluated in a field environment and they were compared based on performances and costs of sensors. All measurements were automatic and fully digital. In addition, relationships between measured

morphological parameters and yield were discussed and analyzed. The developed sensors will be suitable to estimate the yield and to monitor the instantaneous growth stage of *MxG*.

**Chapter 1. Introduction**

The purpose and motivation of this research is introduced in this chapter. The concept of yield monitoring technique is discussed, and an overview of the research is given.

**Chapter 2. Light detection and ranging (LIDAR) based plant height measurement**

This chapter describes the development of a real-time measurement sensor to estimate the height of *MxG* under field conditions. A SICK® LMS 291 laser scanner was applied to vertically scan to the *MxG* to collect data. Two measurement modes, static and dynamic height measurement were described in sequence.

The LIDAR measured the height at a fixed location in the static height measurement mode. The height estimation was based on the detected ground level, which was obtained by a developed ground level generation algorithm. The static height measurement approach was evaluated under various crop densities. To further evaluate the static height measurement, it was also employed to estimate the crop height in a 5m x 10m field.

The LIDAR traveled along the crop at a constant velocity in the dynamic height measurement. The measurement provided a three dimensional structure of the *MxG* field with the integration of velocity information. An Ordinary Least Squares based surface fitting algorithm was applied to generate both the top and ground surfaces of the coverage area resulting in an average crop height. To reduce the error caused the uneven ground surface, an inclination correction

algorithm was developed and shown to improve the accuracy for both static and dynamic height measurements. A height-based yield model of *MxG* was introduced and analyzed.

**Chapter 3. A real-time LIDAR based plant stem diameter sensor**

The objective in this chapter is to develop a real- time LIDAR based sensor to measure stem diameters in a certain area. A LIDAR was used to scan to *MxG* horizontally. The principle of the laser scanner was based on projecting a laser sheet from a commercial LIDAR unit that was intercepted by the *MxG* stems. The angles and distances from the sensor to the stems were obtained as real-time data sets. Each stem caused multiple reflections, and the challenge was to separate the stems in the signals.

To solve this problem, a region of interest (ROI) was firstly defined based on a stem diameter measurement model. The data in the ROI was grouped into sets that contained single stems and sets that contained multiple stems based on their angle continuity. The presentation of *MxG* stems in LIDAR data was discussed and analyzed, based on which a clustering algorithm was applied to separate the multiple stem data sets into single stem data sets. Subsequently, the diameter information was extracted based on a geometric model of *MxG* stems. Four classic clustering algorithms were tested, among which the Gustafson - Kessel Clustering algorithm showed the best performance. The developed method was tested and evaluated in the field.

**Chapter 4. A stereo vision based stem diameter sensor**

The LIDAR based stem diameter measurement in chapter two was limited by a small coverage area, lower accuracy and absence of dynamic measurement support. To better estimate the stem diameters, a binocular stereo vision based high-accuracy diameter sensor for *MxG* was developed and described in this chapter.

Two Unibrain® Fire-i 701c industrial real-time cameras were employed in combination with a downward slanted laser sheet that provided structured lighting. The observed locations where the laser sheet intercepted the *MxG* stalks were used as features in stereo images. Subsequently, the features present in dual images were paired to identify *MxG* stems. Two models were analyzed and tested in experiments: Firstly, a disparity-depth model was used to predict the depth between the cameras and targets (*MxG* stems). Secondly, to estimate the stalk diameter from images, the horizontal covered length per pixel, which varies depending on depth, is required. A depth - horizontally covered length per pixel model, which calculated the horizontally covered length of a pixel based on depth information, was analyzed and validated by experiments. The captured images were white balanced and converted to an RGB color space. A segmentation-based feature detection algorithm was developed to select the features in images. An image matching algorithm, which compared the pixel similarity between image pairs in both one dimensions and two dimensions, was developed to match the same features in the image pairs. The stem diameters were estimated based on the size of detected features, estimated depth and horizontal covered length per pixel. Both depth and diameter estimation were evaluated in the field.

**Chapter 5. A monocular vision based stem diameter sensor**

A novel stereo vision based diameter sensor was introduced in this chapter. Instead of applying binocular stereo vision as described in chapter four, which were relative expensive in both computation and hardware, a monocular vision based 3D diameter measurement system was developed. The principle is similar to the sensor applied in chapter four, but here only one camera was applied. The sensor was composed of an industrial CCD camera and a laser source.

The camera captured real-time images in the YCrCb space, while the laser source provided structured lighting, imposing features for depth estimation and *MxG* stem identification. The captured images were white balanced and converted to the RGB space. A segmentation based method was proposed to detect the features in the images. The depth information of each identified *MxG* stem was extracted based on a perspective model of the diameter sensor unit. Based on the depth - horizontal covered length per pixel model the diameter of *MxG* stems were estimated. Both the sensor unit geometry perspective and the depth – horizontal covered length per pixel model were validated using experiments and mathematical analysis. The proposed method was evaluated in the field.

The relationship between yield and stem diameter was introduced and discussed. The result showed that this relationship is not trivial, mainly because the yield is more strongly dependent upon stem height than diameter. Subsequently, the relationship between a combination of stem height and diameter (stem volum) was further discussed. The result indicated that yield and stem volume followed a linear relationship.

**Chapter 6. A machine vision based crop density sensor**

The objective in this chapter was to develop a crop density sensor for *MxG* to predict the stem density in a certain area. A novel machine vision based crop density sensor for *MxG* is described, where the same sensor module as in chapter four and five was applied.

The sensor coverage area was calculated based on the geometry perspective model of the sensor module, which was introduced in chapter five. The visible *MxG* stems in images were detected using a segmentation based algorithm. A Monte Carlo model was used to predict the number of invisible stems in the image based on the number of detected visible stems. The

model was validated using lab and field experiments. The result showed that sensor provides more accurate estimations for lower crop densities compared to higher crop densities. A crop density based yield model was analyzed based on *Eqn.* 1.1 to uncover the relationship between yield and number of stems. The model was based on manually collected field data. The result showed that the relationship between the yield and the number of stems is linear with zero intercept and the average mass of individual stems as the coefficient.

## Chapter 8. Summary of conclusions and future research direction

The conclusion of this research and the recommended research direction of the future work is described in this chapter.

# CHAPTER 2
# LIGHT DETECTION AND RANGING (LIDAR) BASED PLANT HEIGHT MEASUREMENT

## 2.1 Introduction

The average crop height is considered an important morphological parameter of *Miscanthus Giganteus* (*MxG*), since it is directly related to biomass yield (Zub *et al.*, 2011). In addition, it can be used to identify the genotype of *MxG* (Clifton-Brown and Lewandowski, 2002). Historically, this height information was captured primarily using manual measurements.

This research focused on the development of a laser scanner (LIDAR) based real-time height sensor for *MxG*. With the availability of real-time height sensors, a yield monitoring system for *MxG*, which estimates a total amount of biomass per coverage area as a function of location, becomes possible. Direct measurement of the biomass entering a harvester in the field for herbaceous crops such *MxG* is impractical. A real-time height sensor provides an indirect measure of biomass by relating the biomass yield to the average crop height, individual stem diameter and crop density being the number of stems per coverage area. A GPS can geo-reference the yield to produce a yield map. The stem diameter and crop density sensor will be reported on in subsequent chapters.

Height measurement techniques are widely researched in forestry. Ulander *et al.* (1995), Dammert and Askne (1998) and Shimada *et al.* (2001) applied Synthetic Aperture Radar (SAR) to estimate the height of trees. In their methods, the phase difference among the trees and tree models was used to estimate the height of trees. However, these methods were environment dependent and the devices (SAR) were relatively expensive. Alternatively, image processing and machine vision based methods were employed to measure the height of trees. Cai and Walker (2010) presented a monocular vision based tree height measurement method. A camera was mounted on an unmanned aerial vehicle to capture top view images of trees. The depth information was reconstructed by dynamic programming with an explicit occlusion modeling algorithm. The reported achieved error was within 1.1-1.8 m. In addition, research was conducted on tree height estimation using a LIDAR system. Magnussen *et al.* (1999) estimated tree heights based on a recovery model using an airborne LIDAR. Persson *et al.* (2002) described a tree height measurement method using an airborne LIDAR system as well. The height of trees was estimated by creating a digital terrain model and a digital canopy model. The measurements from this method had a root mean square error of 0.63 m. Kwak *et al.* (2007) developed a tree height estimation method based on an airborne LIDAR system. A morphological image analysis method was applied to a digital canopy model to detect treetops, and a watershed segmentation method was applied to delineate individual trees. The reported root mean square error was in the range of 1.13-1.32m. Yamamoto *et al.* (2010) used a small footprint airborne LIDAR based estimation method of mean tree height. The error of this method was within 1m. Methods combining a LIDAR system with a machine vision system to measure the height of trees were also reported on (St.-Onge 2004, 2008).

One of the complications of this research compared to the references mentioned was that the plant height, such as that of *MxG* is not as high as trees, which demanded higher accuracy. In addition, the coverage area was much smaller than those found in forestry were. These differences showed that the referenced methods did not meet the needs of *MxG* height measurement in terms of technology, costs and accuracy. Therefore, a ground based 2D laser scanner was applied to estimate the height of *MxG*. The applied device was similar to the approach used by Jaakkola *et al.* (2010) who applied a laser scanner to develop a mapping system for tree measurement and Van der Zande *et al.* (2006), who reconstructed the tree structure using a laser scanner as well. The objective of this research was to develop a low-cost and high-accuracy height measurement system for *MxG* in the field as part of a yield monitoring system.

## 2.2 Materials

A SICK® Laser scanner (LMS 291) was applied to scan vertically to estimate the height of the *MxG* plants. The laser scanner (*Fig.* 2.1(a)) consisted of a 905nm infrared radiation source, a scanner, which carries a plane mirror and provides 180 or 100 degrees view, and receiver electronics, which capture the reflected signals sent from the infrared source to obtain distance information. The applied laser scanner features a 180/100 degree view, up to 80 meters operating range, and 0.25 or 0.5 degrees of angular resolution. Its systematic error was ±35 mm, and the statistical error was 10 mm. In this research, the laser scanner was configured for a 180 degree view, eight meters operating range, and an angular resolution of 0.5 degrees.

A computer (Panasonic TOUGHBOOK CF-30, Intel® CoreTM 1.6GHz, with 1.0GB of RAM, 80GB hard disk) was applied to configure the laser scanner and capture data. A

Matlab/C++ application (*Fig.* 2.1(b)) was developed for data acquisition. A serial port facilitated the communication between the laser scanner and the computer. Experiments were conducted in *MxG* fields (*Fig.* 2.1 (c)) Champaign, Illinois (lat/lon: 40.042455,-88.237943) during the spring of 2010.

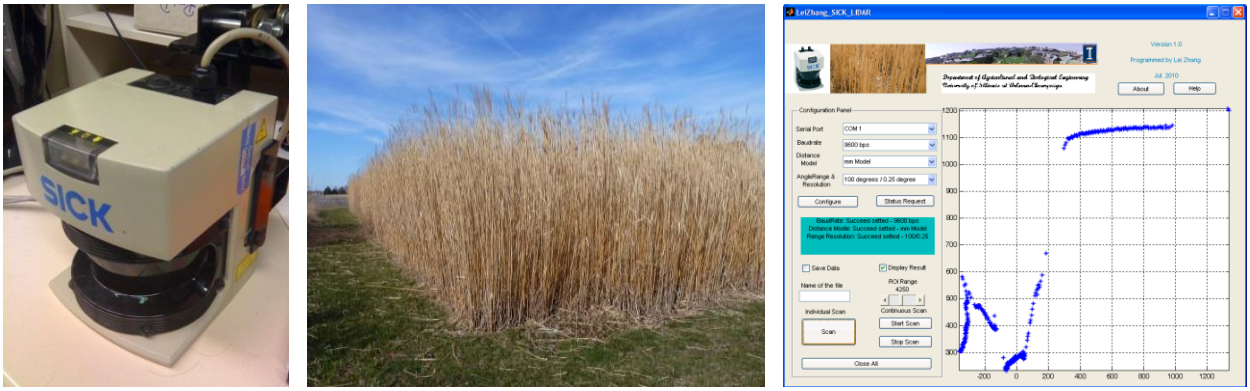


(a) (b) (c)

**Figure 2.1. Materials applied in this research. (a) SICK® LMS 291 laser scanner, which was applied to measure the height of *MxG*. (b) Height measurement methods were evaluated in this experiment field. (c) User interface of the Matlab/C++ application developed to collect data.**

## 2.3 Methodology

To estimate the height of the *MxG* plants, two experimental arrangements being static and dynamic height measurement, were used. The laser scanner was placed statically to measure the height in static height measurement, while the laser scanner moved with a constant velocity during data capture in dynamic height measurement mode. The static mode was designed for pre-harvest height measurement while the dynamic height measurement was used to measure the height during harvesting.

### 2.3.1 Data acquisition

The SICK® LMS291 laser scanner used a telegram to communicate with a computer. The computer sent commands to the laser scanner, and the laser scanner responded using messages. Figure 2.2. (a) shows the data output syntax of the laser scanner.

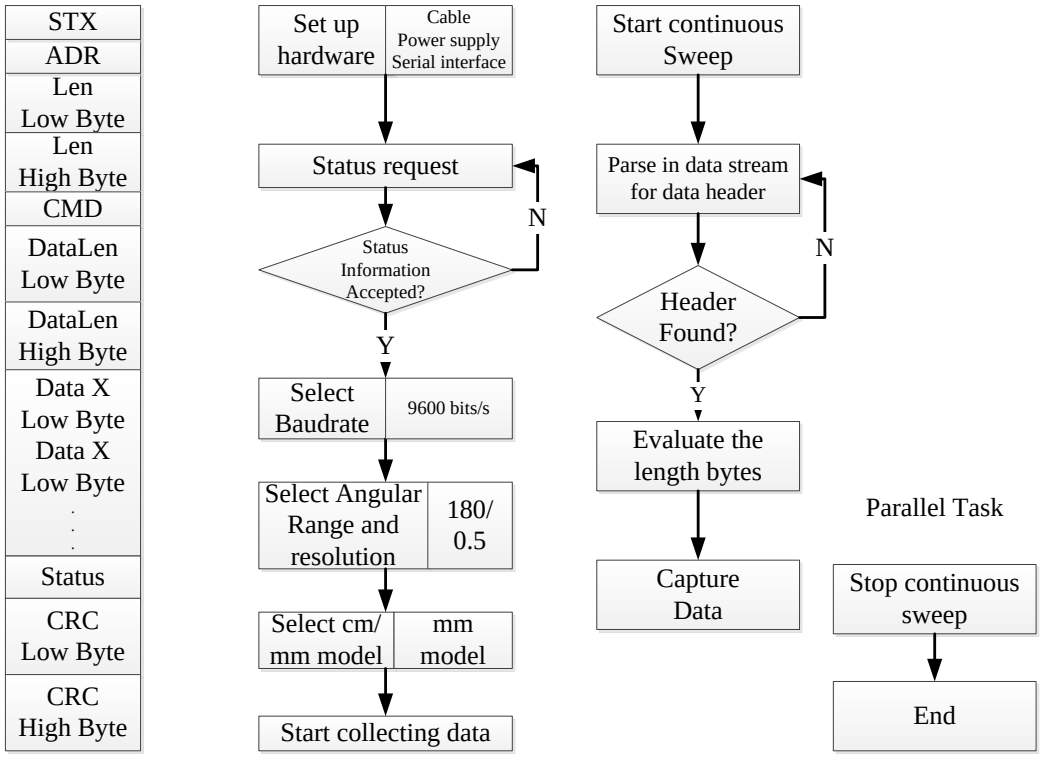


**Figure 2.2. Output data syntax of laser scanner, and procedures of test and data acquisition under continuous model. (a) Data output syntax of the laser scanner. (b) Configuration and test procedures. (c) Procedures to capture data with a continuous sweep model.**

STX represented the start byte, which was 8 bits length. The value of STX was 02 in hexadecimal notation and ADR was the 8-bit address of the computer. Len denoted the 16-bit length of the LMS output data string. CMD was the command byte, which indicated the laser scanner working in individual sweep mode (single scan per time unit) or continuous sweep mode (multiple scans per time unit). DataLen represented the number of measurement data bytes depending on the measurement mode, in this case 361. STX, ADR, Len, CMD, and DataLen

assembled the header of the laser scanner output data. Data X (ranging from 1 to 361) represented the number of data bytes (2 bytes per measurement). The status byte indicated system errors, and CRC represented the result of the cyclic redundancy check.

The laser scanner was configured and tested using the following procedures: (1) Set up the hardware devices including cables, power supply and serial interface. (2) Test with status request. (3) Select the communication baud rate (9600bit/s). (4) Select angular range and resolution (180 degrees range with a resolution of 0.5 degrees). (5) Select cm/mm model (mm model was selected). Figure 2.2. (b) shows the settings applied. Subsequently, the data request command was sent, and data collection commenced.

The data collection in individual sweep mode was straightforward: the data were sent out after receiving the data request command. For the continuous sweep model, because there were multiple frames, their header needed to be identified. Figure 2.2. (c) shows the procedures of data acquisition in the continuous sweep mode. The static height measurements were executed in individual sweep mode, and the dynamic height measurements were executed in continuous sweep mode.

### 2.3.2 Static height measurement

For static height measurement, the laser scanner was used vertically to scan the *MxG* plants. The data consisted of sampling points in polar coordinates with the laser scanner as the origin. While the operating range of the laser scanner can achieve 80 meters (8 meters in this application), the scan angles are not continuous. Therefore, increasing the operating range will lead to reduced tangential resolution. In addition, the tangential resolution is related to the scan

angle. Figure 2.3. shows a geometric representation of the *MxG* height measurement. *Eqn.* 2.1 shows the relationship between the tangential resolution, elevation angle, and operating range.

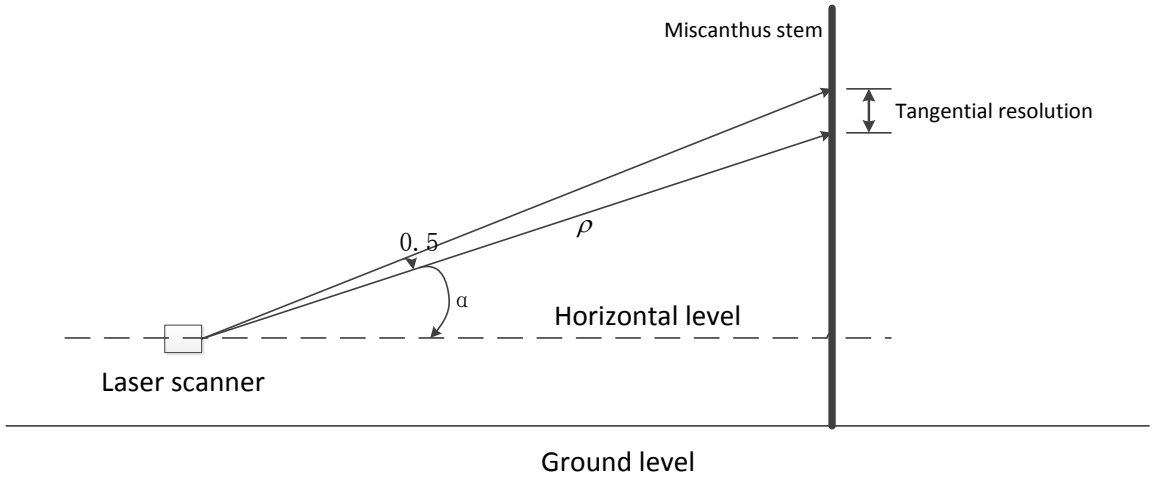


**Figure 2.3. Geometric model of *MxG* height measurement. The tangential resolution of height measurements was a function of the measured distance, measurement angle and the angle resolution.**

$$R_T = \frac{\rho \cdot \cos(a)}{\tan(a+0.5)} - \rho \cdot \sin(a) = \rho\left(\frac{\cos(a)}{\tan(a+0.5)} - \sin(a)\right) \quad (2.1)$$

Where $R_T$ is the tangential resolution in m, $\rho$ is the measured distance in m, and $a$ is the elevation between a horizontal datum and the corresponding scan line in degrees.

The laser scanner will represent objects exceeding the operating range as the maximum distance in the operating range (eight meters). A distance filter was applied to remove objects measured at a distance greater than eight meters. The remaining points were considered valid as shown in *Eqn.* 2.2 .

$$S_{filtered}\{P(\rho,\theta)\} = S_{original}\{P(\rho,\theta)\,|\,\rho < Thres\} \quad (2.2)$$

Where $\rho$ (in m) and $\theta$ (in degree) are the radius and polar angle of a sample point $P$ in polar coordinates. $S_{filtered}$ and $S_{original}$ represent the filtered data set and the original data set. Subsequently, the coordinates of the filtered sample points were converted from polar coordinates to Cartesian coordinates using the following equation:

$$\begin{cases} x = \rho \cos\theta \\ y = \rho \sin\theta \end{cases} \quad (2.3)$$

Where $(x, y)$ are the coordinates of a sampling point in Cartesian coordinates. Under ideal measurement conditions, the central scanning line was perfectly horizontal (*Fig.* 2.4(a)). In this case, the sum of the measured height $H_1$ and the installation height of the device $h_{dev}$ is equal to the true height $H$. However, if the laser scanner is placed at a downward slope (*Fig.* 2.4(b)), $H_1$ will become $H_2$, which is larger than $H_1$. This will lead to an estimated height $H_2 + h_{dev}$ which is larger than the true height $H$. Similarly, if the laser scanner is placed upward sloping (*Fig.* 2.4(c)), this will lead to an estimated height $H_3 + h_{dev}$, which is smaller than the true height.

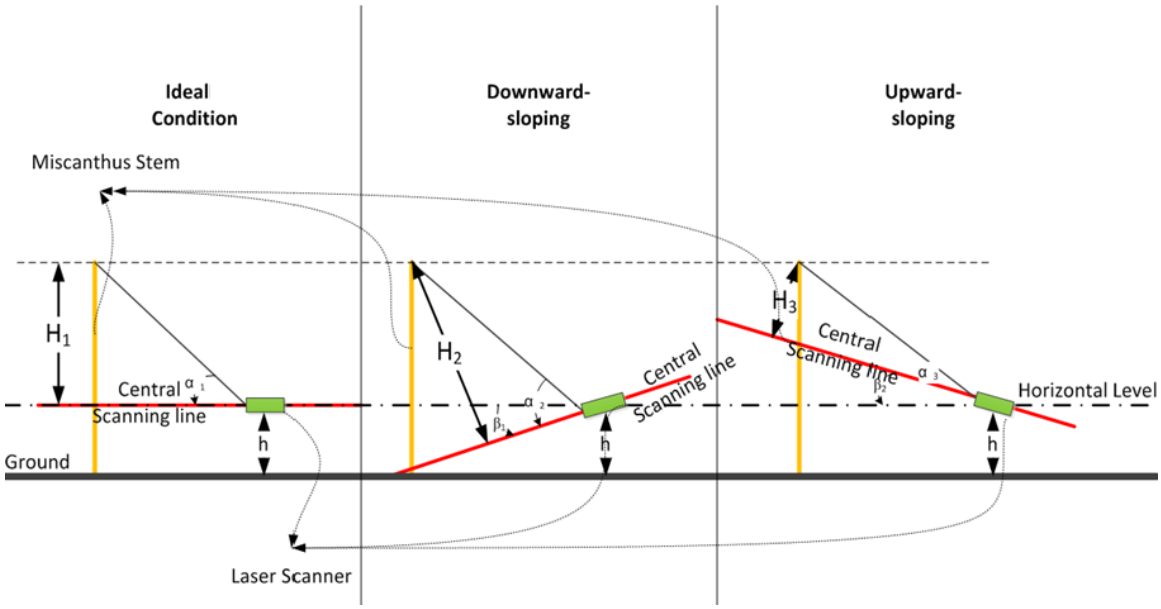


(a) (b) (c)

**Figure 2.4. Inclination influence of the device installation. A downward sloping placed laser scanner will cause a larger measured height, and an upward sloping placed laser scanner will result in a smaller measured height.**

To reduce the error caused by the inclination mentioned above, a correction algorithm was developed. The lower half of the data set that contained ground information was selected from the original sample points.

$$S_{LH} = \{P(\rho,\theta)\} = S_{filtered}\{P(\rho,\theta) \mid \theta \le 90\} \quad (2.4)$$

Where, $S_{LH}$ is the lower half of the filtered data set. The points in $S_{LH}$ were divided into subgroups, which contained 10 samples each, as shown in *Eqn.* 2.4

$$S_{LHi} = S_{LH}\{P(\rho,\theta) \mid 10(i-1)+1 \le \theta \le 10(i-1)+10\} \quad (2.5)$$

Where $S_{LHi}$ denotes the $i_{th}$ subgroup of $S_{LH}$, and $i = 1,2,3...9$.

The difference $D_i$ between the maximum ordinate ( $y_{\max}$ ) and the minimum ordinate ( $y_{\min}$ ), was calculated in each $S_{LHi}$ .

$$D_i = \max(y_i) - \min(y_i), P(x_i, y_i) \in S_{LHi} \quad (2.6)$$

If $D_i$ is smaller than a threshold (150mm), the corresponding subgroup was considered the ground referenced data set. Then, the mean value $E_i$ of all sampling points in the selected ground related data sets was calculated.

$$E_i = \frac{\sum y_i}{10}, P(x_i, y_i) \in S_{GR} \quad (2.7)$$

Where $S_{GR}$ is the selected ground related sample sets.

If the difference between $y_i$ and $E_i$ was larger than the threshold (150 mm) this point was removed from $S_{GR}$ . Subsequently, the mean value of the remaining points was calculated again using *Eqn.* 2.6 and the process was repeated until the difference between every $y_i$ and $E_i$ was smaller than the threshold (150mm). The remaining sampling points were considered ground reference points. An ordinary least squares based line-fitting algorithm was applied to these points to generate a fitted line. The angle between the fitted line, $L_{GND}$, and the horizontal level was considered the inclination (β, deg.). The error caused by this inclination was corrected by rotating all sample points through β degrees. Figure 2.52.5shows two examples of the sample points before and after inclination correction.

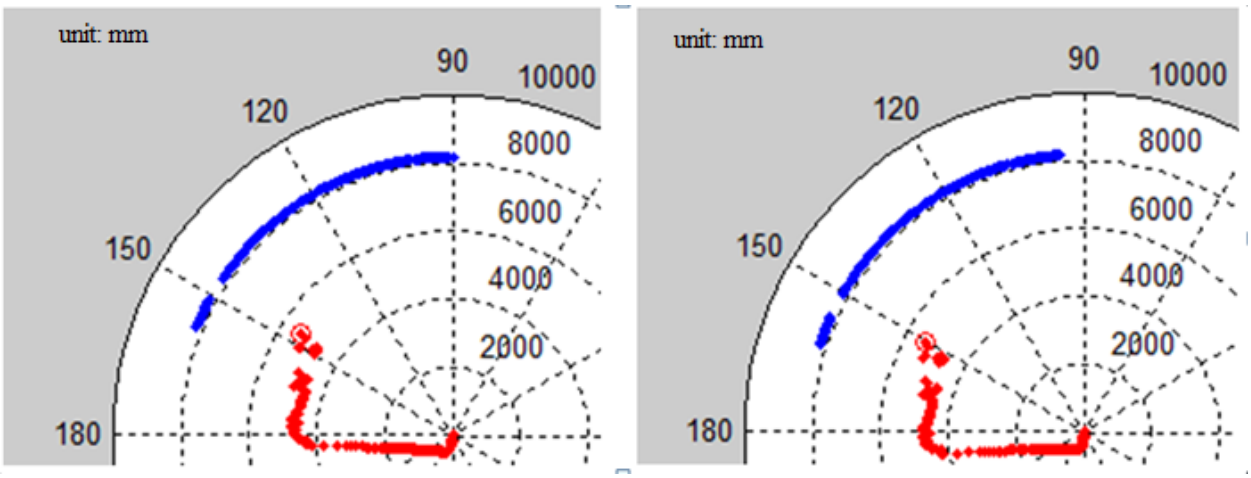


(a) (b)

**Figure 2.5. Sample sets of laser scanner with and without inclination correction. (a) Sample set without inclination correction. (b) Same sample set with inclination correction.**

The maximum ordinate ( $y$ ) was selected from the coordinates of the filtered data set, $S_{filtered}$, to estimate the height of *MxG* as follows:

$$h_{max} = \max(y_i), P(x_i, y_i) \in S_{filtered} \quad (2.8)$$

Where $y_i$ is the ordinate value of sample points within $S_{filtered}$ in Cartesian coordinates.

The estimated height of *MxG*, $H$, was defined as:

$$H = h_{max} + h_{dev} \quad (2.9)$$

The installation height $h_{dev}$ in m, was defined as the distance between the laser scanner and the ground, which was calculated using the following equation:

$$h_{dev} = \frac{|b|}{\sqrt{k^2 + b^2}} \quad (2.10)$$

Where $k$ and $b$ are the slope and vertical intercept of $L_{GND}$. ( $L_{GND} : y = kx + b$ )

### 2.3.3 Dynamic height measurement

In dynamic height measurement, the laser scanner moved at a constant velocity and operated in continuous sweep mode. The captured data were separated into frames based on the output format syntax of the laser scanner. Each individual frame was processed following the same procedure as in static height measurement. All the captured points were presented in three-dimensional coordinates corresponding to the velocity information.

Assume that in time $T$, $n$ frames were captured, and the velocity of the laser scanner was $v$. Thus, there were $361*n$ sample points in a distance of $T*v$ since there were 361 sample points in each frame. The distance between each sample point was therefore $\frac{T*v}{361*n}$. The $N_{th}$ sample point could be represented as $(x_N, y_N, N*\frac{T*v}{361*n})$ in three-dimensional coordinates with the initial point of the laser scanner as the origin: $x_N, y_N$ are Cartesian coordinates of this sample point in each frame that were calculated using *Eqn.* 2.2 .

As in the static height measurement, the highest point in each frame was considered the estimated height measurement. Among $n$ frames, $n$ estimated height measurements were extracted. Based on these points, a cubic interpolation was used to fit a height related surface. The ground-referenced points, obtained using the method described in the static height measurement, were used to fit a surface representing the ground surface. The average distance between the two fitted surfaces was considered the average height in the coverage area. The coverage area was calculated using the following equation:

$$S_M = (\max(x_i) - \min(x_i)) * (\max(y_i) - \min(y_i)) \quad (2.11)$$

Where $S_M$ is the measured area, and $(x_i, y_i, z_i)$ are the coordinates of the height related sample points in 3D.

Figure 2.6, shows how the crop height in the coverage area was estimated using the average distances between the height related surface and the ground related surface. Distances of estimated height sample points to the laser scanner were obtained using their $y$ coordinates, and the tangential resolution was obtained using *Eqn.* 2.1

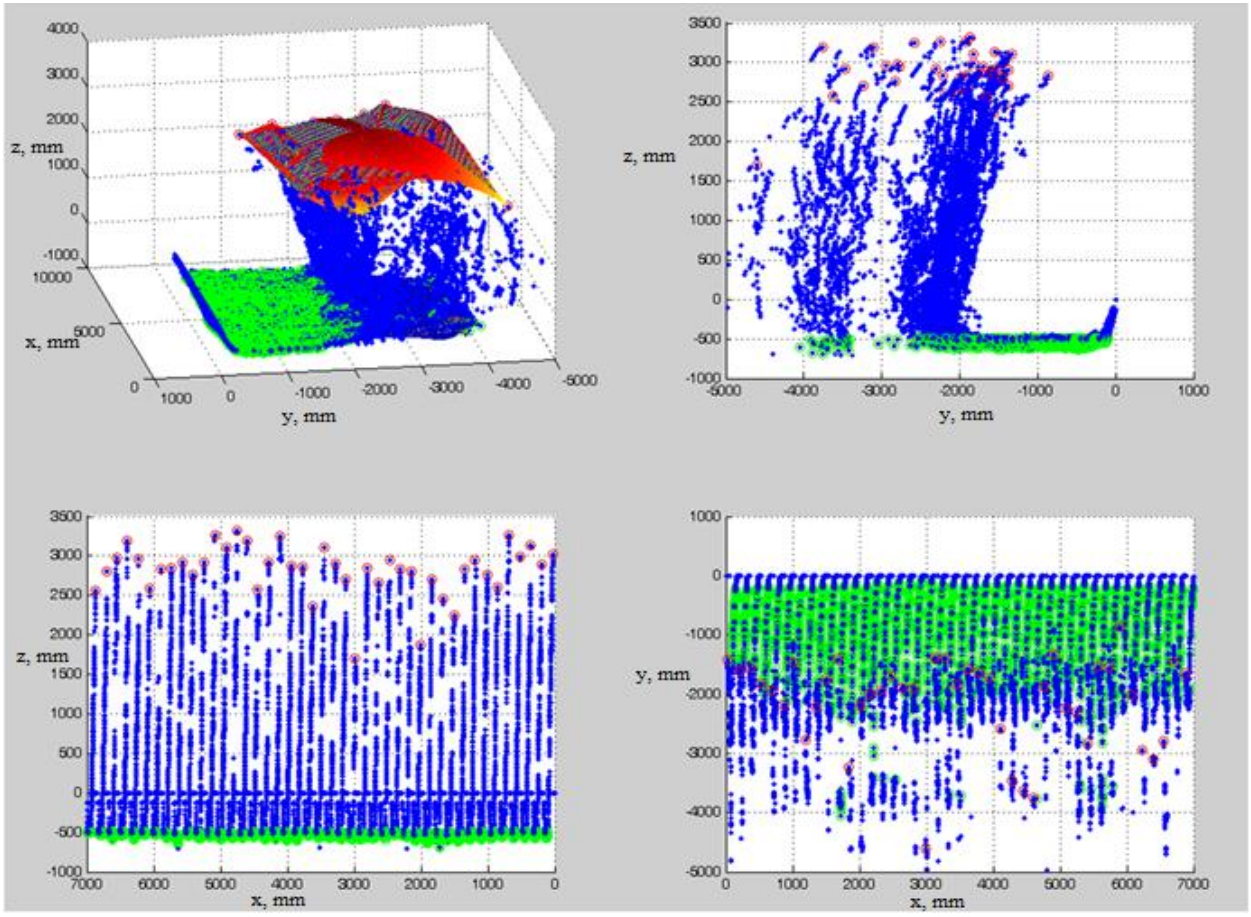


**Figure 2.6. Example of dynamic height measurement result. Upper left: 3D view of the measurement: The upper surface is the height related surface (red), and the lower surface is the ground related surface (green). Upper right, lower left and lower right: Side view, front view and the top view of the measurement.**

## 2.4 Results and Discussion

The methods employed were tested and evaluated in a *MxG* field (*Fig.* 2.1(b)) at Champaign, Illinois (lat/lon: 40.042455,-88.237943), in the spring and fall 2010. The static and dynamic height measurements are described in sequence, and a *MxG* stem height based yield model is discussed in this section as well.

### 2.4.1 Results of static height measurement

To evaluate the static height measurement approach, experiments were conducted using *MxG* fields of varying crop density ranging from 42 stems/$m^2$ to 85 stems/$m^2$. The measurement was repeated five times for each crop density, and the average of these measurements was considered the estimated height. 10 stems were randomly chosen in each field, and the average of their manually measured heights was used as a reference to evaluate the measurement results.

**Table 2.1. Static height measurement results on different crop densities.**

| Crop Density (stems/$m^2$) | Manually Measured Height (m) | Estimated Height (m) | Average Tangential Resolution (m) | Error (m) (%) | Standard Deviation (m) |
|---|---|---|---|---|---|
| 42 | 3.06 | 2.94 | 0.05 | 0.12 (4%) | 0.08 |
| 58 | 3.68 | 3.51 | 0.06 | 0.17 (4.6%) | 0.19 |
| 62 | 3.66 | 3.36 | 0.06 | 0.30 (8%) | 0.08 |
| 74 | 2.75 | 2.57 | 0.04 | 0.18 (7%) | 0.20 |
| 85 | 3.31 | 3.25 | 0.06 | 0.06 (1.8%) | 0.10 |

The results as shown in *Tab.* 2.1 indicate that the method is independent of the crop density in the range of experimental crop densities (42 stems/$m^2$ to 85 stems/$m^2$). The approach used can achieve an estimated accuracy of 94.92% on average with the lowest accuracy of 92% and the highest of 98.2% compared to manually measured heights. The standard deviation of each measurements shows that the difference between each measurement and their mean value is smaller than 0.2m.

To verify the performance of the inclination correction algorithm, results with and without inclination correction were compared. The inclination correction approach improved the estimated accuracy across all crop densities by an average of 4.5% (0.15m) and a maximum of 11.6% (0.34m) (*Tab.* 2.2). The improvement is mainly related to the flatness of the ground: Based on the observation, the improvement by the inclination correction algorithm is less obvious when the ground is relatively flat, such as the experiment conducted at a crop density of 74 stems/$m^2$ in contrast to the experiment conducted at a crop density of 42 stems/$m^2$. In addition, the system installation error was rectified by the inclination correction algorithm improving the results further, as shown in *Fig.* 2.4.

**Table 2.2. Height estimation results with and without inclination correction (IC).**

| Crop Density (stems/$m^2$) | Manually Measured Height (m) | Estimated Height with IC (m) | Error with IC (m) (%) | Estimated Height without IC (m) | Error without IC (m) (%) | Improvement (m) (%) |
|---|---|---|---|---|---|---|
| 42 | 3.06 | 2.94 | 0.12 (4%) | 3.40 | 0.46(15.6%) | 0.34(11.6%) |
| 58 | 3.68 | 3.51 | 0.17 (4.6%) | 3.93 | 0.25(6.8%) | 0.08(2.2%) |
| 62 | 3.66 | 3.36 | 0.30 (8%) | 4.15 | 0.49(13.4%) | 0.19(5.4%) |
| 74 | 2.75 | 2.57 | 0.18 (6.9%) | 2.94 | 0.19(7.0%) | 0.01(0.1%) |
| 85 | 3.31 | 3.25 | 0.06 (1.8%) | 3.50 | 0.19(5.7%) | 0.13(3.9%) |

The results in *Tab.* 2.1 and *Tab*. 2.2 show that the estimated heights were always smaller than the manually measured heights. There were two reasons for this: One was the misdetection of the highest points of *MxG* stems. Since the LIDAR scanned *MxG* stems vertically, there is no guarantee that the highest point of stems is captured by the LIDAR every time. Another reason is that the manually measured stems may not be the same stems as measured by the LIDAR.

To evaluate the performance of the static height measurement method further, the method was applied to estimate the average height of a 10m x 5m *MxG* field (*Fig.* 2.1(b)). Seven locations in the field were randomly chosen as shown in *Fig.* 2.7. 140 randomly selected stems

were manually measured as a reference. The result showed that the estimated average height of the field using the LIDAR was 3.49m, while the average of manually measured stems was 3.35m. The error between the estimation value and the reference was 0.14m (4.2%).

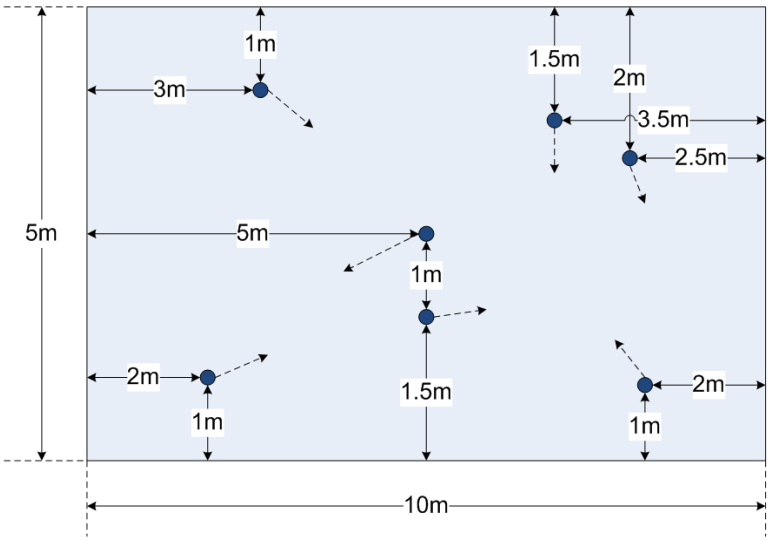


**Figure 2.7. Sampling locations in an experimental field (top view). The arrow in the figure shows the direction in which the laser scanner is facing.**

## 2.4.2 Results of dynamic height measurement

The dynamic height measurement method was tested using varying travel velocities. The coverage area was calculated using *Eqn.* 2.5 . Five stems per square meter were randomly selected and manually measured as references. As shown in *Tab.* **2.3**, while the velocity ranged from 0.2m/s to 0.41m/s, the dynamic height measurement approach achieved an error between 1.5% (0.05m) and 6.5% (0.22m).

**Table 2.3. Height estimation results of dynamic height measurement.**

| Velocity (m/s) | Covered Area ($m^2$) | Manually Measured Height (m) | Estimated Height (m) | Error (m) (%) |
|---|---|---|---|---|
| 0.31 | 19.99 | 3.39 | 3.48 | 0.09(2.7%) |
| 0.32 | 20.25 | 3.66 | 3.53 | 0.13(3.6%) |
| 0.25 | 21.4 | 3.32 | 3.19 | 0.13(3.9%) |
| 0.28 | 24.16 | 3.66 | 3.52 | 0.14(3.8%) |
| 0.24 | 26.22 | 3.45 | 3.27 | 0.18(5.2%) |
| 0.31 | 17.12 | 3.41 | 3.25 | 0.16(4.7%) |
| 0.40 | 29.1 | 3.67 | 3.51 | 0.16(4.4%) |
| 0.22 | 32.21 | 3.36 | 3.41 | 0.05(1.5%) |
| 0.26 | 26.16 | 3.64 | 3.54 | 0.1(2.7%) |
| 0.41 | 29.32 | 3.40 | 3.18 | 0.22(6.5%) |
| 0.33 | 25.23 | 3.51 | 3.37 | 0.14(4%) |
| 0.20 | 21.18 | 3.48 | 3.61 | 0.13(3.7%) |
| 0.28 | 16.83 | 3.55 | 3.43 | 0.12(3.4%) |
| 0.24 | 17.66 | 3.56 | 3.68 | 0.12(3.4%) |

The dynamic height measurement followed the same procedure per frame as the static height measurement where the inclination correction approach improved the results in similar fashion. The estimations with and without inclination correction were compared as shown in *Tab.* 2.4. The results showed that the inclination correction approach improved the dynamic height measurement. The error was reduced by 4.1% (0.14m) on average with a maximum of 9.8% (0.31m).

The error of measurement may be caused mainly by erroneous measurements, since the laser scanner might not always capture the highest points of the plants. By taking the mean of multiple measurements this error was reduced. The dynamic height measurement method was repeated in a single *MxG* field 10 times at the same velocity. The means of measurements are listed in *Tab.* 2.5. . 100 *MxG* stems were randomly selected from the coverage area to be manually measured as references (3.45 m). It is clear that with an increasing number of measurements, the estimation error was reduced to 0.02m from 0.08m.

**Table 2.4. Dynamic height measurement comparison with and without inclination correction.**

| Velocity (m/s) | Manually Measured Height (m) | Estimated Height with IC (m) | Error with IC (m) (%) | Estimated Height without IC (m) | Error without IC (m) (%) | Improvement (m) (%) |
|---|---|---|---|---|---|---|
| 0.31 | 3.39 | 3.48 | 0.09(2.7%) | 3.24 | 0.15(4.4%) | 0.06(1.8%) |
| 0.32 | 3.66 | 3.53 | 0.13(3.6%) | 3.48 | 0.18(4.9%) | 0.05(1.4%) |
| 0.25 | 3.32 | 3.19 | 0.13(3.9%) | 3.18 | 0.14(4.2%) | 0.01(0.3%) |
| 0.28 | 3.66 | 3.52 | 0.14(3.8%) | 3.24 | 0.42(11.5%) | 0.28(7.7%) |
| 0.24 | 3.45 | 3.27 | 0.18(5.2%) | 3.12 | 0.33(9.6%) | 0.15(4.3%) |
| 0.31 | 3.41 | 3.25 | 0.16(4.7%) | 3.17 | 0.24(7%) | 0.08(2.3%) |
| 0.40 | 3.67 | 3.51 | 0.16(4.4%) | 3.15 | 0.52(14%) | 0.36(9.8%) |
| 0.22 | 3.36 | 3.41 | 0.05(1.5%) | 3.21 | 0.15(4.4%) | 0.10(3%) |
| 0.26 | 3.64 | 3.54 | 0.1(2.7%) | 3.53 | 0.11(3%) | 0.01(0.3%) |
| 0.41 | 3.40 | 3.18 | 0.22(6.5%) | 3.08 | 0.32(9.4%) | 0.1(3%) |
| 0.33 | 3.51 | 3.37 | 0.14(4%) | 3.30 | 0.21(6%) | 0.07(2%) |
| 0.20 | 3.48 | 3.61 | 0.13(3.7%) | 3.60 | 0.12(3.4%) | 0.25(7.2%) |
| 0.28 | 3.55 | 3.43 | 0.12(3.4%) | 3.66 | 0.11(3.1%) | 0.23(6.5%) |
| 0.24 | 3.56 | 3.68 | 0.12(3.4%) | 3.75 | 0.19(5.3%) | 0.31(8.7%) |

**Table 2.5. Height estimation from multiple measurements.**

| Measurement Times | 1 | 2 | 3 | 4 | 5 | 6 | 7 | 8 | 9 | 10 |
|---|---|---|---|---|---|---|---|---|---|---|
| **Means of Measurements (m)** | 3.53 | 3.50 | 3.49 | 3.48 | 3.49 | 3.48 | 3.46 | 3.48 | 3.48 | 3.47 |
| **Error (m) (%)** | 0.08 | 0.05 | 0.04 | 0.003 | 0.04 | 0.03 | 0.01 | 0.03 | 0.03 | 0.02 |
| | 2.3% | 1.5% | 1.2% | 0.9% | 1.2% | 0.9% | 0.3% | 0.9% | 0.9% | 0.6% |

## 2.4.3 Height Based Yield Model

The relationship between height and mass of an individual stems can be obtained based on *Eqn.* 1.1:

$$Y = d * \pi \left( \frac{D}{2} \right)^2 * H * \rho \tag{1.1}$$

The yield in a certain area is the product of the average mass of individual *MxG* stems and the total number of stems in the coverage area:

$$\mathrm{Y} = \bar{W}_{indi} \times Num = H \times \pi(\frac{D}{2})^2 \times \rho \times Num \quad (2.12)$$

Where Y is the yield in $\frac{kg}{m^2}$, $\bar{W}_{indi}$ is the average mass of *MxG* stems, $Num$ is the number of stems in a certain area, $D$ is the diameter of *MxG* stems (in m), $H$ is the height of *MxG* stems (in m), and $\rho$ is the material density of *MxG* stems in $\frac{kg}{m^3}$. Based on *Eqn.* 2.12, with the assumption of constant density, the relationship between individual mass and *MxG* stem height is linear.

To validate the relationship shown in *Eqn.* 2.12, the heights and mass of 130 *MxG* stems were measured manually, and a linear function (*Eqn.* 2.13) was applied to fit the collected sample points.

$$W_{indi} = f(H) = c_1 H + c_2 \quad (2.13)$$

An ordinary least squares based method was applied to generate a regression curve. The result is shown in *Fig.* 2.8. The fitted curve found was:

$$W_{indi} = f(H) = 45.23H - 38 \quad (2.14)$$

The R-Square value of this estimation is 0.86. Thus, the yield and the stem height of *MxG* exhibit a linear relationship.

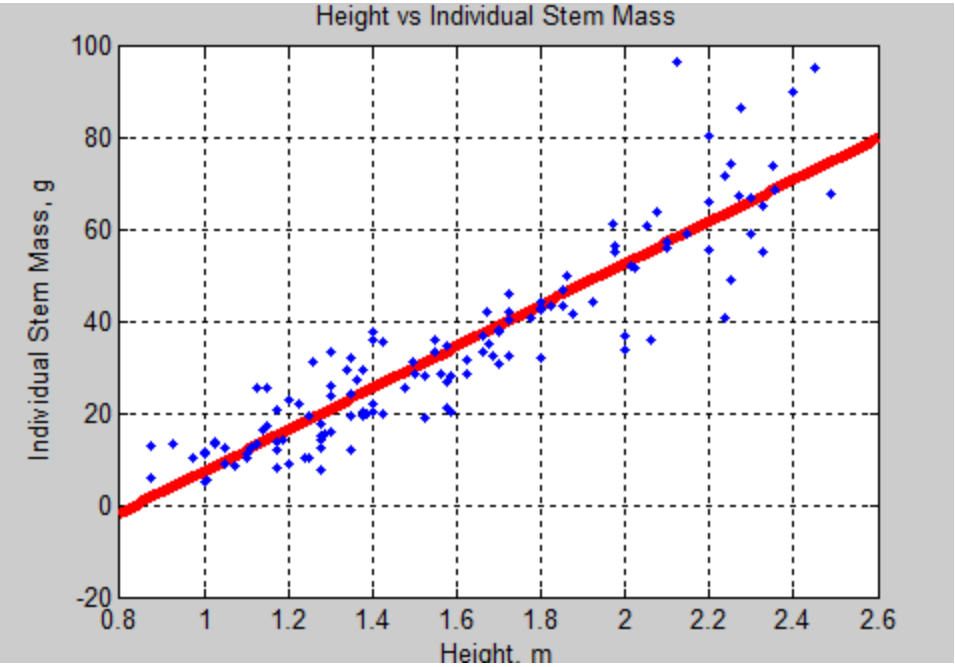


**Figure 2.8. Relationship between individual mass and *MxG* stem height.**

## 2.5 Summary and Conclusions

Height is considered an important yield related parameter of *MxG* since it can be used to estimate yield. An automatic laser scanner-based *MxG* height measurement method was described. The laser scanner was employed to scan plants vertically to capture the data, which contained the distance from objects to the laser scanner and the corresponding angle with the laser scanner as the origin. Both static and dynamic height estimation approaches were described.

With the static height measurement approach, the laser scanner was placed in an arbitrary location to capture the data. A distance filter was applied based on the system's operating range. The tangential resolution was analyzed based on a geometric model of the height measurement. The remaining data after filtering was processed by an inclination correction algorithm to increase the accuracy. In the dynamic height measurement approach, the laser scanner traveled

along the crop at a constant velocity, and the captured data were separated into individual frames. The same process as employed in the static height measurement approach was used on these single frames. All the sampling points were placed into a 3D space, using the velocity information. An ordinary least squares based surface fitting algorithm was applied to generate the top surface of the *MxG* using the detected highest points in each individual frame. Similarly, the ground related surface was generated using ground-related points. The coverage area was calculated by the coordinates of the highest detected points in each frame. The average height of the coverage area was obtained by calculating the average distance between crop height and ground surface.

Both static and dynamic height measurement approaches proved practicable in estimating the height of *MxG* in a field. The static height measurement was robust within crop densities ranging from 42 to 85 stems/$m^2$. The method achieved an accuracy in the range of 92% (0.3m error) to 98.2% (0.06m error).

The method was also used to estimate the average height of a 5m x 10m field, compared with randomly chosen, manually measured stems. This resulted in an accuracy of 95.8% (0.14m error). The dynamic height measurement method was tested under various velocities ranging from 0.2m/s to 0.41m/s, with an achieved accuracy ranging from 93.5% (0.22m error) to 98.5% (0.05m error). The inclination correction algorithm was shown to increase the estimation accuracy for both static and dynamic height measurements: The accuracy of static height measurements were improved by 0.01m (0.1%) to 0.34m (11.6%), while the dynamic height measurements were improved by 0.3% (0.01m) to 9.8% (0.31m). The main limitation of the

method was erroneous measurements of the laser scanner, which can be dealt with by combining multiple measurements and calculating the mean value.

# CHAPTER 3
# A REAL-TIME LIDAR BASED PLANT STEM DIAMETER SENSOR

## 3.1 Introduction

The objective of the research reported in this chapter was to measure the diameter of *Miscanthus Giganteus* (*MxG*) stems in real-time.

Diameter measurement of stems and stalks has been attempted by many researchers. McDonald *et al.* (2003) developed a photo-interruption based time-of-fight sensor to measure the diameter of trees. Grift and Oberti (2006) developed a method to measure the root collar diameter of pine seedlings in a laboratory. It was reported that the method achieved an accuracy of 0.1-0.3mm based on various conditions and configurations. Delwiche and Vorhees (2003) designed an optoelectronic system to measure the diameter of deciduous trees. Unlike the interruption method, in their research, an infrared laser was employed, and the sensors were mounted unilaterally. The error of their method was reported up to $\pm$1.9mm.

One of the complications of this research compared to the references mentioned above is that with *MxG*, it is not possible to measure diameters of single stems directly, since they grow in clumps. Therefore a laser scanning (LIDAR) method was applied, similar to Lefsky *et al.* (1999)

who used a laser scanner to estimate temperate mixed deciduous forest biomass. Also in forestry, Nilsson (1996) used a laser scanner to measure the tree height and stand volume, and Popescu *et al.* (2003) measured the crown diameter using a laser scanner as well. In contrast to the research in forestry, here the diameters of smaller clumped objects (5-20mm) need to be measured.

The objective of this research was to measure the diameters of clumped *MxG* stems in the field as part of a yield monitoring system. The approach was to measure the reflection of laser light from clumped *MxG* stems and to use an algorithm to separate the clumps into measurable individual stem diameters.

## 3.2 Materials

To estimate the diameter of *MxG* stems, a SICK® Laser scanner was applied to scan horizontally. The data were collected using a SICK ® LMS 291 laser scanner in an experiment field at Urbana-Champaign Illinois (lat/lon: 40.042455,-88.237943) in the Spring of 2010. The laser scanner featured a 905nm wavelength infrared light source, up to 180 degrees field of view, 0 to 80 meters operating range (the maximum range with 10% reflectivity was 30 meters), and a 75Hz scanning frequency. The angle resolution was 0.25 or 0.5 degrees and the radial resolution was 1mm. The laser scanner had a systematic error of $\pm$35mm, and a statistical error of 10mm (SICK® Technical Description, 2006). The laser scanner was configured to a range of 100 degrees with an angle resolution of 0.25 degrees.

The laser scanner communicated with a computer (Panasonic TOUGHBOOK CF-30, Intel® CoreTM 1.6GHz, 1.0GB of RAM, 80GB hardware) through a serial port with a baud rate of 9600bits/s. A MATLAB®/C++ data acquisition application was developed to collect data in the

field. The laser scanner was mounted at a height of 87cm above the ground. The sampling locations were randomly selected in a *MxG* field.

## 3.3 Methodology

*MxG* stems presented themselves as a set of points in the raw data of the laser scanner. A fuzzy cluster based algorithm was developed to estimate the diameters of *MxG* stems from the laser scanner data. The algorithm consisted of region of interest (ROI) definition, pre-processing, clustering and post-processing.

### 3.3.1 Definition of the region of interest (ROI)

Even though the operating range of the laser scanner can reach 80 meters, the limitation posed by the angle resolution led to a poor tangential resolution with an increase of the operating range. *Eqn.* 3.1 shows the relationship between the operating distance and the tangential resolution.

$$R_T = 2 * d * \sin\left(\frac{0.25}{2}\right) \qquad (3.1)$$

Where $R_T$ is the tangential resolution in mm, $d$ is the operating distance in mm and 0.25 is the angle resolution of the laser scanner.

*Eqn.* 3.1 shows that the operating distance is inversely proportional to the tangential resolution. Thus, before estimating the diameters of *MxG* stems, a region of interest needed to be determined. To achieve this, the *MxG* stems were modeled as vertical cylinders (*Fig.* 3.1).

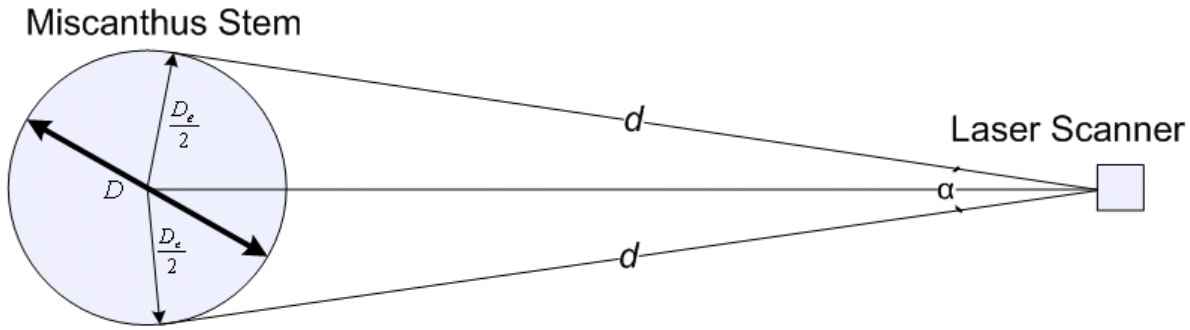


**Figure 3.1. Geometric model of *MxG* stem. Crossing sectional area of *MxG* was modeled as a circle.**

Assuming that the diameter of *MxG* stem was *D*, the starting point and the end point of the interception of the *MxG* stem with the laser sheet define two lines with an angle of $\alpha$ degrees between them. The length from the intersection points to the laser scanner was *d* in m. Based on this geometric relationship, the diameter of *MxG* can be estimated as:

$$D_e = 2 * d * \tan\left(\frac{a}{2}\right) \quad (3.2)$$

Since the *MxG* stem was modeled as shown in *Eqn.* 3.2, the tangential resolution is presented in *Eqn.* 3.3.

$$R_T = 2 * d * \tan\left(\frac{0.25}{2}\right) \quad (3.3)$$

The diameter of *MxG* stems varied from 5mm to 20mm. The tangential resolution of the laser scanner was set to 2mm . Thus the ROI was:

$$ROI = \frac{R_T}{2 * \tan\left(\frac{0.25}{2}\right)} = 458.37mm \quad (3.4)$$

Where $R_T$ was 2mm in *Eqn.* 3.4. When $R_T$ is 2mm, the difference between *Eqn.* 3.1 and *Eqn.* 3.4 was smaller than 0.001mm. The ROI was chosen as 400mm, the corresponding tangential resolution which was 1.745mm. The coverage area $S$ within the ROI was computed as:

$$S = \pi * (400)^2 * \frac{100}{360} = 139626.34mm^2 = 0.13m^2 \quad (3.5)$$

### 3.3.2 Pre-grouping

Noise samples may occur in the ROI data, several of which were caused by the limitation of the operating angle range (100 degrees), and others were caused by the ROI definition (e.g. incomplete stems). These noisy points would affect the subsequent clustering approach. To filter these noisy points and to simplify the clustering approach, the laser scanner data within the ROI was pre-grouped based on angle continuity, meaning that the difference between two neighboring sample points, in the angle domain, was smaller than one degree.

To pre-group the data, an angle histogram was obtained. The angle range was separated into intervals with an angle of one degree, which were denoted as $B_i (i = 1, 2, ..., 100)$. The numbers of the sample points in each interval were calculated as follows:

$$n_i = \sum_{j=1}^{N} \{P_j \in B_i\} \quad (3.6)$$

Where each $P_j$ is a sample point in the ROI and $N$ is the total number of sample points in the ROI. The empty intervals were considered borders among each group. The raw data from the laser scanner is shown in *Fig.* 3.2 (a), and the pre-grouped data within the ROI is shown in *Fig.* 3.2 (b).

In the pre-grouped data sets, if the object presented by the sample groups was smaller than 5mm (The diameter of *MxG* ranges from 5mm to 20mm in common), the corresponding sample groups were considered noise groups. These noise groups were filtered based on their size. If the number of sample points in a pre-grouped group was smaller than a threshold, which was a function of the distance from the intersection points to the laser scanner (*Eqn.* 3.7), this group was removed from the ROI data set. The threshold was computed as follows:

$$Th_n = 8 * \arctan(\frac{2.5}{d}) \quad (3.7)$$

Where $Th_n$ is the threshold, $d$ is the average length of the group from the intersection points to the laser scanner. The number 2.5 in *Eqn.* 3.7 represented 2.5 mm, which was considered a radius threshold of *MxG* stems.

In the remaining pre-grouped groups, if the number of the sample points fell into a specified range (*Eqn*. 3.8), the sample groups were considered representatives of *MxG* stems (*Fig.* 3.2). The geometric model described previously (*Eqn.* 3.2) was applied to extract the diameter information of *MxG* stems in groups that where assumed to originate from single *MxG* stems. In *Eqn.* 3.2, *d*, the distance between the laser scanner and *MxG* stem was regarded the average distance of the grouped sample points, and α, the angle between two interception points was obtained from the angle range of the sample group.

$$8 * \arctan(\frac{2.5}{d}) < Num < 8 * \arctan(\frac{10}{d}) \quad (3.8)$$

Where *Num* is the number of sample points in a group, and $d$ as defined in *Eqn.* 3.1. The number 2.5 and 10 presented the radius thresholds of *MxG* stems, which were 2.5mm and 10mm respectively.

### 3.3.3 Clustering

After pre-grouping, there were several groups that contained more than one *MxG* stem according to the size of the groups (*Fig.* 3.2(d)). The sample points in these groups were angle continuous, which means that the angle difference between two adjacent sample points was smaller than 0.25 degrees. To separate *MxG* stems within the groups, a clustering method was applied.

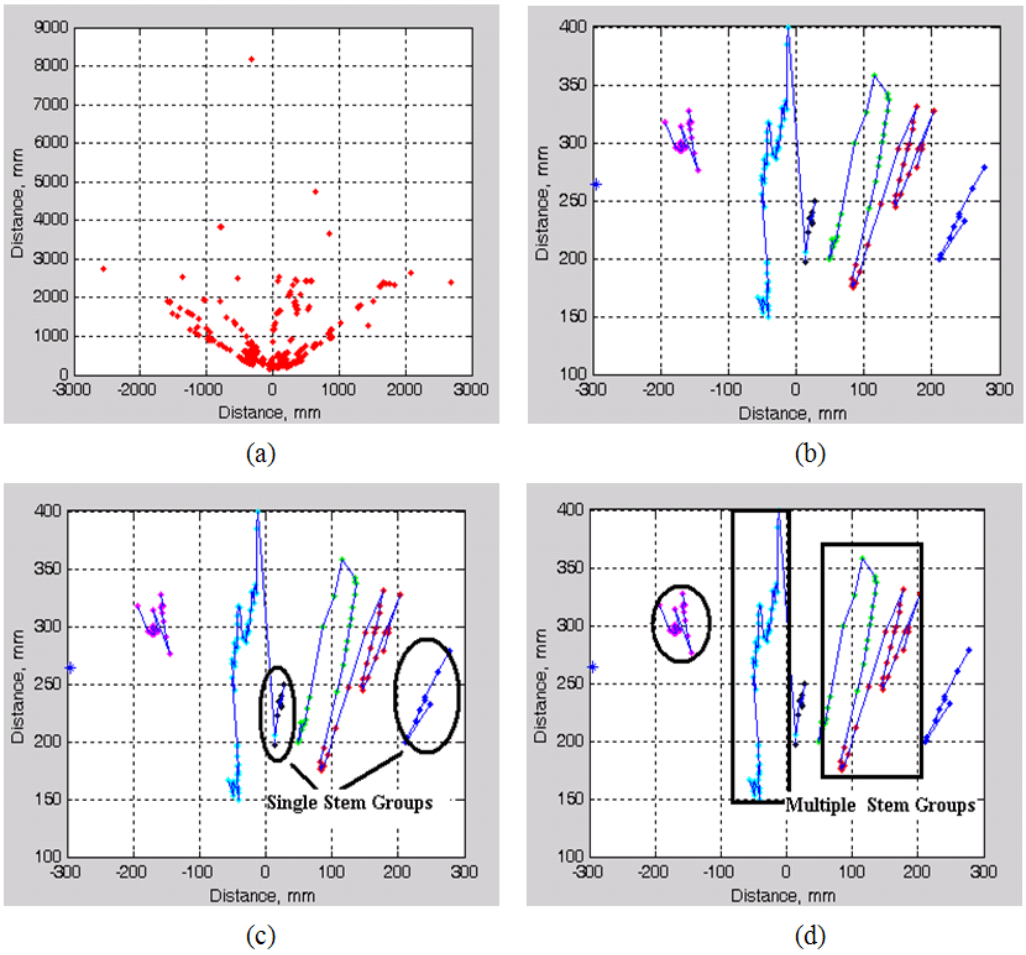


**Figure 3.2. Data obtained by the laser scanner. (a) Raw data from the laser scanner. (b) Pre-grouped data within the ROI. (c) Single stem groups in the pre-grouped ROI data. (d) Multiple stem groups in the pre-grouped ROI data.**

The features of the sample points fed to the cluster were the location information of the *MxG* stems in the laser scanner image. In Cartesian coordinates, there were two parameters *x* and *y*, the position of the laser scanner which was defined as the origin in the coordinate frame. The data were normalized before feeding them to the clustering algorithm. Assuming there were *N* valid sample points, $p_i = (x_i, y_i)\ i = 1, 2, ...N$, within the ROI, the normalized features, $X_i$ and $Y_i$ were calculated using the following equations:

$$\begin{cases} X_i = \dfrac{x_i - \min\{x_i\}}{\max\{x_i\} - \min\{x_i\}} \\ Y_i = \dfrac{y_i - \min\{y_i\}}{\max\{y_i\} - \min\{y_i\}} \end{cases} \quad (3.9)$$

The sample points were mapped onto the interval [0,1] after normalization. Figure 3.3 shows an example of a normalized data group.

Assuming that the data set $P = [p_1, p_2, p_3, ..., p_N]$, $p_i$ denotes sample points of the laser scanner, the data dimension is $N \times n$. *N* is the number of sample points within the ROI, and *n* is the number of the features fed to the cluster (*n* = 2). The cluster prototypes are described as $V = \{v_i \,|\, 1 \le i \le c\}$. $v_i$ which refers to the center of the clusters in the features domain, and *c* denotes the total number of clusters. A partition matrix:

$$U = \begin{bmatrix} \mu_{1,1} & \mu_{1,2} & \cdots & \mu_{N,1} \\ \mu_{2,1} & \mu_{2,2} & \cdots & \mu_{N,2} \\ \vdots & \vdots & \ddots & \vdots \\ \mu_{N,1} & \mu_{N,2} & \cdots & \mu_{N,c} \end{bmatrix} \quad (3.10)$$

$\mu_{i,k}$ denotes the probability that the $k^{th}$ sample point belonged to the $i^{th}$ cluster, and it satisfied the following criteria: The probability $\mu_{i,k}$ is between 0 and 1. The sum of the probability of the $k^{th}$ sample point belonging to each cluster is 1. Within a cluster, the sum of the probability of all the points is larger than 0 and smaller than the number of the sample points.

$$\begin{cases} \mu_{k,i} \in [0,1], 1 \le k \le N, 1 \le i \le c; \\ \sum_{i=1}^{c} \mu_{k,i} = 1, 1 \le k \le N; \\ 0 < \sum_{k=1}^{N} \mu_{k,i} < N, 1 \le i \le c; \end{cases} \quad (3.11)$$

The principle behind the GK Clustering algorithm is to minimize an object function (Gustafson and Kessel, 1979):

$$J(X;U,V,A) = \sum_{i=1}^{c}\sum_{k=1}^{N} (\mu_{ik})^2 D^2_{ikA_i} \quad (3.12)$$

Where

$$D_{ikA}{}^2 = \|p_k - v_i\|_A^2 = (p_k - v_i)^T A_i (p_k - v_i) \quad (3.13)$$

$$A_i = [\rho_i \det(F_i)]^{\frac{1}{n}} F_i^{-1}, \ \|A_i\| = \rho_i \quad (3.14)$$

$$F_i = \frac{\sum_{k=1}^{N} (\mu_{ik})^2 (p_k - v_i)(p_k - v_i)^T}{\sum_{k=1}^{N} (\mu_{ik})^2} \quad (3.15)$$

The minimization approach of *Eqn.* 3.12 used was based on previous research (Babuška *et al.*, 2002). The method updated the cluster centers interactively based on the cluster covariance and distance between sample points and cluster centers. The detailed procedures are shown follows:

**Step 1**: Compute the cluster center:

$$v_i^{(l)} = \frac{\sum_{k=1}^{N} \left(\mu_{ik}^{(l-1)}\right)^2 p_k}{\sum_{k=1}^{N} \left(\mu_{ik}^{(l-1)}\right)^2}, \quad 1 \le i \le c \qquad (3.16)$$

Where, $l$ is the iteration number.

**Step 2**: Calculate the cluster covariance:

$$F_i^{(l)} = \frac{\sum_{k=1}^{N} \left(\mu_{ik}^{(l-1)}\right)^2 \left(p_k - v_i^{(l)}\right)\left(p_k - v_i^{(l)}\right)^T}{\sum_{k=1}^{N} \left(\mu_{ik}^{(l-1)}\right)^2}, \quad 1 \le i \le c \qquad (3.17)$$

**Step 3**: Calculate the distances between sample points and cluster centers:

$$D_{ikA_i}{}^2 == \left(p_k - v_i^{(l)}\right)^T A_i \left(p_k - v_i^{(l)}\right) \qquad (3.18)$$

Where $A_i$ is as described in *Eqn.* 3.14.

**Step 4**: Update the partition matrix

$$\mu_{ik}^{(l)} = \frac{1}{\sum_{j=1}^{c} \left( \frac{D_{ikA_i}\left(p_k, v_i\right)}{D_{jkA_i}\left(p_k, v_j\right)} \right)^2}, 1 \le i \le c, \; 1 \le k \le N \qquad (3.19)$$

Repeat all the steps above, until $\left\| U^{(l)} - U^{(l-1)} \right\| < \varepsilon$.

*Fig.* 3.3(b) shows the clustering result of the GK clustering algorithm for the data group shown in *Fig.* 3.3(a). The circles in the figure show $\mu_{ik}$ values varying from 0.5 to 0.9 of each cluster.

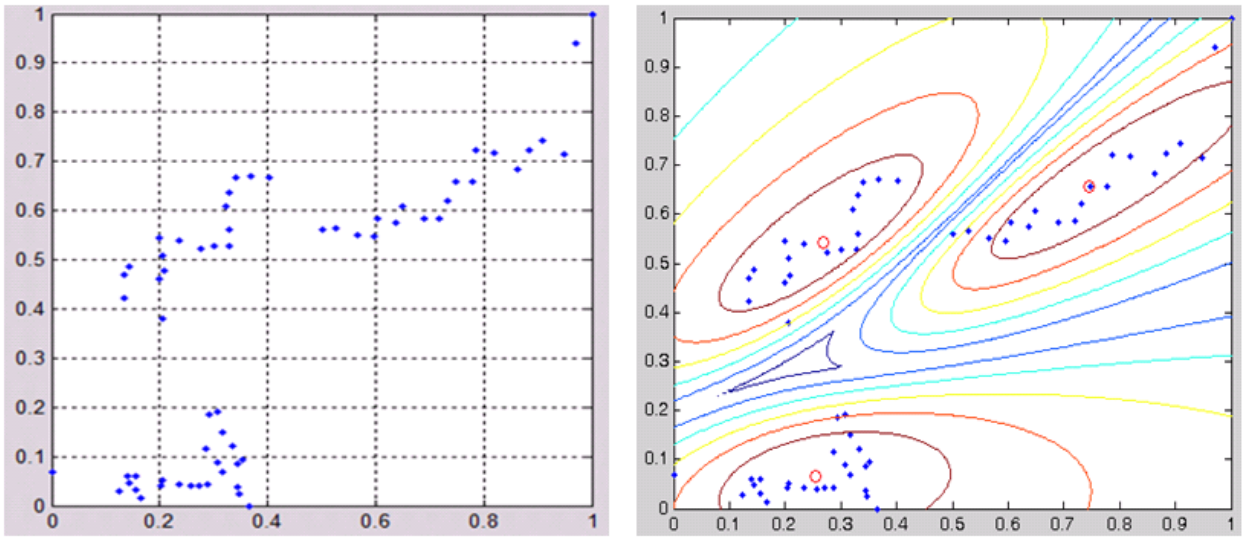


**Figure 3.3. Normalized data set and corresponding clustering result based on GK clustering algorithm. (a) Example of normalized multiple stems group. (b) Clustering result of the data group in *Fig.* 3.3(a) based on the GK clustering algorithm, with a cluster number of three.**

Based on the result shown in *Fig.* 3.3(b), the GK cluster separated the *MxG* stems in multiple stem groups well. However, this result was obtained based on the assumption that the total cluster number was known before applying the GK clustering algorithm. To predict the total number of clusters, seven validity measures were chosen to optimize the choice of the number of cluster in the data set. They were partition coefficient (PC), classification entropy (CE) (Bezdek, 1981), partition index (SC), Separation index (S) (Bensaid *et al.*, 1996), Xie and Beni's index (XB) (Xie and Beni, 1991), Dunn's index (DI) (Dunn, 1973) and alternative Dunn index (ADI) (Bezdek and Dunn, 1975). The data sets were clustered into two to seven clusters, and the

corresponding validity measures were computed by *Eqn.* 3.20 to *Eqn.* 3.26 for each cluster number. The optimal cluster number was obtained by using four of them, being SC, S, XB and ADI. Figure 3.4 shows the clustering results of various cluster numbers, and *Fig.* 3.5 shows the corresponding validity measures of each cluster number. The optimal cluster number was obtained when the SC and C decreased sharply and XBI and DI reached a local maximum.

$$PC(c) = \frac{1}{N}\sum_{i=1}^{c}\sum_{j=1}^{N}\left(\mu_{ij}\right)^{2} \quad (3.20)$$

$$CE(c) = -\frac{1}{N}\sum_{i=1}^{c}\sum_{j=1}^{N}\mu_{ij}\log\left(\mu_{ij}\right) \quad (3.21)$$

$$SC(c) = \sum_{i=1}^{c}\frac{\sum_{j=1}^{N}\left(\mu_{ij}\right)^{2}\left\|p_j - v_i\right\|^{2}}{N_i\sum_{k=1}^{c}\left\|v_k - v_i\right\|^{2}} \quad (3.22)$$

$$S(c) = \frac{\sum_{i=1}^{c}\sum_{j=1}^{N}\left(\mu_{ij}\right)^{2}\left\|p_j - v_i\right\|^{2}}{N\min_{i,k}\left\|v_k - v_i\right\|^{2}} \quad (3.23)$$

$$XB(c) = \frac{\sum_{i=1}^{c}\sum_{j=1}^{N}\left(\mu_{ij}\right)^{2}\left\|p_j - v_i\right\|^{2}}{N\min_{i,j}\left\|p_j - v_i\right\|^{2}} \quad (3.24)$$

$$DI(c) = \min_{i\in c}\left\{\min_{j\in c, i\neq j}\left\{\frac{\min_{p\in c_i, q\in c_j} d(p,q)}{\max_{k\in c}\left(\max_{p,q\in c} d(p,q)\right)}\right\}\right\} \quad (3.25)$$

$$ADI(c) = \min_{i\in c}\left\{\min_{j\in c, i\neq j}\left\{\frac{\min_{p\in c_i, q\in c_j}\left|d(q,v_j) - d(p,v_j)\right|}{\max_{k\in c}\left(\max_{p,q\in c} d(p,q)\right)}\right\}\right\} \quad (3.26)$$

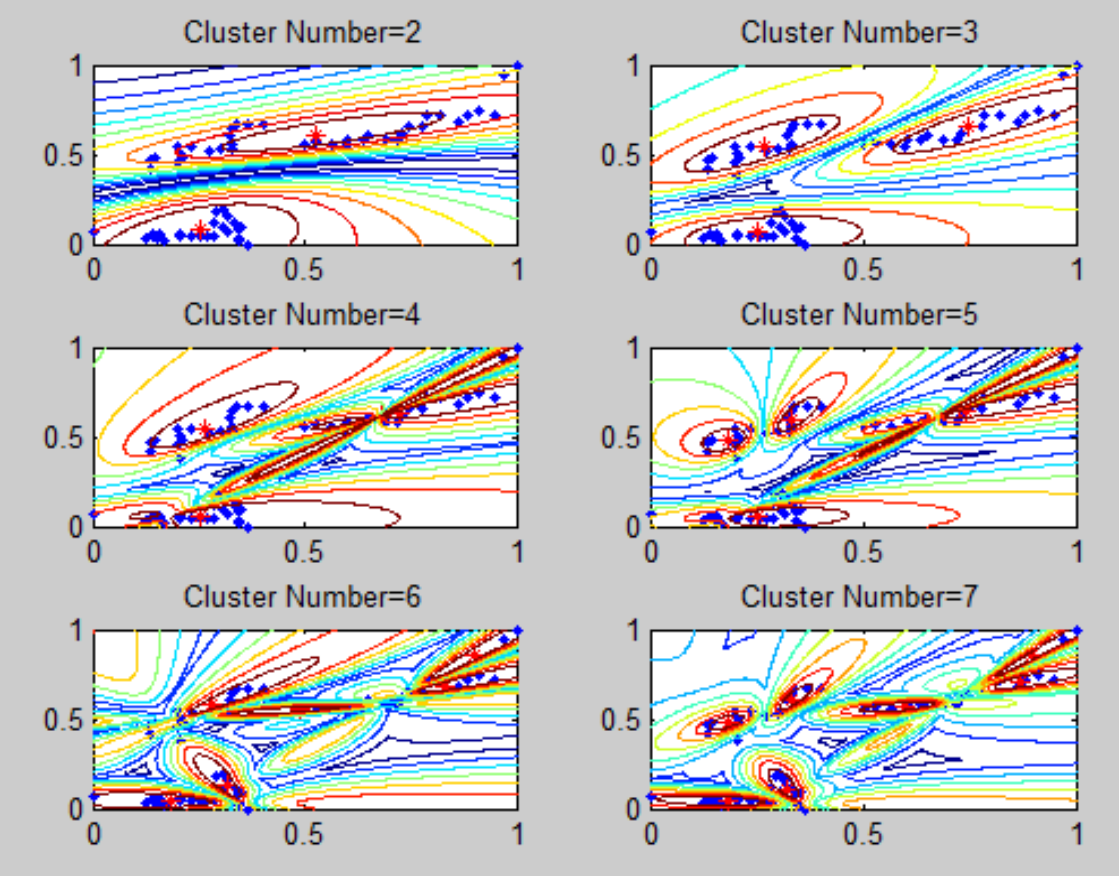


**Figure 3.4. Clustering results (GK clustering) of various cluster numbers from two to seven.**

If the probability of a sample point falling into a certain cluster was above 70%, this sampling point was considered to belong to this cluster. The reason to choose 70% as a threshold was because within this range the distance between the sample point in a cluster and the cluster center was close to 35mm, which was the systematic error of the laser scanner. There were still several sampling points, which did not belong to any cluster. These points were considered as uncertain points and discarded.

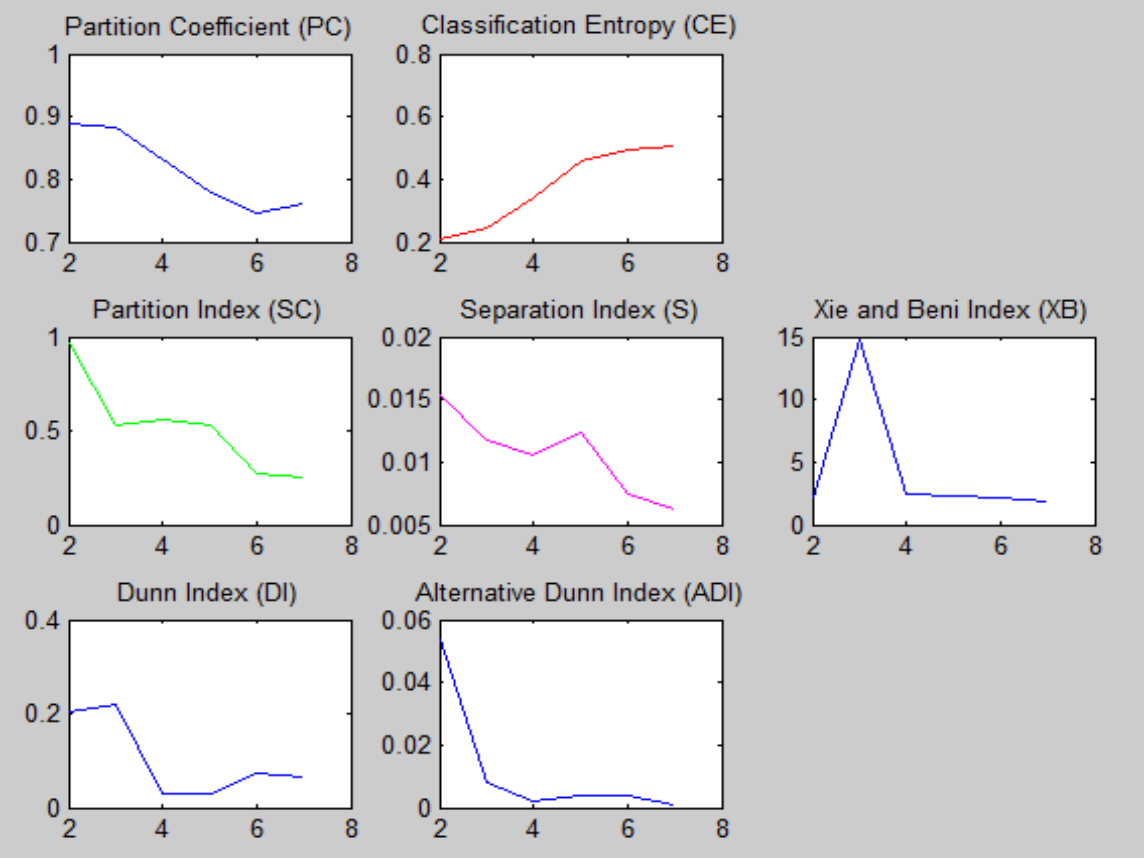


**Figure 3.5. Validity measures for varying cluster numbers (in *Fig.* 3.4). The x-axes represent the number of clusters, the y-axes represent the value of each validity measure.**

An angle-continuity check was applied to the clustered multiple stem groups to confirm that all sample points in a cluster were angle continuous. If they were not, the cluster was considered an invalid set. If the number of sample points in a cluster was smaller than a threshold (*Eqn.* 3.7), this cluster was considered an invalid set as well. The diameter information of *MxG* stems was only extracted from valid clusters, and all invalid sets were removed from the samples. In 10 randomly chosen test data sets, all clusters were valid. *Eqn.* 3.2 was applied to extract the diameter information from the *MxG* stems from each valid cluster. Figure 3.6 shows an example of a of laser scanner data set within the ROI (*Fig.* 3.2(b)). Different colored points groups presented different *MxG* stems in the figure.

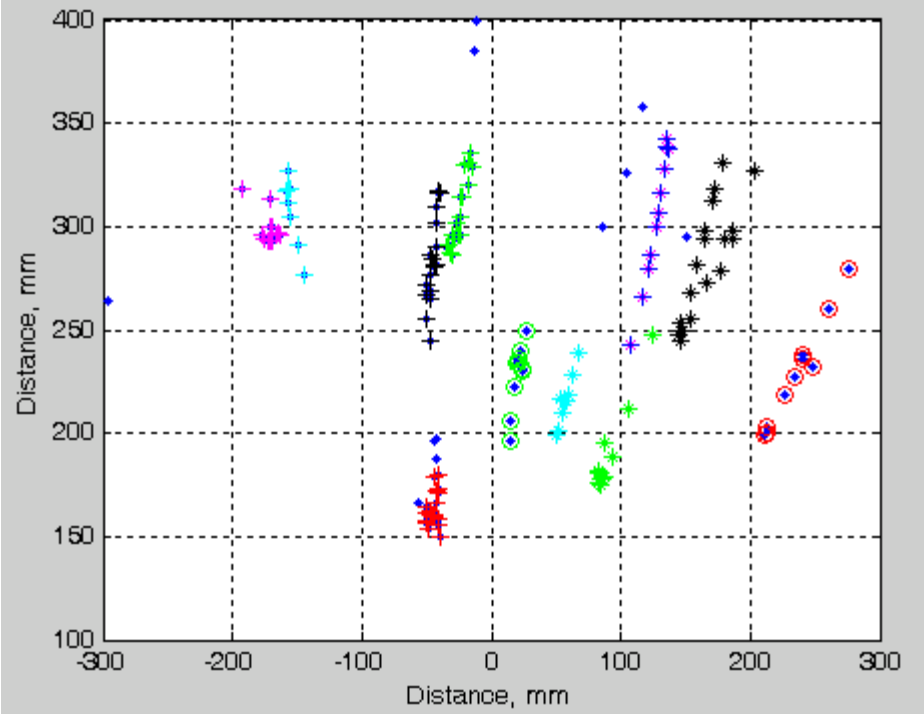


**Figure 3.6. Clustering result of data shown in *Fig.* 3.2. Different combination of colors and symbols present different *MxG* stems.**

## 3.4 Results and Discussion

The method applied consisted of four stages being, 1) presentation of *MxG* stems in the laser scanner data, 2) clustering algorithm comparison, 3) feature extraction and 4) field test evaluation, which are described in sequence.

### 3.4.1 Presentation of *MxG* stems in the laser scanner data

To evaluate the clustering based *MxG* stem diameter extraction method, the representations of the *MxG* stems in the laser scanner data needed to be identified. Laser scanner data were captured with 1 stem, 4 stems and 8 stems in the lab to identify the shapes of the *MxG* stems in the data (*Fig.* 3.7). The *MxG* stems presented themselves as vertically distributed sample sets in

these figures. There were several reasons why the *MxG* stems presented themselves as the shapes shown in *Fig.* 3.6 and *Fig.* 3.7.

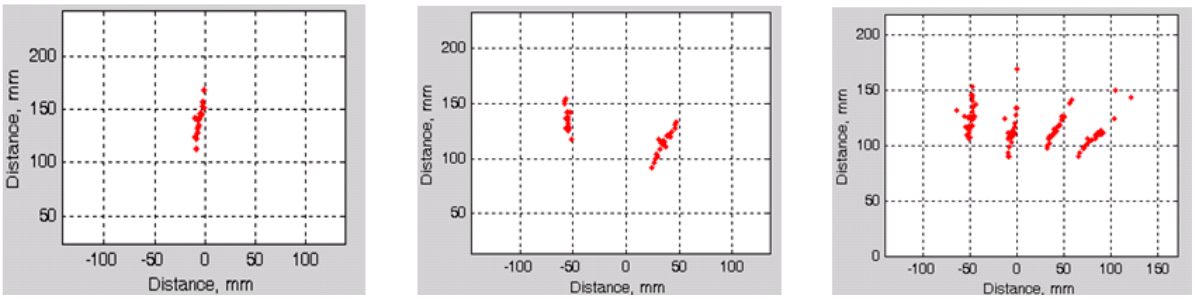


**Figure 3.7. Presentation of *MxG* stems in the laser scanner data, from left to right: One stem, two stems and four stems.**

Firstly, the accuracy of the laser scanner is limited. As mentioned, the systematic error of the laser scanner was ±35mm, and the statistical error was 10mm in the radial direction. Ideally, the sample points belonging to one *MxG* stem should be in a small circle being the shape of the *MxG* stem. However, because of the resolution limitation of the laser scanner, there were sample points, which belonged to the same *MxG* stem falling outside the circle along the radial direction. In addition, the reflection rate of the light source of the laser scanner (wavelength: 905nm) was relatively low, which caused a measurement error. Furthermore, the presentation of *MxG* stems was also affected by its color and by the relatively small size of the *MxG* stems.

To test the influence of the color of the scanned object on the laser scanner data, five flat objects with various colors and identical size (270mm x 300mm) and material (plastic) were scanned by the laser scanner at the same location. The distance between the objects and the laser scanner was 340mm. The results are shown in *Fig.* 3.8(a) and *Tab.* 3.1.

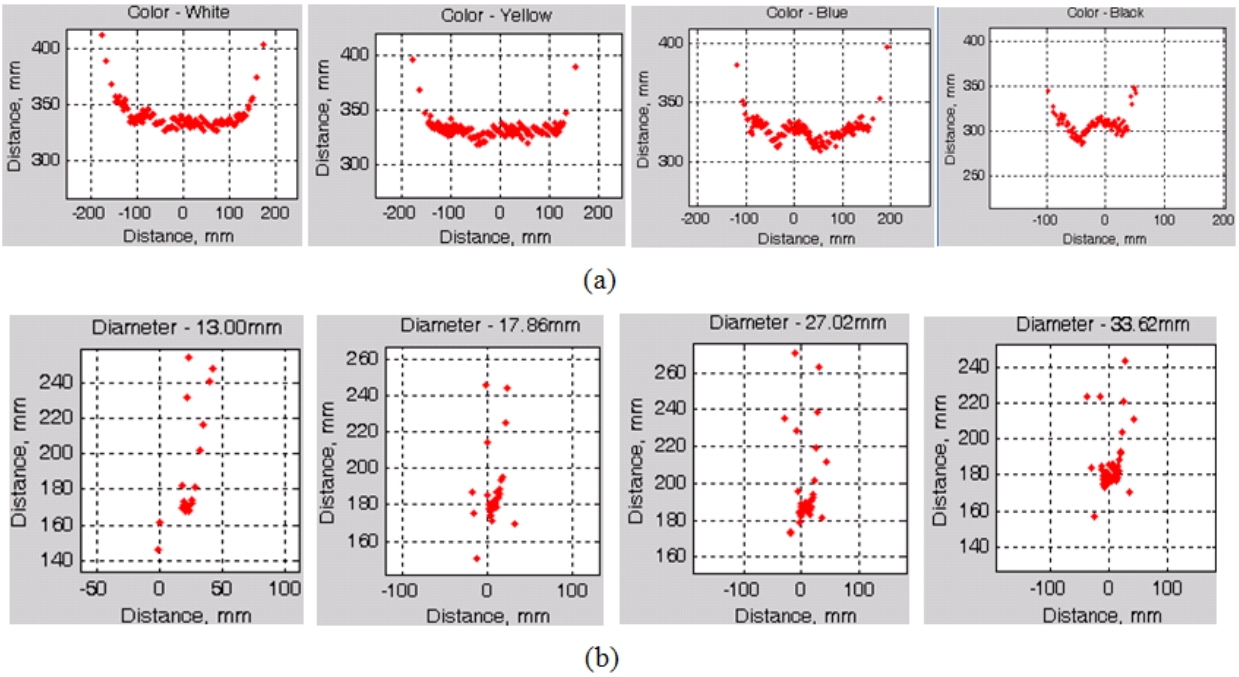


**Figure 3.8. Color and size effects on the laser scanner. (a) Color effect on the laser scanner, from left to right: white, yellow, blue and black. (b) Size effect on the laser scanner, diameters of objects from left to right: 10.75mm, 21.36mm, 34.01mm and 41.50mm. The unit in these figures is mm in both x and y axis.**

There were 182 sample points detected in the range of 370mm of a white object. The measured length was 376.8mm and the measured distance between the object and the laser scanner was 335.6mm with a standard deviation of 5.43mm$^2$. However, for a black object, the number of detected sample points in the same range was 97. The measured length was 148.6mm, and the measured distance was 307mm with a standard deviation of 11.91 mm$^2$. It was evident that the dark object had the least accurate scanning result. This was because the dark object absorbed the radiation from the laser scanner, which was reflected by the brighter objects. Figure 3.8(b) shows the scanning results of objects with the same color (white) and material (paper), but varying diameter (size). The objects were located at 170mm distance from the laser scanner. The number of sample points between 135 - r mm and 205 + r mm (where 35 is the systematic error of the laser scanner, and r is the radius of the object in mm) from the laser scanner was

calculated. The diameters were estimated based on these sample points. The result is shown in *Tab.* 3.2. The error was inversely proportional to the diameter, implying that larger objects presented themselves better in the scanning data.

**Table 3.1. Color effect on the laser scanner: brighter objects have a better detection.**

| **Color** | **white** | **yellow** | **blue** | **black** |
|---|---|---|---|---|
| **Sample points (Number)** | 182 | 180 | 172 | 97 |
| **Length (mm)** | 276.8 | 283.5 | 260.3 | 148.6 |
| **Distance (mm)** | 335.6 | 330.9 | 325 | 307.8 |
| **STD ($mm^2$)** | 5.43 | 4.74 | 7.24 | 11.91 |

To test the effect of ambient light on the laser scanning, the same flat white object used in the color testing was scanned several times under varying lighting conditions being 1) no light, 2) light from the left side, 3) right side, 4) center, and 5) all directions, as shown in *Fig.* 3.9. The result indicated that the lighting condition did not affect the scanner result significantly.

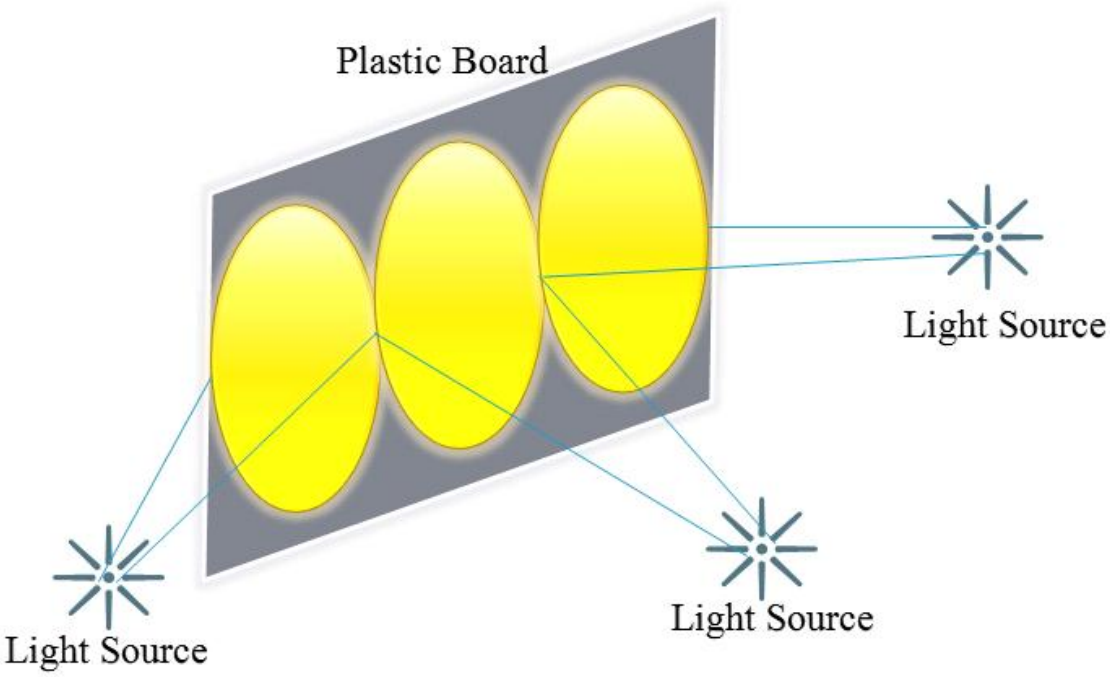


**Figure 3.9. 3D graphic of testing the effect of ambient light on the laser scanning.**

The reasons above explain why the *MxG* stems presented themselves as point sets along the radial direction as shown in *Fig.* 3.7. The same results were obtained by the diameter extraction method (*Fig.* 3.6).

**Table 3.2. Size effect on the laser scanner: larger objects are detected better.**

| **Objects** | **Object1** | **Object2** | **Object3** | **Object4** |
|---|---|---|---|---|
| **Real Diameter (mm)** | 13 | 17.86 | 27.02 | 33.62 |
| **Sample points (Number)** | 16 | 23 | 37 | 46 |
| **Estimated Diameter (mm)** | 11.1 | 16.3 | 26.8 | 33.5 |
| **Error (mm)** | 1.9 | 1.56 | 0.22 | 0.12 |

## 3.4.2 Clustering algorithm comparison

Three classical clustering techniques were compared with the GK clustering algorithm. They were the K-mean (KM) clustering algorithm, fuzzy C-Mean (FCM) clustering algorithm and the

Gath-Gave (GG) clustering algorithm. *Tab.* 3.3 shows the successful clustering result rate of these four clustering algorithms on a 30 data sets.

**Table 3.3. Clustering results among four algorithms on 30 data sets.**

| Clustering method | GG | KM | FCM | GK |
|---|---|---|---|---|
| **Successfully clustered number** | 5 | 9 | 23 | 29 |
| **Successfully clustered rate (%)** | 16.7 | 30 | 76.7 | 96.7 |

Figure 3.10 shows the result of these clustering algorithms for the data set shown in *Fig.* 3.3(a).

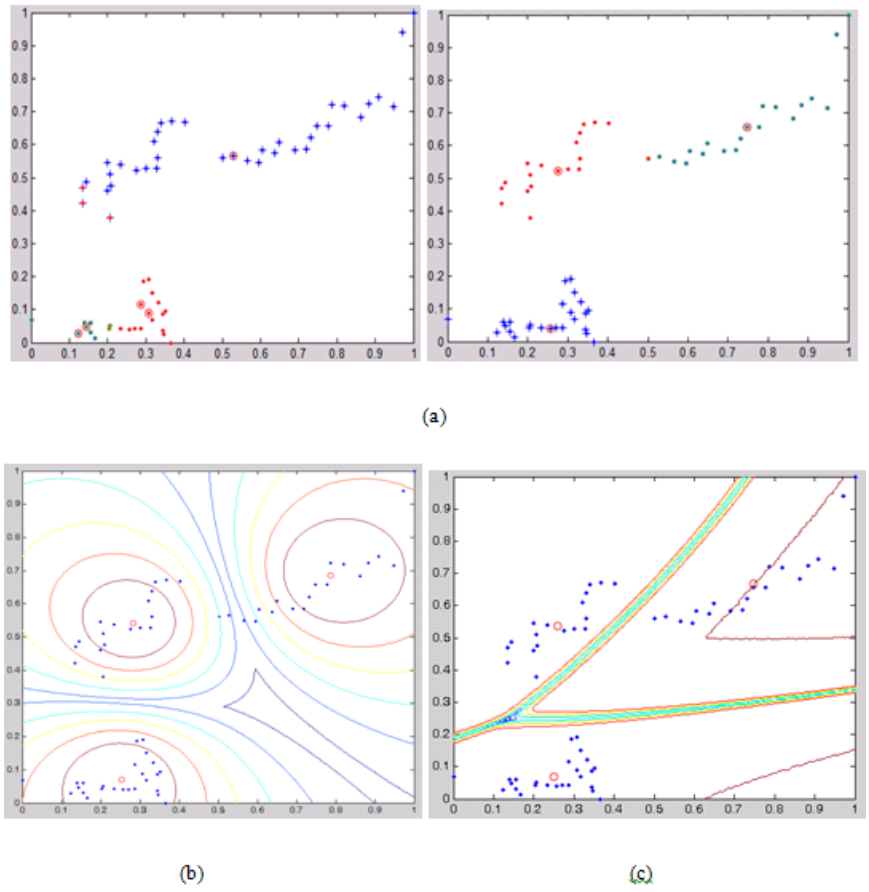


**Figure 3.10. Results of various clustering algorithms for the data set in *Fig*. 3.3(a). (a) Clustering results of KM clustering algorithm based different initial cluster centers. Left: inappropriately selected initial cluster centers. Right: well selected initial cluster centers. (b)**

**Clustering result of FCM clustering algorithm. (c) Clustering result of GG clustering algorithm.**

*Fig.* 3.10(a) shows the result of the KM clustering algorithm. The KM clustering algorithm was strongly dependent upon the positions of the initial cluster centers. If the initial cluster centers were well chosen, the clustering algorithm provided the correct clustering result (Right figure in *Fig.* 3.10(a)). However, if the initial cluster centers were selected incorrectly, erroneous clustering results were obtained by the KM clustering algorithms (Left graph in *Fig.* 3.10(b)). However, the centers of clusters cannot be accurately determined before clustering and need to be assigned at random. Among 30 data sets, only nine were successfully clustered (30%) based on randomly selected initial cluster centers. In contrast, for the GK clustering algorithm, 29 of the same 30 data sets (96.7%) were successfully clustered.

The principle of the FCM algorithm was similar to the GK clustering algorithm. Both algorithms attempt to minimize the object function in *Eqn.* 3.12. Unlike the GK clustering algorithm, the FCM algorithm uses the same norm inducing matrix $A$, which described the shape of the cluster, for every cluster in *Eqn.* 3.13. Thus, the clusters detected by the FCM clustering algorithm were all in the same shape and orientation (determined by the norm inducing matrix $A$). As shown in *Fig.* 3.10(b), all three clusters have a similar shape. Since the *MxG* stems presented themselves in different shapes and orientations, the GK clustering was shown to yield superior results. Figure 3.11. (a) shows an example of the results comparison between the GK clustering algorithm based method and FCM clustering algorithm based method. Seven stems were detected by the FCM clustering algorithm with an estimated diameter of 10.9mm, and nine stems were detected by the GK clustering algorithm with an estimated diameter of 12.1mm. The manually measured average diameter of the stems was 11.6mm among

the seven stems, and 11.5 mm among nine stems. In the 30 data sets, 23 (76.7%) data sets were successfully clustered by the FCM clustering algorithm. Thus, the GK clustering algorithm based method had a higher accuracy and detection rate than the FCM clustering based method.

Unlike the FCM and GK clustering algorithms, which are based on the inner-product norm, the GG clustering algorithm is based on a distance norm (*Eqn.* 3.27) and fuzzy maximum likelihood estimations (Bezdek and Dunn, 1975).

$$D_{ik}(p_k, v_i) = \frac{\sqrt{\det(F_{wi})}}{a_i} \exp\left(\frac{1}{2}(p_k - v_i^{(l)})^T F_{wi}^{-1}(p_k - v_i^{(l)})\right) \qquad (3.27)$$

Where $F_{wi} = \dfrac{\sum_{k=1}^{N} (\mu_{ik})^w (p_k - v_i)(p_k - v_i)^T}{\sum_{k=1}^{N} (\mu_{ik})^w}$ is the fuzzy covariance matrix of the i$^{th}$ cluster, and

$a_i = \dfrac{1}{N}\sum_{k=1}^{N} \mu_{ik}$ is the prior probability (The average of the probability of $N$ points belong to this cluster) of i$^{th}$ cluster.

Thus, the GG clustering algorithm can provide better defined clustering boundaries than the FCM and GK clustering algorithms, as shown in *Fig.* 3.10(c). However, if the number of data samples in a cluster was relatively small (or the number of clusters was relatively large) the matrix $F$ in *Eqn.* 3.15 became singular, which caused the GG clustering algorithm to fail. This problem occurred when predicting the total cluster number. Among 30 data sets, only 5 (16.7%) were successfully clustered by the GG clustering algorithms. Based on the analysis above, the GK clustering algorithm was applied due to its higher successful clustering rate and accuracy.

### 3.4.3 Feature extraction

As mentioned above, the location information was the only known parameter in the data set. The laser scanner provided the angle and the distance for each sample point in polar coordinates, and the position of the device was regarded the origin. Thus there were four parameters, which were the polar angle in the polar coordinates, the radius in polar coordinates, the X axis and Y axis in Cartesian coordinates. To select the features to be fed to the clustering algorithm, they were grouped into pairs based on their measured coordinates. The first group of features was the position information in polar coordinates. An example of the clustering results based on these two features is shown in *Fig.* 3.11. (b). Nine stems were detected based on these features. The number of detected *MxG* stems was 11, after applying the features in Cartesian coordinates (*Fig.* 3.6) on the same data set.

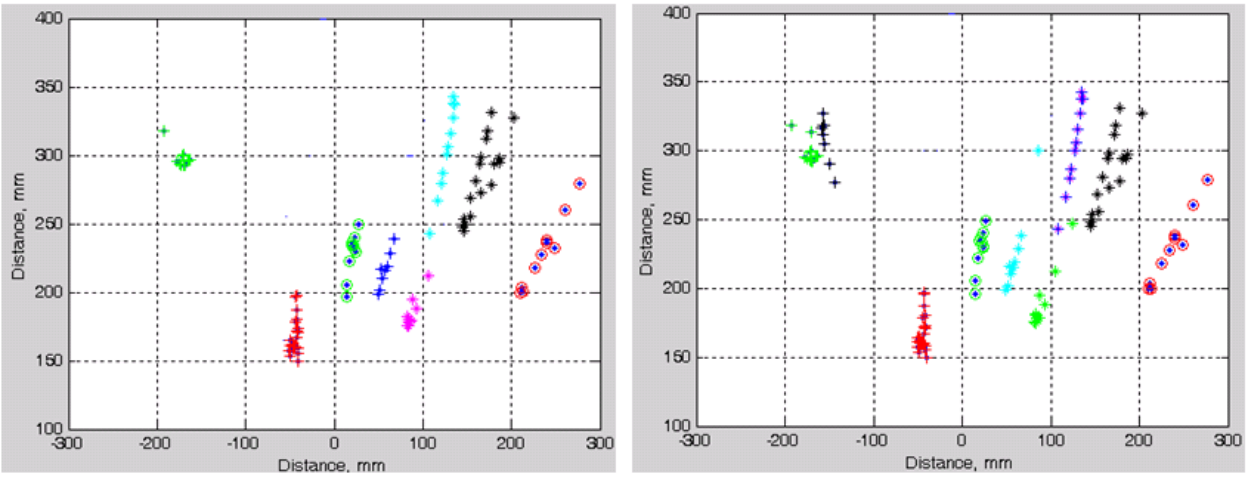


**Figure 3.11. Clustering result of Cartesian coordinates feature based FCM clustering algorithm and Polar coordinates feature based GK clustering algorithm. (a) Clustering result of the same data set in *Fig.* 3.6 based on the FCM clustering algorithm. (b) Clustering result using features from Polar coordinates based on the GK clustering algorithm. Different combination of colors and symbols present different *MxG* stems.**

Ten data sets were tested using these two groups of features. 63 *MxG* stems with an average estimated diameter of 10.57mm were detected based on polar coordinates features, and 70 *MxG* stems with an average estimated diameter of 11.40mm were detected based on Cartesian coordinate features. Cartesian coordinate features provided a higher detection rate. This was because in the data sets, which contained multiple *MxG* stems that needed to be clustered, the polar angle differences between two neighboring sampling points were always 0.25 degree, which was the angle resolution of the laser scanner. This influenced the process of choosing the optimal cluster number, which led a lower number of detected *MxG* stems in the algorithm. When using the features in the Cartesian coordinates, the differences between neighboring sample points were all different. In the 30 data sets, 29 (96.7%) were successfully clustered using the features in Cartesian coordinates, while 24 (80%) were successfully clustered using the features in Polar coordinates. Thus, the appropriate features fed to the clustering algorithm were the position information in the Cartesian coordinates.

### 3.4.4 Field test evaluation

To evaluate the performance of the method described, five locations were randomly chosen in a 10 by 10 m *MxG* plots, at the University of Illinois SoyFACE location in Champaign County, Illinois (lat/lon: 40.042455,-88.237943). At each location, five scans were performed, and 10 out of 25 scans were randomly chosen among all data sets. Within these 10 scans, 70 valid *MxG* stems were detected, and diameters of 70 *MxG* stems within the ROI (400mm) were manually measured at each location. Figure 3.11 shows the measurement results and the manually measured counterparts. The average of the manually measured *MxG* stems was 12.33mm, and the average of estimated diameters from laser scanner data using the method was 11.4mm. The

error was 0.93mm on average, or 7.5% of the average manually measured diameter. The tangential resolutions for each estimated stems were calculated based on *Eqn.* 3.1. The average tangential resolution of all 70 estimated *MxG* stem diameters was 1.13mm. Thus, if there was one sample point grouped into a wrong cluster, it would cause 1.13mm difference in the estimated result. Based on the results shown in *Fig.* 3.11, the average error between estimated diameter and manually measured diameter was one sampling point.

The reasons for this error are listed below. The accuracy limitation of the laser scanner limited the estimated results. In addition, the targets, *MxG* stems, were small, and it decreased their reflection rate. Both of these two reasons increased the clustering difficulty. Noise in the field caused by wind or leaves probably contributed to the error as well. In addition, incorrectly clustered sample points lowered the accuracy.

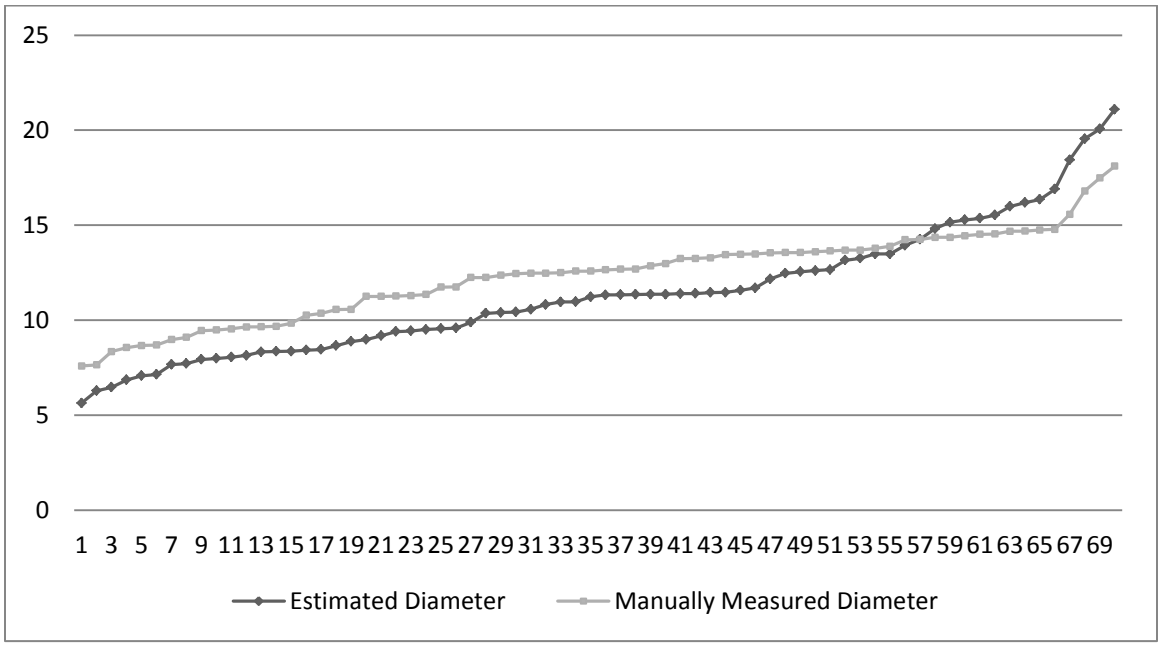


**Figure 3.12. Results comparison between clustering algorithm measurements and manual measurements. x axis is the stem number, y axis is the value of diameter in mm. The results were sorted in ascending order.**

## 3.5 Summary and Conclusions

A laser scanner based method was developed to automatically measure the diameters of *MxG* stems. The stem diameter was considered an important parameter to estimate yield in real-time. The laser scanner data contained the position information of *MxG* stems with the laser scanner as the origin. Based on the presentation of *MxG* stems, a clustering based method was developed to extract the diameter information.

A Region of Interest (ROI) was defined based on the tangential resolution of the laser scanner. The sample points within the ROI were pre-grouped using angle continuity. All samples were grouped into either single stem groups or multiple stem groups. A clustering algorithm was applied on the multiple stem groups to separate the data into data containing only a single stem. The diameter information of *MxG* stems was extracted based on a geometric model of *MxG* stems for the data groups containing single stem and clustered data sets.

Four clustering algorithms (K-mean (KM) clustering algorithm, fuzzy C-Mean (FCM) clustering algorithm, Gath-Gave (GG) clustering algorithm and (GK) clustering algorithm) were tested. Based on their performances, the GK clustering algorithm was regarded superior. Various combinations of features fed to the cluster were tested to evaluate the clustering result, and stems represented in Cartesian coordinates were used as features and fed to the clustering algorithm.

The method was shown feasible to extract diameter information of *MxG* stems in the field. Based on 10 randomly chosen scanning data sets, 70 *MxG* stems were detected, and the average of the estimated diameters was 11.4mm. 70 *MxG* stems around the scanning points were randomly selected as references. The manually measured average diameter of these *MxG* stems was 12.3mm. The error was 0.93 mm, which was 7.5% of the manually measured *MxG* stem

diameters. The possible sources of error were interference in the field, such as wind and leaf residuals, incorrectly clustered samples and the limited resolution of the laser scanner.

# CHAPTER 4
# A STEREO VISION BASED STEM DIAMETER SENSOR

## 4.1 Introduction

The LIDAR based stem diameter measurement introduced in chapter three was limited by the coverage area, dynamic measurement support and device cost. To improve the performance of stem diameter sensor and to aid researchers in determining the diameters of *Miscanthus Giganteus* (*MxG*) stems in an automated, high-throughput fashion, a high-accuracy stereo vision based diameter sensing system was developed. In addition, the developed system could be an integral part of a yield monitoring system for *MxG*, as well as being useful for validation of crop models.

The majority of previously developed diameter sensors in agriculture and forestry are based on photo-interruption and optical time-of-flight methods. Some examples were listed in section 3.1. However, neither of the sensor principles in the literature is suitable for measuring diameters of *MxG* stems in a field environment, due to the crop density and the fact that *MxG* grows in clumps rather than rows.

A stereo machine vision system is well suited to capture images of populations of stems, but, in order to measure the diameters of individual stems, they need to be separated. Ivanov *et al.*, (1995) used stereo vision to build a three-dimensional model of a maize canopy. Zhao and Aggarwal (2000) developed a method to reconstruct urban scenes by combining stereo vision and GPS. Lin *et al.* (2001) reported a method to reconstruct three-dimensional vegetable seedlings using stereo vision based three-dimensional graphical modeling. Takahash *et al.* (2002) developed a stereo vision based method for apple harvesting, which achieved a percentage accuracy of depth estimation of 95%. Bulanon *et al.* (2004) estimated the distance between apples and cameras using stereo vision. The reported accuracy percentage was 86% compared with manually measured results. Smit *et al.* (2004) developed a stereo vision module to calculate a real-time depth map for an agricultural vehicle. Rovira-Más *et al.* (2008) applied stereo vision to construct three-dimensional terrain maps. Finally, Jin and Tang (2009) developed a corn plant sensing system based on stereo vision.

The main limitations of the methods reported in the literature with regard to *MxG* diameter estimation were 1) the complicated background of *MxG* images in the field, 2) the absence of significant features for image matching and 3) the higher accuracy requirement, since the size of the *MxG* diameter is small (5-20mm) and the crop density is high (*Fig.* 1.1).

To accommodate the unique requirements, a novel stereo vision based method was developed. Stereo vision has the advantage of being able to capture images of groups of *MxG* stems. The *MxG* stems were detected and identified based on features provided by a laser sheet. This method simplified the image matching process of a traditional stereo vision method. Based on experiments, using manually measured *MxG* stem diameters as references, the method

achieved an accuracy of 99.8% (0.02mm) for average diameter estimation, and an average accuracy of 93.1% (0.60mm) for individual *MxG* stem diameter estimation.

The objective of this research was to 1) Identify *MxG* stems in images 2) extract the depth information of each identified *MxG* stems 3) estimate the stem diameters of identified stems.

## 4.2 Materials

To obtain high-quality images of *MxG* stems, a stereo imaging system was developed. This system (*Fig.* 4.1(b) and (b)) consisted of two Unibrain® Fire-i 701c color cameras and a slanted laser sheet generator. The cameras featured a 1/2" progressive scan CCD solid-state image sensor (ICX205AK, Sony Co. LTD) allowing resolutions ranging from 320 x 240 to 1280 x 960 pixels. Both gray scale and YCrCb color images can be captured with a capture speed ranging from 1.875 to 20 frames per second. Each camera was fitted with a C-mount 6mm F1.2 lens (Pentax Co.). The aperture and focal distance of the lens can be manually adjusted by a diaphragm ring and a focal ring. Two cameras were placed side by side and mounted on a frame at a mutual distance of 75 mm.

To generate the laser sheet for structured lighting, a 50 mW laser pointer with a wavelength of 532nm (visible green) was fitted with a Fresnel lens. The angle between the laser sheet and the cameras optical axis plane was 15 degrees. The camera module was connected to a portable computer (Dell®, Studio 1555) through an IEEE1394 (FireWire®) bus. Two 12 Volt batteries were provided as an external power supply for the cameras.

A Matlab®/C++ application was developed to configure the camera module and acquire images. The images were collected in an experimental field in Urbana-Champaign, Illinois

(lat/lon: 40.040963,-88.224565) in the spring and fall of 2010 and the spring of 2011. All images were captured in the YCrCb color space, at a resolution of 640x480 pixels, and formatted as Bitmap Image Files.

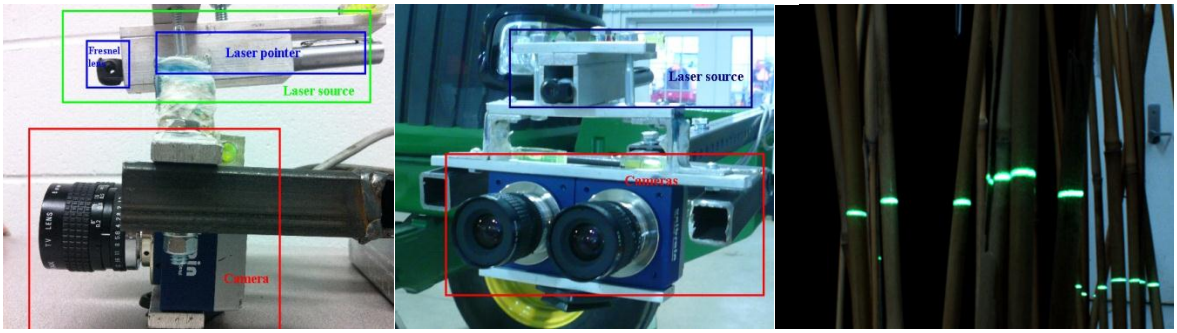


(a) (b) (c)

**Figure 4.1. Sensor module and captured image. (a) Side view of sensor module (b) Front view of the sensor module, consisting of two cameras combined with a laser sheet (c) Laser interception marks provided by the laser sheet.**

## 4.3 Methodology

To extract the diameters of *MxG* stems from images, several procedures were designed (*Fig.* 4.2): Two cameras captured images of an identical scene simultaneously. These images were white balanced and converted into the RGB color space, and the white balanced images were rectified based on the cameras' intrinsic and extrinsic parameters, which were obtained through calibration.

The depth information can be extracted based on laser marks in the images, which will be discussed in chapter 5. The features (laser marks, *Fig.*4.1(c)) were detected based on a color based image segmentation algorithm applied to the image pair. They were matched between the image pair in both one-dimensional epipolar geometry based matching constraints and two-dimensional pixel similarity based matching. The depth information was obtained based on the

matching disparities. Subsequently, *MxG* stems were identified based on the features (laser marks). Combining the identified targets, the horizontal covered length per pixel (obtained by calibration), and depth information, the diameter of *MxG* stems were obtained. The procedure flow chart of the developed sensor in this charpter was shown in *Fig.* 4.2.

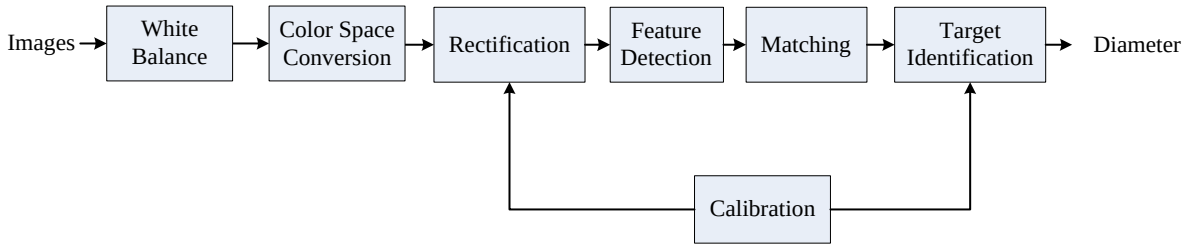


**Figure 4.2. Procedure flow chart of the stereo vision based diameter sensor for *MxG*.**

### 4.3.1 White balance and color space conversion

For a digital camera, each recorded pixel value is dependent upon the color temperature of the light source. For example, a white object will appear reddish under a low color temperature, and will appear bluish under a higher color temperature (Liu *et al.*, 1995). To correct the image to its canonical light source lit equivalent, an automatic white balance method was applied (Weng *et al.*, 2005). The chosen method has the advantage of operating in the YCrCb color space, which is the original color space of the captured images, reducing the computational cost.

To select the candidate reference white points, the near white region was first defined as a set of pixels that satisfy the following equations:

$$\begin{cases} \left|C_b(i,j) - (M_b + D_b \times sign(M_b))\right| < 1.5D_b \\ \left|C_r(i,j) - (1.5 \times M_r + D_r \times sign(M_r))\right| < 1.5D_r \end{cases} \quad (4.1)$$

Where $C_b(i, j)$ and $C_r(i, j)$ are chromaticity values of pixel $(i, j)$. $M_b$ and $M_r$ are respective mean values of $C_b(i, j)$ and $C_r(i, j)$. $D_b$ and $D_r$ are the average absolute differences, which were calculated as follows:

$$\begin{cases} D_b = \dfrac{\sum_{i,j}(|C_b(i, j) - M_b|)}{N} \\ D_r = \dfrac{\sum_{i,j}(|C_r(i, j) - M_r|)}{N} \end{cases} \quad (4.2)$$

Subsequently, the image was converted into the RGB color space by the following equation (Poynton, 1996):

$$\begin{cases} R = Y + 1.402(C_r - 128) \\ G = Y - 0.34414(C_b - 128) - 0.71414(C_r - 128) \\ B = Y + 1.772(C_b - 128) \end{cases} \quad (4.3)$$

For each pixel, *R*, *G* and *B* are values of the red, green and blue components in the RGB color space, and *Y* is the luminance value in the YCrCb color space. In the near white region that was obtained using *Eqn.* 4.1, the top 10% pixels were selected as reference white. Subsequently, the channel gains in the RGB color space were calculated by:

$$\begin{cases} R_{gain} = \dfrac{Y_{\max}}{\overline{R}} \\ G_{gain} = \dfrac{Y_{\max}}{\overline{G}} \\ B_{gain} = \dfrac{Y_{\max}}{\overline{B}} \end{cases} \quad (4.4)$$

Where, $R_{gain}$, $G_{gain}$ and $B_{gain}$ are the red, green and blue channel gains in the RGB color space. $\overline{R}$, $\overline{G}$ and $\overline{B}$ are the means of the reference white pixels in the RGB color space for three

channels. $Y_{\max}$ is the maximum luminance value of all pixels in the YCrCb color space. The white balanced pixels in RGB color space were presented as:

$$\begin{cases} R = R \times R_{gain} \\ G = G \times G_{gain} \\ B = B \times B_{gain} \end{cases} \quad (4.5)$$

## 4.3.2 Calibration and image rectification

The calibration process includes four sections: 1) camera calibration 2) distortion-correction and rectification 3) disparity-depth model and 4) depth-coverage area per pixel model.

### 4.3.2.1 Camera Calibration

To reconstruct three-dimensional information, a camera calibration process is required (Tsai, 1987). For a stereo vision system, the poses and positions of cameras in the system can be determined, and the radial and tangential distortions can be corrected by camera calibration. Both intrinsic parameters, presenting camera geometric and optical characteristics, and the extrinsic parameters, presenting the three-dimensional position and orientation of the camera frame relative to a certain world coordinate system are obtained by camera calibration. A camera model (Heikkilä and Silven, 1997) and a maximum-likelihood estimation based camera calibration algorithm (Zhang, 1999) were applied. Each camera was calibrated individually based on a series of calibration plane images (20 images), which were captured from various view angles (*Fig.* 4.3). In each image, the corner related pixels were extracted, then, the coordinates of these pixels were obtained in both world coordinates and image coordinates. The ordinary least squares method was applied to calculate the relationship between the two coordinate systems. The intrinsic parameters including focal length, principal point, skew angle

and distortion coefficients and the extrinsic parameters including rotation matrix and translation matrix were obtained by camera calibration.

After calibrating the two cameras, the relationships between each camera coordinates and world coordinates were set up, as shown in *Eqn.* 4.6:

$$\begin{cases} C_{world} = R_1 \cdot C_{cam1} + T_1 \\ C_{world} = R_2 \cdot C_{cam2} + T_2 \end{cases} \quad (4.6)$$

Where $C_{world}$ are the world coordinates, $C_{cam1}$ and $C_{cam2}$ are the camera coordinates. $R_1, R_2$ are the rotation matrices of two cameras. $T_1, T_2$ are the translation matrices of the two cameras. Then, the relative position of two cameras can be denoted by:

$$C_{cam1} = R_1^{-1} \cdot R_2 \cdot T_2 \cdot C_{cam2} + R_1^{-1}(T_2 - T_1) = RC_{cam2} + T \quad (4.7)$$

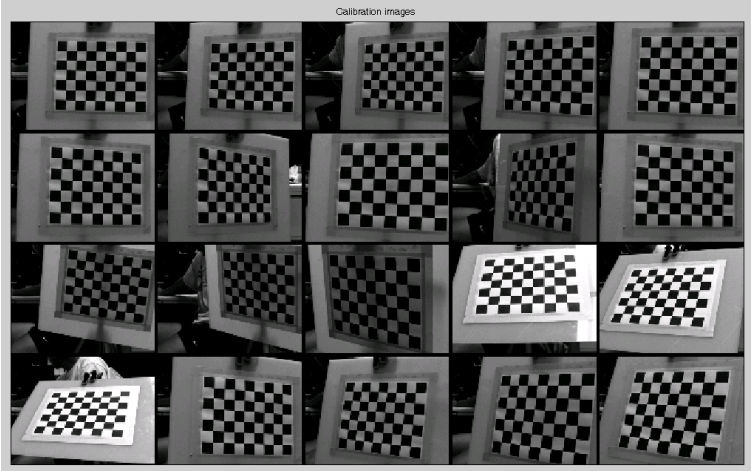


**Figure 4.3. Calibration plane images used for camera calibration.**

#### 4.3.2.2 Distortion correction and rectification

To obtain stereo-based high accuracy measurements, the tangential and radial distortion needs to be corrected. Based on the camera distortion model (Brown, 1966), the relationship between distorted image and undistorted image is described as below:

$$\begin{bmatrix} x \\ y \end{bmatrix} = \begin{bmatrix} (1 + kc_1 r^2 + kc_2 r^4 + kc_5 r^6) \cdot \hat{x} + dx_1 \\ (1 + kc_1 r^2 + kc_2 r^4 + kc_5 r^6) \cdot \hat{y} + dx_2 \end{bmatrix} \quad (4.8)$$

Where,

$$\begin{bmatrix} dx_1 \\ dx_2 \end{bmatrix} = \begin{bmatrix} 2k_3 \hat{x}\hat{y} + k_4 \cdot (r^2 + 2\hat{x}^2) \\ k_3 \cdot (r^2 + 2\hat{y}^2) + 2k_4 \hat{x}\hat{y} \end{bmatrix} \text{ and } r = \sqrt{\hat{x}^2 + \hat{y}^2} \quad (4.9)$$

$[x, y]^T$ are the normalized coordinates in image plane with distortion, and $[\hat{x}, \hat{y}]^T$ are the normalized coordinates without distortion. $[kc_1, kc_2, kc_3, kc_4, kc_5]$ are the distortion coefficients obtained by camera calibration. The distortion correction of the image was applied using Eqns. 4.8 and 4.9.

To simplify the process of detecting matching points between image pairs, image rectification is required. Based on epipolar geometry, if the two cameras are aligned to be coplanar, the matching points in the image pairs will lie on a horizontal line parallel to the baseline between the cameras. The image rectification process reduces the searching of matching points from two-dimensional to a one-dimensional problem. An existing image pair rectification algorithm (Fusiello *et al.*, 2000) was applied in this chapter.

#### 4.3.2.3 Disparity-depth model

To measure the diameter of the *MxG* stems using the stereo vision system, the distance (depth) between the stems and the cameras is needed, since the pixel coverage area depends on the depth

information. Figure 4.4 shows the geometry of a stereo vision system. $O_R$ and $O_T$ represent the optical centers of the two cameras, $f$ is the focal length, $P$ is a point in world coordinates, $P'$ and $P''$ are the projected points of $P$ in an undistorted rectified image pair, $X_R$ and $X_T$ are the horizontal coordinate in image coordinates, Z is distance between $P$ and the baseline between the cameras, and B is the distance between the focal centers of the two cameras. The disparity $(X_R - X_T)$ and the depth Z have the following relationship.

$$\frac{B}{Z} = \frac{(B + X_T) - X_R}{Z - f} \Rightarrow Z = \frac{B \cdot f}{X_R - X_T} \qquad (4.10)$$

Therefore, the depth can be estimated using the disparity between images captured by the two cameras.

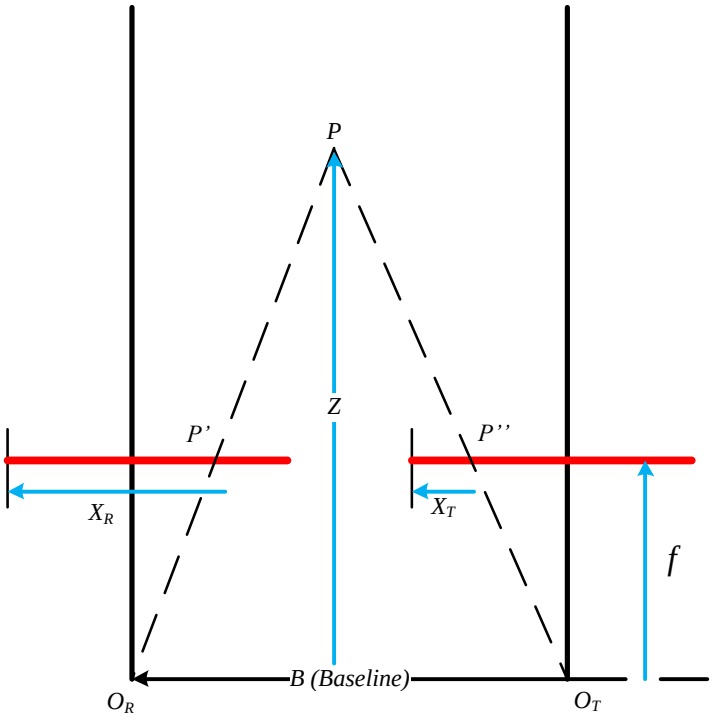


**Figure 4.4. Geometry of a stereo vision system.**

#### 4.3.2.4 Depth-horizontally covered length per pixel model

The pixel coverage area depends on the depth. The further the object is the smaller the coverage area per pixel is. As shown in *Fig.* 4.5, the depth is Z, the vertical angle of view is a and the horizontal angle of view is b, then coverage area per pixel and depth follow the following relationship.

$$S_{pixel} = \frac{2(\tan\frac{a}{2} + \tan\frac{b}{2})}{M \times N} \times Z \qquad (4.11)$$

Where $S_{pixel}$ is the coverage area per pixel, and $M \times N$ is the size of images (640x480 pixels ). Similarly, the horizontally covered length per pixel ( $L_{h\_pixel}$ ) is:

$$L_{h\_pixel} = \frac{2\tan\frac{b}{2}}{M} \times Z \qquad (4.12)$$

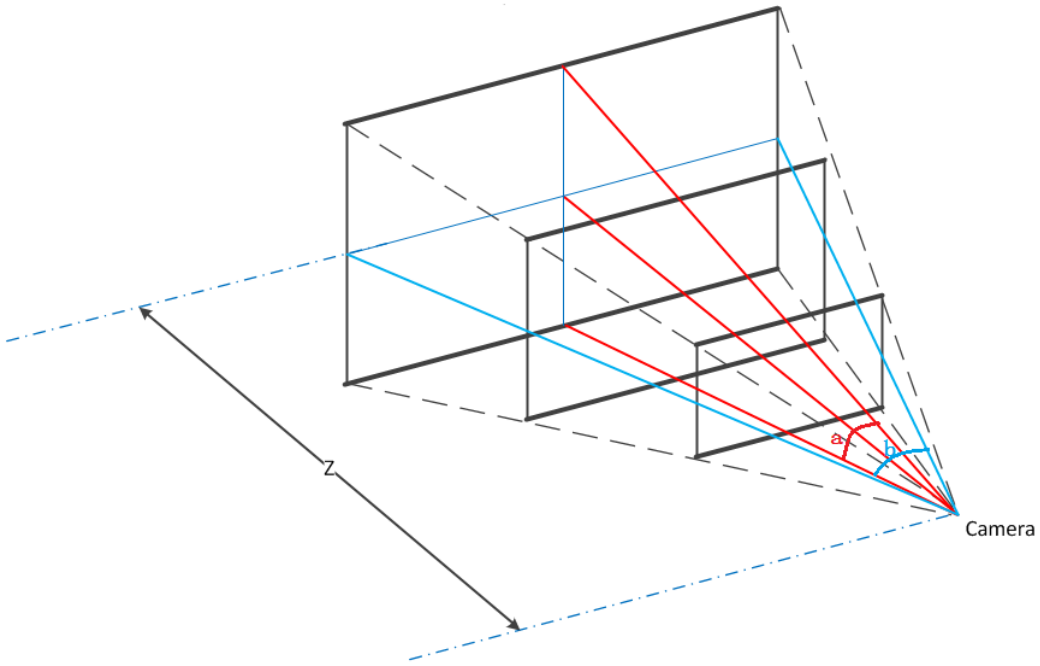


**Figure 4.5. Geometric model of the relationship between depth and coverage area.**

### 4.3.3 Feature detection

The features in the images are bright spots caused by the laser sheet interception on the *MxG* stems. These spots represent the diameters of *MxG* stems. To detect the features, a segmentation-based algorithm was developed. To decrease the ambient lighting influence, the mean values of the image pairs were adjusted to an experimentally determined value (43 in this case). The RGB color image was converted to a gray scale image using the following equation:

$$I_{Gray} = 0.2989 \times R + 0.5870 \times G + 0.1140 \times B \quad (4.13)$$

Where $I_{Gray}$ is the luminance of the grayscale image. The coefficients in *Eqn.* 4.13 were selected based on the rule of conversion between RGB color space to YIQ color space, which is used in NTSC color TV systems (Buchsbaum and Walter, 1975). The gray scale image was further converted to a binary image:

$$I_{WB} = \begin{cases} 1 & if \quad I_{Gray} > T_1 \\ 0 & if \quad I_{Gray} < T_1 \end{cases} \quad (4.14)$$

Where, $I_{WB}$ is the binary image converted from $I_{Gray}$, and $T_1$ is a threshold, which was equal to 70 in this case. A filter was applied to the images to remove connected areas (noisy points) with a size smaller than a threshold $T_2$ and larger than a threshold $T_3$, as shown in *Eqn.* 4.15.

$$S_i = \begin{cases} 1 & if \quad T_2 < area(S_i) < T_3 \\ 0 & else \end{cases} \quad (4.15)$$

Where $S_i$ is the $i^{th}$ connected area in the binary image. $T_2$ is 50, and $T_3$ is 450 .

For a connected area, orientation is defined as the angle between the x-axis and major axis of the ellipse that has the same second moments (area moment of inertia) as the region itself. As

shown in *Fig.* 4.6, the angle $r$ is the orientation of the connected area (white areas in *Fig.* 4.6). Because the valid features (the laser spots on the *MxG* stems) are horizontally oriented, the connected areas, whose orientations are larger than a threshold $T_4$ were removed, as shown in *Eqn.* 4.16.

$$S_i = \begin{cases} 1 & if \quad r_i < T_4 \\ 0 & else \end{cases} \qquad (4.16)$$

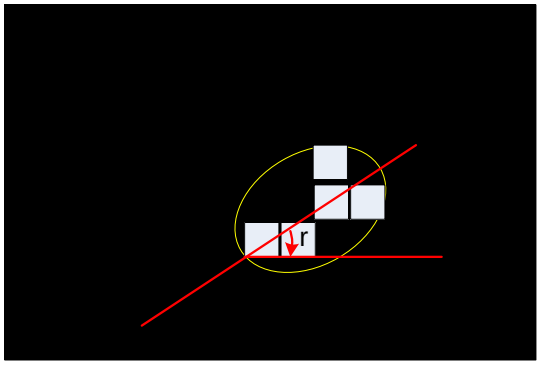


**Figure 4.6. Definition of orientation of a connected area in a binary image.**

*Fig.* 4.7(a) shows an example of a distortion-corrected, rectified image pair, and *Fig.* 4.7(b) shows the detected features in the images.

(a)

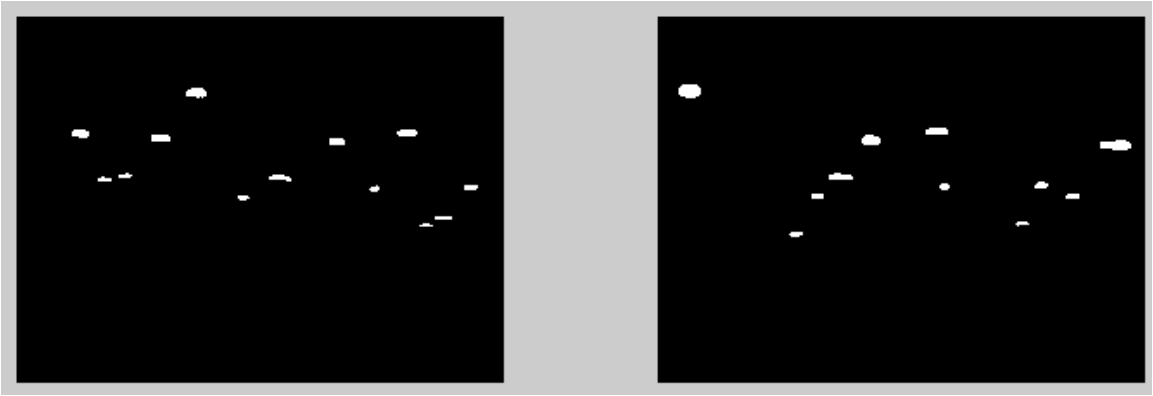

(b)

**Figure 4.7. Distortion coorected rectified image pair and detected features. (a) Example of a distortion corrected rectified image. (b) Detected features in (a).**

### 4.3.4 Image matching

Because the objects of interest in the image pair are only related to *MxG* stems, it is unnecessary to match the entire images. Instead, the only objects that need to be matched are the features in the image pairs. To match the features in the image pairs, the center of each remaining connected area was calculated by taking an average of all the coordinates of the points belonging to the area, as shown in the following equation:

$$\begin{cases} Xc_i = \dfrac{\sum X_k}{\mathrm{N}} & k = 1, 2, .... \\ Yc_i = \dfrac{\sum Y_k}{\mathrm{N}} & k = 1, 2, .... \end{cases} \qquad (4.17)$$

Where, $(Xc_i, Yc_i)$ are the coordinates in the image plane of the center of the $i^{th}$ connected area. $(X_k, Y_k), k = 1, 2, ....$ are the coordinates of all the pixels in the $i^{th}$ connected area.

Since the image pair is rectified, due to the epipolar geometry, the centers of the matched features appear in a line parallel to the baseline of the cameras. To search for the matched features, two similarity matrices were generated. One matrix ($M_{1D}$) represented the one-dimensional similarity between features in the image pair (*Eqn.* 4.18). The element of the one dimensional similarity matrix $M_{1D}(i, j)$ is the absolute value of the vertical difference between the $i^{th}$ feature in the left image and the $j^{th}$ feature in the right image.

$$M_{1D} = \begin{bmatrix} |YLc_1 - YRc_1| & |YLc_2 - YRc_1| & \cdots & |YLc_n - YRc_1| \\ |YLc_1 - YRc_2| & |YLc_2 - YRc_2| & \cdots & |YLc_n - YRc_2| \\ \vdots & \vdots & \ddots & \vdots \\ |YLc_1 - YRc_m| & |YLc_1 - YRc_m| & \cdots & |YLc_n - YRc_m| \end{bmatrix} \qquad (4.18)$$

Where $YLc_i$ is the vertical coordinate of the $i^{th}$ feature in the left image, and $YRc_j$ is the vertical coordinate of the $j^{th}$ feature in the right image, assuming *n* features in the left image and *m* features in the right image.

The corresponding matrix $M_{2D}$ represents the two-dimensional similarity between features in the image pair. Using each $(Xc_i, Yc_i)$ as the center created a 64x64 pixel window for each feature (the size of windows might change depending on the distance to the cameras). The element in

this two dimensional similarity matrix $M_{2D}(i,j)$ is the mean value of the absolute differences between pixels in $i^{th}$ window in left image and pixels in $j^{th}$ window in right image.

$$M_{2D}=\begin{bmatrix} mean(|WL_1-WR_1|) & mean(|WL_2-WR_1|) & \cdots & mean(|WL_n-WR_1|) \\ mean(|WL_1-WR_2|) & mean(|WL_2-WR_2|) & \cdots & mean(|WL_n-WR_2|) \\ \vdots & \vdots & \ddots & \vdots \\ mean(|WL_1-WR_m|) & mean(|WL_2-WR_m|) & \cdots & mean(|WL_n-WR_m|) \end{bmatrix} \quad (4.19)$$

Where $WL_i$ is the $i^{th}$ window in the left image, and $WR_j$ is the $j^{th}$ window in the right image.

The matching algorithm started by finding the minimum value ($Min^{1D}{}_i$) in each column of $M_{1D}$, where the row index ($j$) (the $j^{th}$ feature in right image) of this detected minimum value in $M_{1D}$ was considered as the candidate matched feature of the $i^{th}$ feature in left image. This process followed the steps below:

**Step 1**: If $T_5$ $Min^{1D}{}_i$ ($T_5=5$), it was assumed that there is no matched feature in the right image. This feature was discarded. Go to Step 2.

**Step 2**: If $Min^{1D}{}_i = Min^{1D}{}_j = k$ (conflicted match), check the $M_{2D}$, if $M_{2D}(i,k) < M_{2D}(j,k)$, $Min^{1D}{}_i = k$ and $Min^{1D}{}_j$ = next smallest value in $j^{th}$ column of $M_{1D}$. Go to step 1. If there is no conflicted match, go to step 3.

**Step 3**: Check all the remaining matched pairs $(i,j)$. If $M_{2D}(i,j) > T_6$ ($T_6=200$), this pair was discarded.

The value of $T_5(5)$ and $T_6(200)$ was selected based on experimental results. The remaining feature pairs were considered matched pairs. Figure 4.8 shows an example result of image matching. The matched pairs are labeled by boxes with the same color in the image pair.

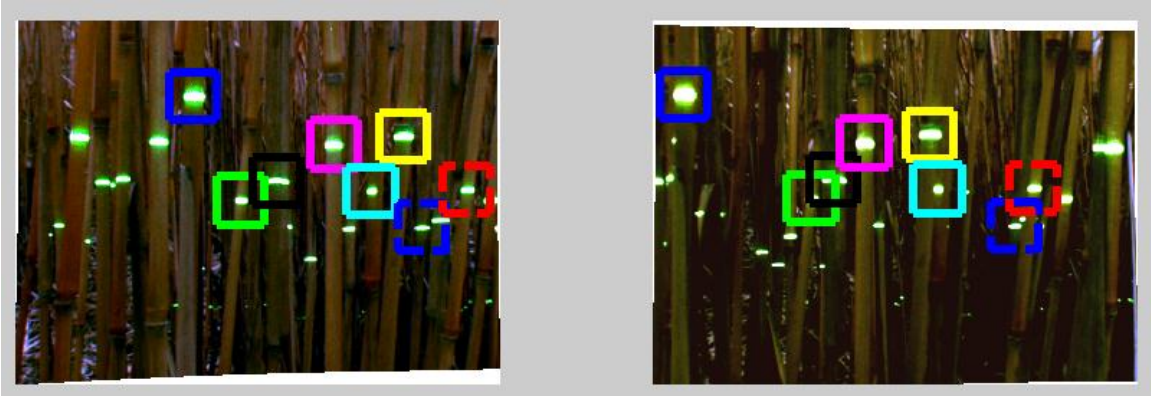

**Figure 4.8. Example result of image matching. Features denoted by identical line colors are matched pairs.**

### 4.3.5 Diameter information extraction

The disparity of each target (feature) was obtained by the matched feature pairs.

$$D_{(i,j)} = \left| XLc_i - XRc_j \right| \qquad (4.20)$$

Where $D_{(i,j)}$ denotes the disparity of $i^{th}$ object in the left image ( $j^{th}$ object in right image). $XLc_i$ is the horizontal coordinate of the center of $i^{th}$ object in the left image, and $XRc_j$ is the horizontal coordinate of the center of $j^{th}$ object in the right image. Both $XLc_i$ and $XRc_j$ are in image coordinates.

Subsequently, based on the disparity - depth model, which predict the depth based on disparity, the depth information ( $Z_{(i,j)}$ ) of the $i^{th}$ object in left image (the $j^{th}$ object in right image) was obtained by applying *Eqn.* 4.10.

$$Z_{(i,j)} = \frac{B \cdot f}{D_{(i,j)}} \quad (4.21)$$

After obtaining the disparity information, the horizontal length of each target was calculated as follows:

$$L_{(i,j)} = \frac{(\max(X_{i,k}) - \min(X_{i,k})) + (\max(X_{j,l}) - \min(X_{j,l}))}{2} \qquad k,l = 1,2,... \quad (4.22)$$

Where $L_{(i,j)}$ is the length of the $i^{th}$ object in the left image (the $j^{th}$ object in right image) in pixels. $X_{i,k}$ is the horizontal coordinate of the $k^{th}$ pixel in the $i^{th}$ object in the left image, and $X_{j,l}$ is the horizontal coordinate of the $l^{th}$ pixel in the $j^{th}$ object in the right image.

Based on *Eqn.* 4.12, the diameter ( $dia_{(i,j)}$ ) of $i^{th}$ object in the left image (the $j^{th}$ object in the right image) was calculated as:

$$dia_{(i,j)} = \frac{2\tan\frac{b}{2}}{M} \times Z_{(i,j)} \times L_{(i,j)} \quad (4.23)$$

## 4.4 Results and Discussion

This section consists of four parts, 1) camera calibration results, 2) disparity-depth model, 3) depth-horizontally covered length model and 4) field tests results, which are described in sequence.

### 4.4.1 Camera calibration

The intrinsic parameters of two cameras obtained by camera calibration are shown in *Tab.* 4.1. The extrinsic parameters are shown in *Eqn.* 4.24.

**Table 4.1. Intrinsic parameters of two cameras.**

| | **Left camera** | **Right camera** |
|---|---|---|
| **Focal Length (pixel)** | [1327.87, 1323.87] | [1334.82, 1334.28] |
| **Principal point (pixel)** | [238.83, 147.21] | [265.75, 102.25] |
| **Skew angle (degree)** | 90 | 90 |
| **Distortion coefficients** | [ -3.36, 4.11, 0.04, 0.07, 0 ] $\times 10^{-1}$ | [-2.95, 0.63, 0.03, 0.03, 0] $\times 10^{-1}$ |

$$\begin{cases} R = \begin{bmatrix} 0.9999 & -0.0043 & 0.0096 \\ 0.0043 & 0.9998 & 0.0202 \\ -0.0097 & -0.0202 & 0.9997 \end{bmatrix} \\ T = [-58.6100 \quad 0.0265 \quad 9.3362]^T \end{cases} \qquad (4.24)$$

Where $R$ and $T$ are the rotation matrix and the translation matrix in *Eqn.* 4.7. The rotation matrix ($R$) is close to the unit matrix. This implies that the relative position of the two cameras were close to the ideal parallel placement. However, there was still an installation error. The translation matrix ($T$) had shown that the optical center of the two cameras virtually lied in the same plane (the relative small second component in $T$), while one camera was mounted higher (around 1 mm) than the other (the third component in $T$). The image rectification process compensated for this installation error.

### 4.4.2 Disparity-depth model

To set up the disparity-depth model (section 4.3.2.3), 11 image pairs of a calibration plane (*Fig.* 4.3) (30mm per square) with depths ranging from 200mm to 500mm were taken. *Tab.* 4.2 shows the measurements of disparities of square corners related pixels and the depths at which the images were taken.

**Table 4.2. Measurements of disparities and depths.**

| **Disparity (pixel)** | 440.3 | 378.4 | 325.5 | 289.5 | 258.5 | 247.2 | 226.8 | 202.2 | 186.4 | 181.3 | 171.5 |
|---|---|---|---|---|---|---|---|---|---|---|---|
| **Depth (mm)** | 200 | 230 | 260 | 290 | 320 | 350 | 380 | 410 | 440 | 470 | 500 |

A power function (Based on *Eqn.* 4.21) was applied to fit the points in *Tab.* 4.2 with the disparity as the *x* axis and depth as the *y* axis. Figure 4.9 (a) shows the curve fitting result. The points were fitted by the function:

$$f_1(x) = ax^b \qquad (4.25)$$

Where $a = 7.49 \times 10^4$ and $b = -0.98$, and the regression coefficient was 0.99.

*Eqn.* 4.24 has the same structure as *Eqn.* 4.10. It indicates that the experimental value of $B \cdot f$ in *Eqn.* 4.10 is $7.49 \times 10^4$. The measured length of the baseline was 60mm and the focal length of the camera was 1337.8 pixels based on camera calibration, therefore, the calculated value of $B \cdot f$ is $8.03 \times 10^4$. Since the experimental and the calculated result are similar, *Eqn.* 4.25 was applied as the disparity-depth model.

### 4.4.3 Depth-horizontally covered length per pixel model

Similar to the determination process of the disparity-depth model, to establish the relationship between depth and horizontally covered length per pixel, the numbers of pixels of a 30mm length edge in the same 11 image pairs used to set up the disparity-depth model were counted. Subsequently, the horizontally covered length per pixel was calculated by dividing 30mm by the number of pixels. The result is shown in *Tab.* 4.2.

Linear functions were applied to fit the points shown in *Tab.* 4.2 (depth as *x* axis, covered length per pixel as *y* axis) as shown in *Fig.* 4.9(b). The estimated function for the horizontally covered length per pixel in average is as follows:

$$f_2(x) = cx + d \qquad (4.26)$$

Where $c = 7.544 \times 10^{-4}$ and $d = 4.140 \times 10^{-2}$ , where the regression coefficient was 0.99.

*Eqn.* 4.26 has the same structure as *Eqn.* 4.12. It shows that the experimental value of $\frac{2\tan\frac{b}{2}}{M}$ in *Eqn.* 4.12 is $7.544 \times 10^{-4}$. In reality, the field of view ( $b$ ) of the cameras is 26 degrees, the length of an image ( $M$ ) was 640 pixels and the calculated value of $\frac{2\tan\frac{b}{2}}{M}$ is $7.215 \times 10^{-4}$. Again, the experimental result and the theoretical result were similar. Thus, *Eqn.* 4.26 was adopted as the relationship between depth and horizontally covered length per pixel.

**Table 4.3. Measurements of the depth and covered length per pixel for stereo vision cameras**

| **Depth (mm)** | 200 | 230 | 260 | 290 | 320 | 350 | 380 | 410 | 440 | 470 | 500 |
|---|---|---|---|---|---|---|---|---|---|---|---|
| **Covered length per pixel of left camera(mm/pixel)** | 0.11 | 0.13 | 0.16 | 0.18 | 0.20 | 0.22 | 0.25 | 0.27 | 0.29 | 0.32 | 0.34 |
| **Covered length per pixel of right camera(mm/pixel)** | 0.11 | 0.13 | 0.16 | 0.18 | 0.20 | 0.22 | 0.24 | 0.27 | 0.29 | 0.31 | 0.34 |
| **Covered length per pixel in average(mm/pixel)** | 0.11 | 0.13 | 0.16 | 0.18 | 0.20 | 0.22 | 0.25 | 0.27 | 0.29 | 0.32 | 0.34 |

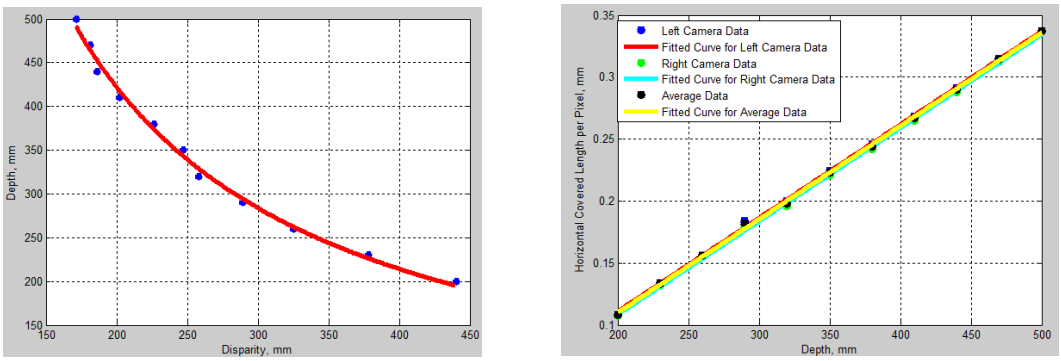


(a) (b)

**Figure 4.9. Relations among disparity, depth and horizontally covered length per pixel. (a) Relationship between disparity and depth. (b) Relationship between depth and horizontally covered length per pixel.**

### 4.4.4 Field evaluation

To evaluate the method described, tests were conducted in *MxG* fields in Urbana, Illinois (lat/lon: 40.040963,-88.224565), in the Fall of 2010 and the Spring of 2011. The sampling locations within the field were randomly selected.

100 *MxG* stems in 100 image pairs were randomly selected to evaluate the method. The estimated depths and diameters of *MxG* stems were compared with manually-measured depths and diameters. Figure 4.10 shows the depth estimation result.

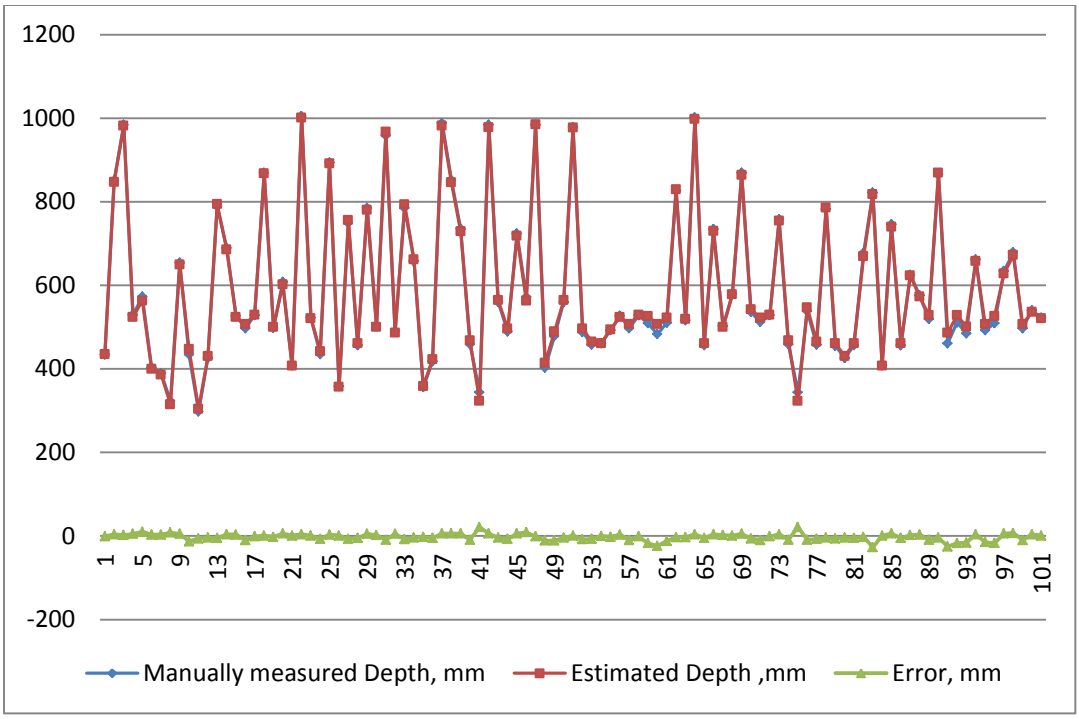


**Figure 4.10. Depth estimation result: the x-axis indicates the sample number of *MxG* stems, the y-axis indicates the depth in mm.**

The maximum depth of the selected *MxG* stems was 1005, while the minimum depth was 298mm and the mean depth was 590mm. The error between the estimated depth and the manually measured depth ranged from 0mm to 27mm with an average of 6.45mm and a standard deviation of 5.49. Thus, the depth estimation method achieved an accuracy of 98.90% (6.45mm) on average.

The diameter estimation result is shown in *Fig.* 4.11.

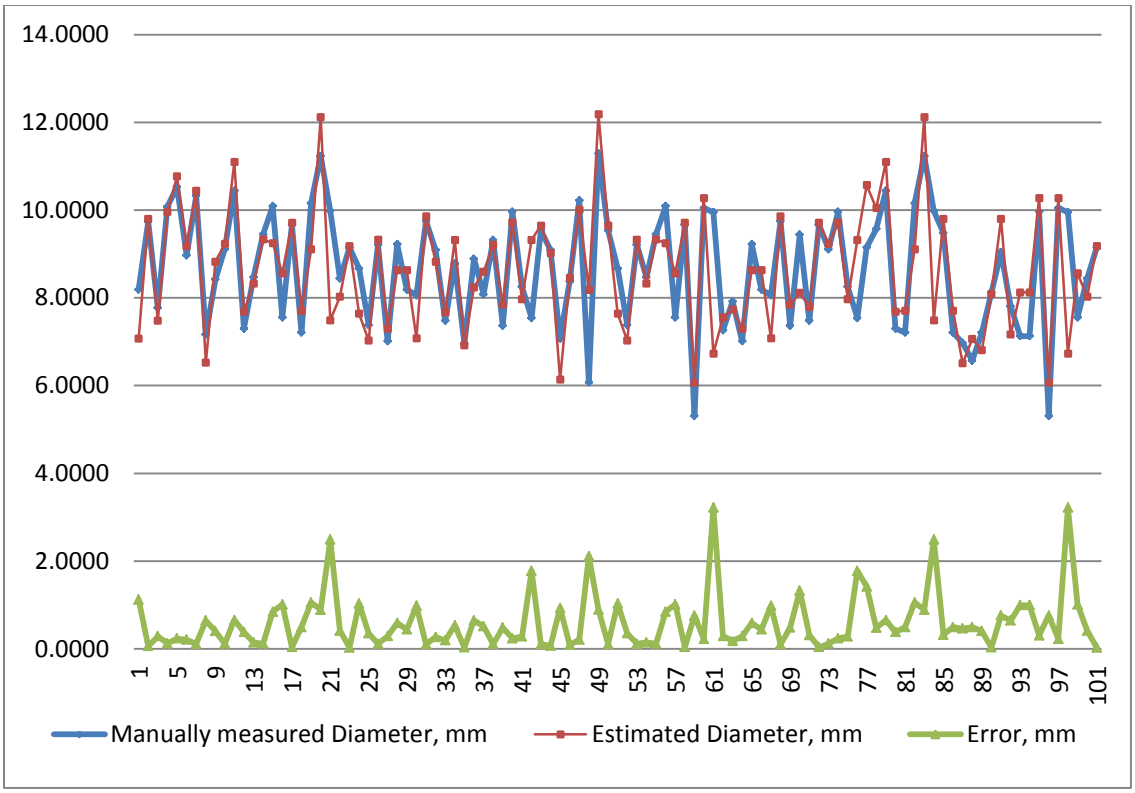


**Figure 4.11. Diameter estimation result: the x-axis indicates the sample number of *MxG* stems, and the y-axis indicates the diameter in mm.**

The manually measured diameters of selected *MxG* stems ranged from 5.31mm to 11.29mm with an average of 8.65mm. The estimated diameters ranged from 6.07mm to 12.18mm with an average of 8.63mm. The error of the average diameter was 0.02mm, achieving an accuracy of 99.80%. The error of manually measured diameters and the estimated diameters based on this research ranged from 0.03mm to 3.22mm with a mean of 0.60mm and a standard deviation of 0.63. Thus, the developed method achieved an accuracy of 93.10% (0.60mm).

In 100 image pairs, 471 diameters of *MxG* stems were estimated. 10 mismatching features were detected, leading to a valid estimation ratio of 97.8%.

## 4.5 Summary and Conclusions

Diameter is considered as an important yield related parameter of *MxG*. A vision-based *MxG* diameter sensor was developed. The sensor contained dual color CCD cameras and a green laser sheet generator. The cameras were employed to collected images in the YCrCb color space. The laser source illuminated the *MxG* stems, yielding features to match captured image pairs and identify *MxG* stems.

The captured image pairs were white balanced and converted to the RGB color space. Based on the cameras intrinsic and extrinsic parameters, which were obtained during camera calibration, the image pairs were rectified. The image rectification adjusted the image pairs as if they were acquired by two perfectly aligned cameras, and reduced the complexity of the following image matching process from two-dimensional matching to one-dimensional matching. The features (laser spots) in image pairs were detected by a segmentation algorithm, and they were matched by two similarity matrices based on epipolar geometry. The depth information of each matched feature pair was obtained by a disparity - depth model. The diameter information was extracted based on its depth information and a depth - horizontally coverage area per pixel model.

The relationship between the disparity and depth, and the relationship between the depth and horizontally covered length per pixel were obtained by both analysis and experiments and the experimental results corroborated the theoretical results. The diameter sensor and corresponding method were evaluated in a series of field tests. The results showed that the depth-disparity model achieved an accuracy of 98.9% (6.45mm) on average for depth estimation. The vision system based sensor achieved an accuracy of 99.8% (0.02mm) while estimating the average

diameter in field, and achieved an accuracy of 93.1% (0.60mm) on average for estimation of individual *MxG* stem diameters. The valid estimation rate ratio was shown to be 97.88%.

# CHAPTER 5
# A MONOCULAR VISION BASED STEM DIAMETER SENSOR

## 5.1 Introduction

Unlike traditional stereo vision systems, which employ dual cameras, a stereo vision system using a single camera is described in this chapter. Compared to the binocular vision system, a monocular system is of lower cost from both a commercial and computational point of view. The main difficulty in monocular stereo vision is to recover the depth information. Attempts of monocular vision systems are covered in the literature: Teoh and Zhang (1984) developed a monocular stereo vision system using a camera with two mirrors, which were fixed at a 45 degree angle with respect to the optical axis of the camera, and a third mirror mounted on a shaft, that rotated through 90 degrees. The depth information was recovered by using two sequential image acquisitions. Nishimoto and Shirai (1987) improved Teoh and Zhang's method. They placed a glass plate in front of the camera instead of using mirrors and two different views were provided by rotating the glass plate. The depth information was also obtained by two sequential image acquisitions. A similar method was described by Pachidis and Lygouras (2007). Their method also applied a rotating glass plate and two images to obtain depth information.

Matsumoto *et al.* (1997) reported on a monocular stereo vision system, which was based on image sequences. Criminisi *et al.* (2000) described a monocular prior-knowledge based vision system, where the depth information was obtained by comparing the height with an object of known height in the image. The depth information was sensed based on motion parallax. Multiple shots and iterative calculation were required for this method. Wang and Ishii (2009) developed a system to reconstruct depth information based on optical flow analysis. A speed sensor was required to estimate the acceleration in their method.

Either multiple sequential image acquisition, additional sensors or prior knowledge are required for the existing monocular stereo vision systems. In addition, the computational cost is relatively high for these methods, and their accuracy is relatively low. These disadvantages limit the potential of using the existing monocular vision system to measure the diameter of *MxG* stems.

Therefore, a novel monocular stereo vision based *MxG* diameter sensor was developed. The method applied a slanted laser sheet to provide features in images, and the depth information was obtained by geometry perspective analysis using a single image. The results showed that the proposed method achieved high accuracies in both depth and diameter estimation.

## 5.2 Materials

The same sensor arrangement as described in section 4.2 was applied in this chapter. A combination of an industrial color CCD camera (Unibrain® Fire-i 701 c) and a laser sheet generator were applied as the diameter sensor module. The accessible image size of the camera ranged from 320x240 to 1280x960 pixels with an image acquisition rate ranging from 1.875 to 20 frames per second. A C-mount 6mm F-1.2 lens (Pentax Co.) was fitted to the camera. The

camera required a 12 Volt external power supply, and an IEEE 1394 (FireWire®) cable to connect to a computer (Dell Studio 1555). The laser sheet provided identifiable features in the images. It was composed of a 50mW laser pointer and a Fresnel lens, which transformed the laser beam into a diverging laser sheet. The wavelength of the laser source was 532nm. Figure 4.1 shows the sensor module. A Matlab®/C++ based image acquisition application was developed to configure the sensor module and collect images. The images were captured in the Fall and Spring of 2011 in an experiment field in Champaign- Urbana. The captured images were in the YCrCb color space with a resolution of 640x480 pixels in BitMap format.

## 5.3 Methodology

The camera was calibrated before the image processing. The captured images were first preprocessed to achieve proper white balance, and converted into the RGB color space. Then, a geometrical analysis based method was used to obtain the depth information from a single image. The diameter information was obtained using the depth information and an image segmentation based target identification method.

### 5.3.1 Preprocessing

The preprocessing included camera calibration, image distortion correction, white balance and color space conversion. These processes were the same as described in section 4.3.2.1 (camera calibration), 4.3.2.2 (distortion correction and rectification) and section 4.3.1 (white balance and color space conversion).

### 5.3.2 Geometry perspective analysis based depth estimation

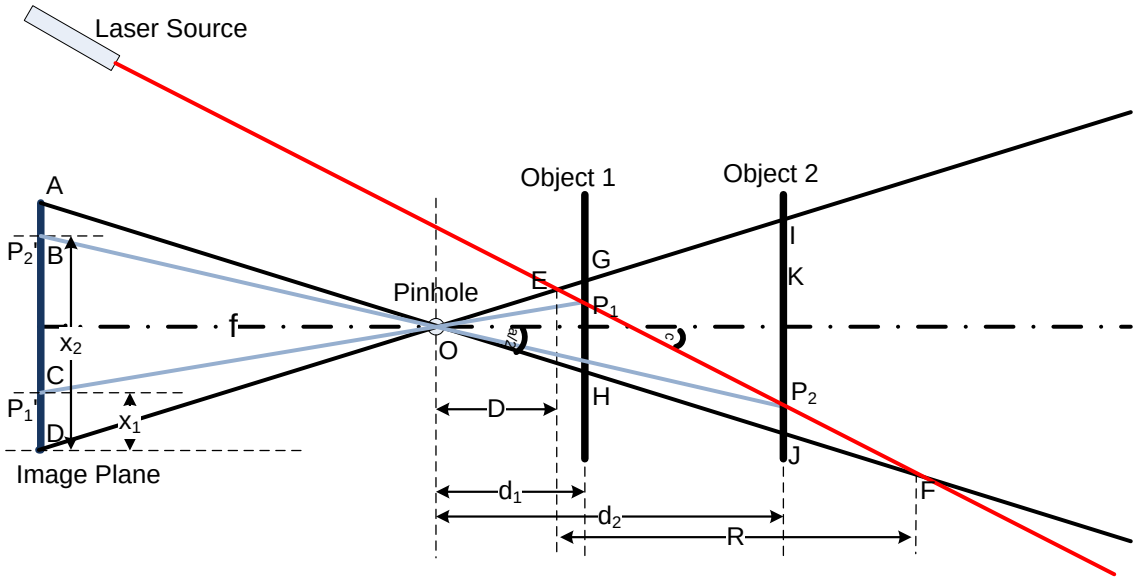


**Figure 5.1. Geometry perspective model of the diameter sensor unit.**

The distance between the objects in the image and the camera is required for three-dimensional reconstruction. Since a laser sheet was projected onto the *MxG* stems, the depth information was estimated using geometrical analysis.

Figure 5.1 shows a geometry perspective model of the sensor unit, assuming a pinhole camera model. The distance between the pinhole (O) and the image plane is f. Assume the distances between the pinhole and two objects (object 1 and object 2) are $d_1$ and $d_2$. The angle between the laser sheet and the optical axis of the camera is c, and the camera vertical field of view is the angle $\angle AOD$. The laser sheet intersects object 1 and object 2 at point $P_1$ and $P_2$. AD denotes the vertical edges of the image plane (A is the lower boundary and D is the upper boundary of the image), then, the visible area of object 1 is GH, while the visible area of object 2 is IJ, and the visible area of the laser sheet is EF. This means that point G on object 1, point I on object 2 and

point E on the laser sheet have the same vertical location in the image plane. Similarly, point H on object 1, point J on object 2, and point F on the laser sheet have the same vertical location as well. The projected point in image of point $P_1$ is C, and its vertical level is $x_1$. The projected point in the image of point $P_2$ is B, and its vertical location in the image is $x_2$. The horizontal distance between point E and the pinhole is D.

For object 1, the triangle $\triangle GOP_1$ is equal to triangle $\triangle DOC$ ($\triangle GOP_1 \cong \triangle DOC$). Thus,

$$\frac{CD}{f} = \frac{GP_1}{d_1} \tag{5.1}$$

Since,

$$\begin{cases} CD = x_1 \\ GP_1 = (d_1 - D)(\tan c + \tan\frac{a}{2}) \end{cases} \tag{5.2}$$

This transforms *Eqn.* 5.1 to:

$$\frac{x_1}{f} = \frac{(d_1 - D)(\tan c + \tan\frac{a}{2})}{d_1} \tag{5.3}$$

Then, the relationship between $d_1$ and $x_1$ is:

$$d_1 = \frac{D \cdot f \cdot (\tan c + \tan\frac{a}{2})}{f \cdot (\tan c + \tan\frac{a}{2}) - x_1} \tag{5.4}$$

Similarly, the triangle $\triangle IOP_2$ is similar to triangle $\triangle BOD$ ($\triangle IOP_2 \cong \triangle BOD$).

$$\frac{x_2}{f} = \frac{(d_2 - D)(\tan c + \tan\frac{a}{2})}{d_2} \Rightarrow d_2 = \frac{D \cdot f \cdot (\tan c + \tan\frac{a}{2})}{f \cdot (\tan c + \tan\frac{a}{2}) - x_2} \quad (5.5)$$

Based on *Eqn.* 5.4 and *Eqn.* 5.5 (they have the same form), the depth (d) and the vertical location in the image have the following relationship:

$$d = \frac{p}{q - x_2} \quad (5.6)$$

Where $q = f \cdot (\tan c + \tan\frac{a}{2})$ and $p = D \cdot q = D \cdot f \cdot (\tan c + \tan\frac{a}{2})$.

Once the sensor unit is set up, the relative positions of the camera and laser source are fixed and the parameters in *Eqn.* 5.6 (D, f, α and c) are constants. Thus, the depth information of each feature (laser spot) can be obtained using a single image, based on its vertical level in the image.

### 5.3.3 Target identification and diameter estimation

The *MxG* stems were identified by detecting the features in images. The same method introduced in section 4.3.3 (feature detection) was applied to detect the features (laser spots). Figure 5.2 shows an example of a distortion corrected image and the corresponding detected features in the image.

(a) (b)

**Figure 5.2. Distortion corrected image example and detected features. (a) Example of distortion corrected image. (b) Detected features in (a).**

The depth information of each connected area (*MxG* stem) ( $Z_i$ ) was computed by

$$Z_i = \frac{\mathrm{p}}{\mathrm{q} - Yc_i} \qquad (5.7)$$

Where $Yc_i$ is the vertical coordinate of the center of the $i^{th}$ connecting area in the image. $Yc_i$ was obtained by *Eqn.* 4.17. where p and q have the same definition as in *Eqn.* 5.6.

To estimate the diameter of *MxG* stems, the relationship between depth and horizontal covered length per pixel is needed. This relationship was discussed in section 4.3.2.4 (Depth –horizontal covered length per pixel model).

The diameter of each *MxG* stem in pixel was estimated as:

$$dia\_pix_i = \max(X_k) - \min(X_k) \qquad k = 1, 2, \ldots \qquad (5.8)$$

Where $dia\_pix_i$ is the *MxG* stem diameter in pixels. $X_k$ , $k = 1, 2, ....$ is the horizontal coordinates of all the pixels in the $i^{th}$ connected area (*MxG* stem).

Thus, based on *Eqn.* 4.12, *Eqn.* 5.7 and *Eqn.* 5.8, the estimation of *MxG* stem diameter ( $dia_i$ ) can be calculated as:

$$dia_i = dia\_pix_i \cdot Z_i \cdot \frac{2\tan\frac{b}{2}}{M} \qquad (5.9)$$

Where M is the width of the image, and b is the horizontal field of view of the camera (as shown in *Fig.* 4.5)

## 5.4 Results and Discussion

The proposed method was evaluated in three sections: 1) Sensor unit geometry perspective model validation 2) Resolution analysis 3) Field evaluation, which are discussed below in sequence.

### 5.4.1 Sensor unit geometry perspective model validation

The sensor unit geometry model is the foundation of the method. To validate the model, 35 images of a flat surface board were taken at distance ranging from 30cm to 200cm with a increment of 5 cm. Examples of the images are shown in *Fig*. 5.3.

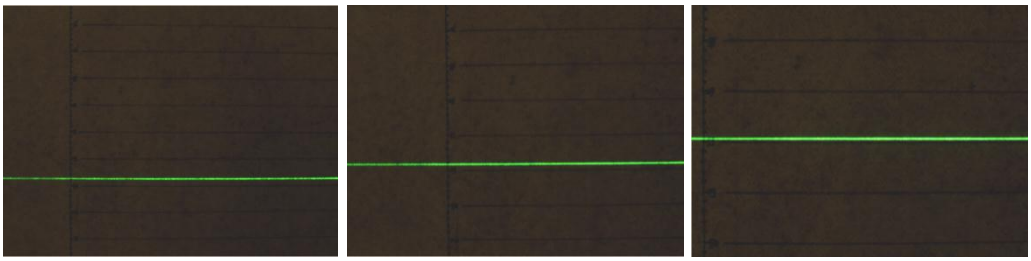

**Figure 5.3. The vertical location of the laser mark changes with the distance to the camera. The object is closer to the camera on the right side image.**

The vertical position of the laser sheet in each image was obtained based on the method mentioned in section 4.3.3 (Feature detection). The laser marks were detected using *Eqn*. 4.13, *Eqn*. 4.14 and *Eqn*. 4.15. One of the thresholds in *Eqn*. 4.16, T3, was set to infinity here. The average vertical position of largest connected area in the binary image was considered the vertical position of the laser sheet. *Tab*. 5.1 shows the relationship between the depth and the vertical position of the laser sheet.

**Table 5.1. Relationship between the depth and the vertical level of the laser mark.**

| | | | | | | | | | |
|---|---|---|---|---|---|---|---|---|---|
| **Depth (cm)** | 35 | 40 | 45 | 50 | 55 | 60 | 65 | 70 | 75 |
| **Vertical Level (pixel)** | 24.4 | 85.1 | 126 | 160 | 188.5 | 214.5 | 230.5 | 246.5 | 256 |
| **Depth (cm)** | 80 | 85 | 90 | 95 | 100 | 105 | 110 | 115 | 120 |
| **Vertical Level (pixel)** | 269 | 275.5 | 287 | 293 | 298.5 | 306 | 311.5 | 318 | 322.5 |
| **Depth (cm)** | 125 | 130 | 135 | 140 | 145 | 150 | 155 | 160 | 165 |
| **Vertical Level (pixel)** | 327 | 328.5 | 334 | 336.5 | 338 | 341 | 344 | 346.5 | 349.5 |
| **Depth (cm)** | 170 | 175 | 180 | 185 | 190 | 295 | 200 | | |
| **Vertical Level (pixel)** | 353.5 | 355 | 356 | 358 | 360 | 361.5 | 360.5 | | |

Based on the analysis in section 5.3.2, the relationship between depth and the vertical position of the laser sheet in the image should have the format shown in *Eqn*. 5.6. As shown in *Fig*. 5.4(a),

linear regression was applied to fit the points in *Tab*. 5.1 with a function, which has the form shown in *Eqn*. 5.6 with vertical level as X axis and depth as the Y axis. The fitted curve is:

$$Z = \frac{12720}{426.6 - \mathrm{x}} \qquad (5.10)$$

The regression coefficient of this estimation was 0.99.

Compared *Eqn*. 5.6 with *Eqn*.5.10, the following relationship exists.

$$\begin{cases} \mathrm{f} \cdot (\tan c + \tan \frac{a}{2}) = 426.6 \\ \mathrm{D} \cdot \mathrm{f} \cdot (\tan c + \tan \frac{a}{2}) = 12720 \end{cases} \qquad (5.11)$$

Then, D=29.82 cm, while the manually measured D was 29.48 cm. The similarity of geometry analysis and experimental result indicates that the geometry perspective model of the sensor unit is valid.

### 5.4.2 Resolution analysis

Since the horizontal covered length per pixel varies depending on depth, the estimated length resolution in the image also relied on depth. Based on the analysis in section 4.3.2.4 (Depth – horizontal covered length per pixel model). (*Fig.* 4.5), the depth and horizontal covered length per pixel follows a linear relationship. To validate this, the number of pixels of a 30mm length edge in 11 images (depth ranging from 20cm to 50 cm with an increment of 3cm) were counted. Subsequently, the horizontally covered length per pixel was calculated by dividing 30mm by the number of pixels. The result is shown in *Tab.* 5.2.

Linear regression was applied to fit the points shown in *Tab.* 5.2 (depth as x axis, covered length per pixel as y axis) as shown in *Fig.* 5.4(b). The estimated function for the horizontally covered length per pixel in average was shown as follows:

$$L_{h\_pixel} = 7.536\times10^{-4}\times Z + 0.040 \qquad (5.12)$$

The regression coefficient of this estimation was 0.99.

Comparing *Eqn.* 5.12 with *Eqn.* 4.12, an experimental value was obtained of $\frac{2\tan\frac{b}{2}}{M}$ in *Eqn.* 4.12 being $7.536\times10^{-4}$. The field of view (angle b) of the cameras was 26 degrees, and since the width of an image ($M$) was 640 pixels, the calculated value of $\frac{2\tan\frac{b}{2}}{M}$ is $7.215\times10^{-4}$. The experimental result and the theoretical result are similar, and therefore *Eqn.* 5.12 was applied as the relationship between depth and horizontally covered length per pixel. Thus, the resolution of the sensor unit follows *Eqn.* 5.12.

**Table 5.2. Measurements of covered length per pixel and the depth for the camera.**

| **Depth (mm)** | 200 | 230 | 260 | 290 | 320 | 350 | 380 | 410 | 440 | 470 | 500 |
|---|---|---|---|---|---|---|---|---|---|---|---|
| **Covered length per pixel of left camera (mm/pixel)** | 0.108 | 0.134 | 0.156 | 0.184 | 0.200 | 0.224 | 0.246 | 0.268 | 0.291 | 0.315 | 0.337 |

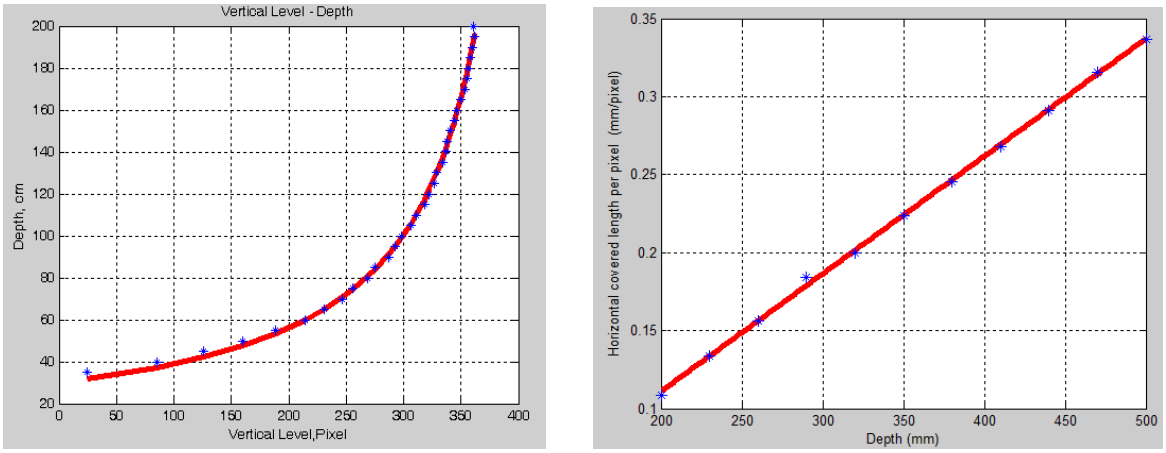


(a) (b)

**Figure 5.4. Relationships between depth, vertical position of the laser sheet and horizontally covered length per pixel. (a) Relationship between depth and the vertical position of the laser sheet in the image. (b) Relationship between depth and horizontally covered length per pixel.**

## 5.4.3 Field evaluation

To evaluate the performance of the developed diameter sensor, it was tested in a *MxG* field in Urbana, Illinois (lat/lon: 40.040963,-88.224565), during the fall of 2010 and spring of 2011. In 100 randomly selected images, diameters of 1,364 *MxG* stems were estimated. 150 *MxG* stems were randomly chosen from these 1,364 *MxG* stem diameter estimations, and the depths and diameters of the chosen *MxG* stems were manually measured as references. Figure 5.4 shows the depth estimation results.

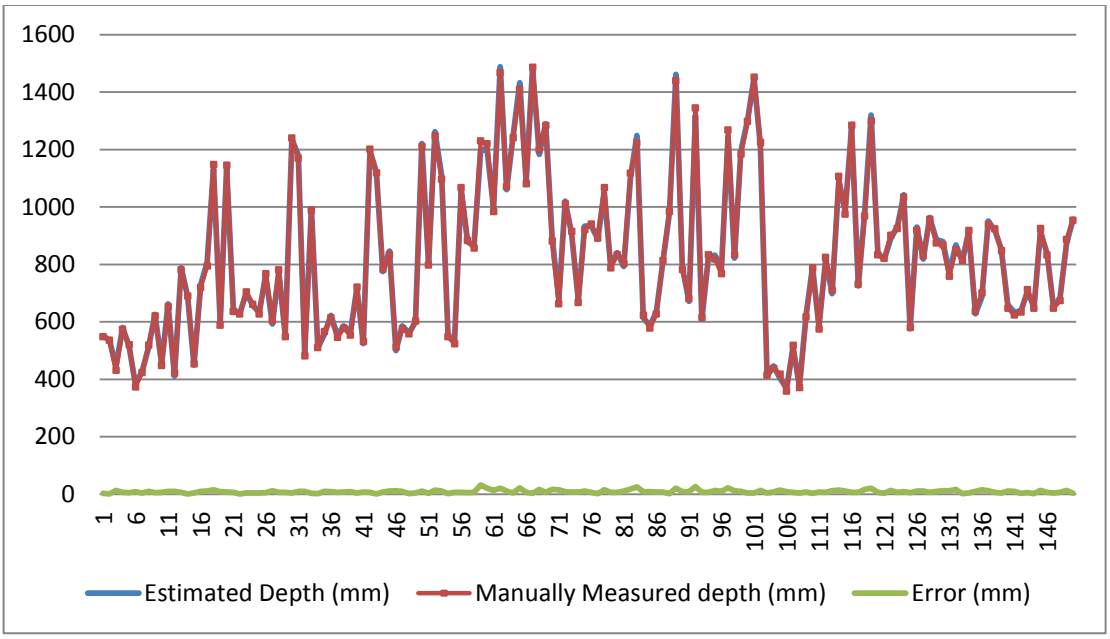


**Figure 5.5. Depth estimation result: the x-axis indicates the sample number of *MxG* stems, and the y-axis indicates the length in mm.**

The depths of the selected *MxG* stems ranged from 359mm to 1,486mm with an average of 822mm (based on manually measured depths). The errors between the estimated depth and the manually measured depth ranged from 1mm to 32mm with an average of 8.86mm and a standard deviation of 5.39mm. The geometry based depth estimation method achieved an accuracy of 98.92% (8.86mm as an average error) on average.

Similarly, *Fig.* 5.5 shows the results of the diameter estimation process. The diameters of selected *MxG* stems were in a range from 4.35mm to 13.57mm with an average of 8.57mm (based on manually measured diameters). The diameter estimation error ranged from 0.01 mm to 2.28mm with an average of 0.55mm and a standard deviation of 0.45mm. Thus, the individual diameter estimation of the proposed method achieved an accuracy of 93.5% (0.55mm average error). In addition, the average diameter of all selected *MxG* steam was 8.57mm, while the

average of the estimated *MxG* stem diameters was 8.51mm. Thus, the proposed method achieved an accuracy of 99.9% for average diameter estimation.

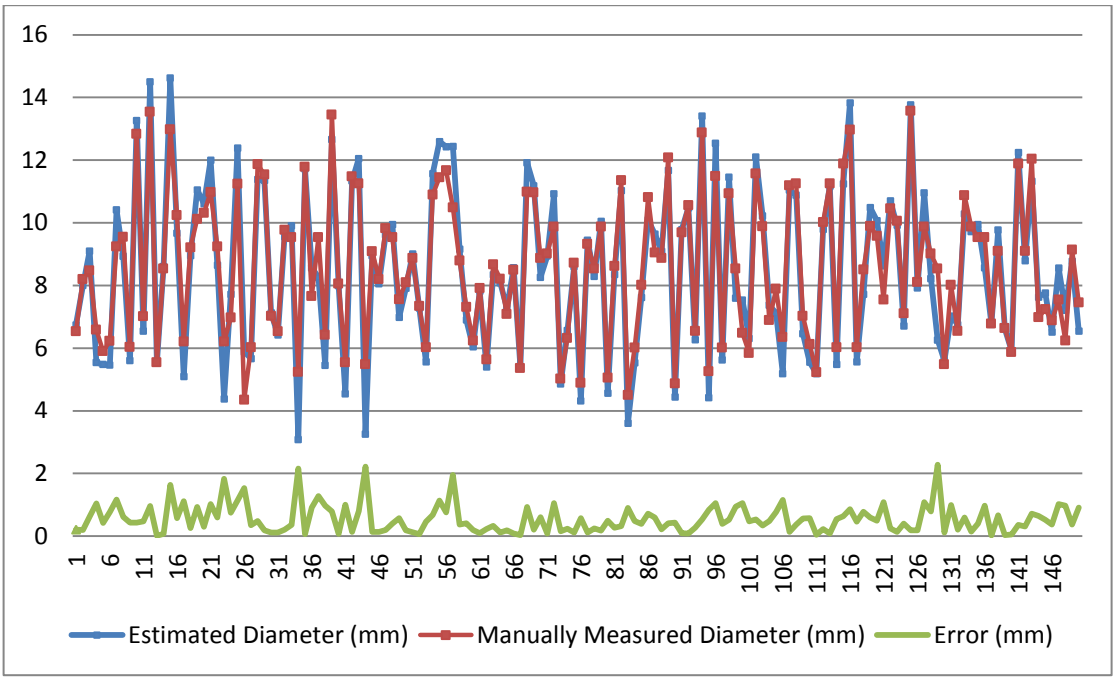


**Figure 5.6. Diameter estimation result: the x-axis indicates the sample number of *MxG* stems, and the y-axis indicates the length in mm.**

### 5.4.4 Diameter based yield model

*Eqn.* 1.1 shows that the total yield in a certain area is the production of average mass of individual *MxG* stems and the total number of stems in the area (as shown in *Eqn.* 2.12: $Y = \bar{W}_{indi} \times Num = H \times \pi(\frac{D}{2})^2 \times \rho \times Num$ ). In *Eqn.* 2.12 Y is the yield unit in $\frac{kg}{m^2}$ , $\bar{W}_{indi}$ is the average mass of *MxG* stems, $Num$ is the number of stems in a certain area, $D$ is the diameter of *MxG* stems, $H$ is the height of *MxG* stems, and $\rho$ is the material density of *MxG* stems. Then, the relationship between the individual mass and the stem diameter ( $D$ ) is quadratic. Diameters and masss of 130 *MxG* stems were measured manually to validate the relationship between

individual mass and stem diameter, and a quadratic function (*Eqn.*5.13) was applied to fit the collected sample points.

$$W_{indi} = f(D) = c_3 D^2 \quad (5.13)$$

Where $c_3$ is an unknown coefficient.

A quadratic curve was generated using linear regression:

$$W_{indi} = f(H) = 0.8763 D^2 \quad (5.14)$$

The regression coefficient of this estimation was 0.313, which means that it is not a good fit (*Fig.* 5.7(a)). The main reason is that the mass is more strongly dependent upon height than diameter. The diameters ranged from 5mm to 13mm, while the height ranged from 1m to 4m. Based on *Eqn.* 2.12, the yield and the stem volume ( $A = \frac{\pi}{4} D^2 H$ ) (the product of diameter squared, height and $\frac{\pi}{4}$) constitutes a linear relationship. Thus a linear function (*Eqn.* 5.15) was applied to model the relationship between yield and the stem volume.

$$W_{indi} = f(A) = c_4 A + c_5 \quad (5.15)$$

Linear regression yielded:

$$W_{indi} = f(A) = 5.194 \times 10^{-4} A + 0.5215 \quad (5.16)$$

The regression coefficient of this estimation was 0.72, which indicates a better fit (*Fig.* 5.7(b)) compared with the estimation shown in *Eqn.* 5.14. Thus, the yield and the stem volume of *MxG* exhibit a linear relationship.

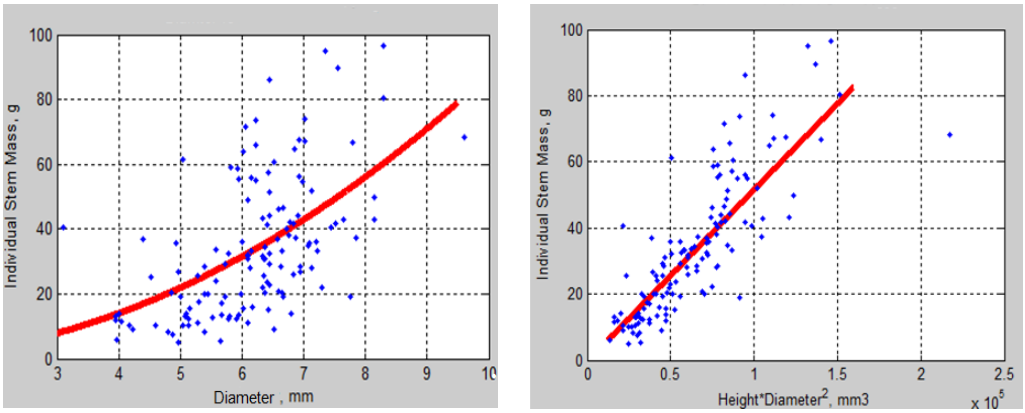


(a) (b)

**Figure 5.7. Relationships between individual mass and stem diameter and the stem volume. (a) Relationship between individual mass and *MxG* stem diameter. (b) Relationship between the individual mass and stem volume.**

## 5.5 Summary and Conclusions

A novel monocular stereo vision based *MxG* stem diameter sensor was developed. The sensor unit was composed of a Unibrain® Fire-i 701c color CCD camera and a 50mW laser sheet generator. A single camera was used to capture images, and the laser sheet was used to create identifiable features in the images. The sensor unit was configured and controlled by a laptop computer through a FireWire® interface.

The collected images were white balanced and converted into a RGB color space. Camera calibration was applied to correct for distortion in the images. A color segmentation method was developed to detect the features (laser spots). To extract the depth information of each feature, a geometrical perspective based method was developed and analyzed. Subsequently, a depth – horizontal covered length per pixel model was built to obtain the horizontal covered length per pixel based on the estimated depth. The diameter information was estimated based on the product of the size of each feature in pixels and the covered length per pixel.

The sensor unit geometry perspective model was validated by a series of experiments. The results showed that the models well represented the sensor unit geometry perspective. The proposed method was tested in the field as well. 150 *MxG* stems were randomly chosen from 100 images (1364 *MxG* stems), and their depths and diameters were measured manually as references. The results showed that the depth estimation method achieved an average accuracy of 98.9% (8.86mm average error). The diameter estimation sensor achieved an average accuracy of 93.5% (0.55mm average error) for individual *MxG* stem diameter estimation, while for average diameter estimation the achieved accuracy of the proposed method was 99.9%.

# CHAPTER 6
# A MACHINE VISION BASED CROP DENSITY SENSOR

## 6.1 Introduction

Crop density (stem/$m^2$) is considered a key factor to reflect the crop condition during the growing season, and to affect the yield of crops (Maertens *et al.*, 2003). Crop density sensors for *MxG* are currently not available. The objective of this research was to develop a high accuracy crop density sensor for *MxG*. The availability of a crop density sensor enables the development of a yield monitoring system, which is based on morphological information of *MxG* being stem diameter and height.

Crop density sensors for other crops are covered in the literature. Taylor *et al* (1986) reported a crop density measurement approach for a combine harvester. A laser beam was installed in front of the combine header, and the crop density was estimated by counting the interruptions of the beam. Similar research was done by Missotten (1998), where instead of a laser beam, an infrared light was applied. The sensor coverage area was calculated based on the width between the transmitter and receiver and the velocity. Similarly, Maertens *et al.* (2003) reported on an ultrasonic crop density sensor, where the sensor was placed on a wagon traveling on parallel

rails with plants between them. All the existing crop density sensors were designed for row crops, where the height of the crop was relative small. However, for *MxG*, neither a row structure nor a low height is present. Other crop density sensors measured crop density in indirect ways. Ehlert and Smith (1996) and Ehlert *et al.* (2004) applied a pendulum meter to measure the crop density. The pendulum will be pushed backwards by the plants and the proxy crop biomass density was obtained by measuring the push back angle. Saeys *et al.* (2009) developed a crop density sensor for small grains using a LIDAR sensor. The LIDAR scanned downwards towards the plants with a certain angle to measure the height of the plants based on detected ground level. The crop density was estimated based on height measurements. These methods provided only an approximate crop density estimation, because they measured the crop density indirectly, and are dependent upon the physical properties of the crop (Maertens *et al.*, 2003).

In this research, a machine vision based crop density sensor was developed. The main difficulty in applying machine vision system to predict the crop density of *MxG* is the occlusion of stems. A Monte Carlo model was applied to predict the number of invisible stems based on the number of detected visible stems in the image captured by the machine vision system. A Monte Carlo model is a numerical method to simulate a system with random inputs (Brown and Barnwell, 1987). Simulations were repeated using values of randomly selected parameters to determine the properties of a phenomenon (Fishman, 1995). The Monte Carlo method is widely used in agriculture: Hoff and Janni (1989) applied the Monte Carlo technique to determine the thermal radiation shape factors of six geometry configurations, and their result was within 2.2% of theoretically known shape factors. Hession *et al*. (1996) presented a two-phase Monte Carlo method to evaluate and propagate the natural stochastic variability and knowledge uncertainty

separately in hydrologic and water quality modeling. Similarly, Wei *et al*. (2008) developed a dual Monte Carlo method to analyze the predictive uncertainty, and further applied the method to a Rangeland hydrology and Erosion Model. Garg *et al*. (2009) proposed a physical hyper-spectral optical Monte Carlo model to compute the reflectance of water. Fraser *et al*. (2003) and Qin and Lu (2007) applied a Monte Carlo method to quantify light propagation of fruit.

The field distribution of *MxG* stems in the field can be considered a random distribution, and the diameters of the stems are also random variables. Then, a random variables (the locations of *MxG* stems and its diameters) involved system and the good performance of the Monte Carlo model output for systems with random components (Brown and Barnwell, 1987) justifies this technique to predict the crop density of *MxG*.

The developed sensor contains a machine vision system to detect the visible *MxG* stems, and a Monte Carlo model to predict the crop density in field. Field evaluation of the sensor showed an average accuracy of 92.2%.

## 6.2 Materials

The density sensor module applied in this chapter is the same as described in section 4.2 and section 5.2. It was composed of a commercial color CCD camera (Unibrain® Fire-i 701 c) and a laser sheet generator. The sensor module was configured and controlled by a host computer (A DellTM Studio 1555 laptop) through a FireWire® interface. The laser sheet was applied to provide features allowing identification of the *MxG* stems. It was composed of a 50mW 532nm laser source and a Fresnel lens, which produced a diverging laser sheet. Figure 4.1 shows the sensor module applied in this chapter. A Matlab®/C++ based image acquisition application was

developed to configure the sensor module and collect images. The captured images were in YCrCb color space with a resolution of 640x480 pixels in BitMap format.

## 6.3 Methodology

The difficulty of the *MxG* crop density estimation is the occurrence of occlusions, meaning that some *MxG* stems may be blocked by others. A method to predict the crop density based on the number of visible *MxG* stems in images is described in this chapter. The coverage area of the sensor was estimated using the geometry perspective of the sensor module (section 5.3.2, Geometry perspective analysis based depth estimation). *MxG* stems were detected and identified based on the methods described in section 4.3.1 (White balance and color space conversion) and section 4.3.3 (Feature detection). Based on the information obtained by the sensor, a Monte Carlo model was developed to predict the crop density, expressed in the number of stems per area.

### 6.3.1 Sensor coverage area calculation

Based on the analysis in section 5.3.2 (geometry perspective analysis based depth estimation), an image size of 640x480 pixels featured the coverage area ( S ) with:

$$S = \tan(\frac{b}{2})\left(\frac{p}{q-480} - \frac{p}{q-1}\right)^2 \qquad (6.1)$$

Where b is the horizontal field of view of the camera (as shown in *Fig.* 4.5). p and q are the same as in *Eqn.* 5.6.

Similarly, the visible area of the laser spots is:

$$S_L = \tan(\frac{b}{2})\left(\frac{p}{q - x_D} + \frac{p}{q - x_{D+R}}\right)\left(\frac{p}{q - x_D} - \frac{p}{q - x_{D+R}}\right) \quad (6.2)$$

Where $x_D$ and $x_{D+R}$ are the corresponding vertical locations in images, such as points E and F in *Fig.* 5.1.

### 6.3.2 Image processing based *MxG* stem identification

To predict the crop density, a total number of visible *MxG* stems in an image is required. The captured image was white balanced and converted into RGB color space from YCrCb color space based on the methods introduced in 4.3.1 (White balance and color space conversion). Then, the *MxG* stems were detected and identified by applying the method described in section 4.3.3 (Feature detection). There is a change in the method in this chapter compared to chapter 4. The threshold $T_2$ in *Eqn.* 4.15 was set as 5 instead of 50. This is because for crop density estimation both entirely visible stems and partially visible stems need to be detected. By decreasing the $T_2$, partially visible stems could be detected. Figure 6.1 compares the feature detection results of the same image (*Fig.* 5.2(a)) with different values of the threshold $T_2$, where the number of detected features was considered equal to the number of visible *MxG* stems.

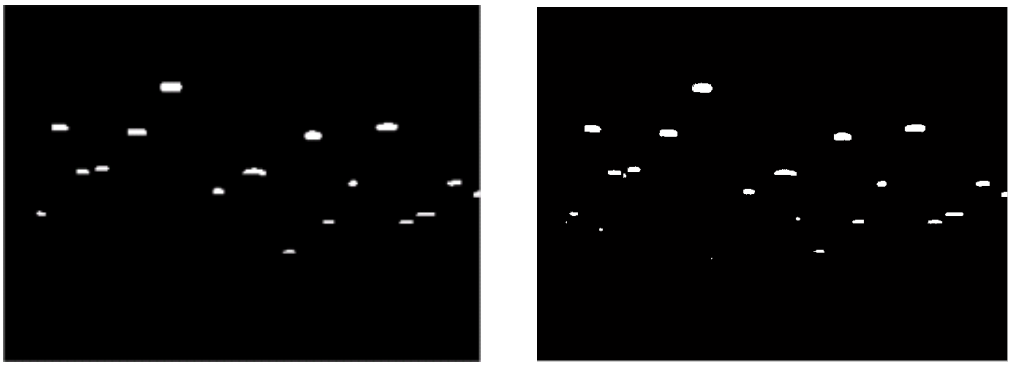

(a) (b)

**Figure 6.1. The value of $T_2$ effects the feature detection result. (a) Detected features with $T_2$ = 50. (b) Detected features with $T_2$ =5.**

### 6.3.3 Monte Carlo Model based crop density estimation

Assuming that the positions of *MxG* stems in the field follow a random distribution, it is possible to predict the number of blocked *MxG* stems based on the number of visible ones. To achieve this prediction, a Monte Carlo model based method was developed.

Based on *Eqn.* 6.2, the coverage area of the sensor is an isosceles trapezoid with an area of $\tan(\frac{b}{2})\left(\frac{p}{q-x_D}+\frac{p}{q-x_{D+R}}\right)\left(\frac{p}{q-x_D}-\frac{p}{q-x_{D+R}}\right)$. Given a crop density, *MxG* stems are randomly located since the x and y coordinates of the centers of the *MxG* stems were generated randomly in this area with randomly chosen diameters ranging from 5-15mm. Overlap of MxG stems was not allowed, and the location and diameter were regenerated if overlap occurred. Then, the number of visible *MxG* stems (including partially visible and entirely visible *MxG* stems) and the number of invisible *MxG* stems were computed as shown in *Fig.* 6.2. This process was repeated 100 times for crop densities ranging from 5 stem/$m^2$ to 500 stem/$m^2$. The relationship between

the number of visible *MxG* stems and the number of invisible *MxG* stems was obtained by the simulation result of the model.

$$Uvis = f(Vis) \qquad (6.3)$$

Where *Uvis* is the number of invisible *MxG* stems, and *Vis* is the number of visible *MxG* stems, which can be estimated based on the method described in section 6.3.2.

Then, the crop density can be estimated as:

$$Den = \frac{Vis + Uvis}{S_L} = \frac{Vis + Uvis}{\tan(\frac{b}{2})\left(\frac{p}{q - x_D} + \frac{p}{q - x_{D+R}}\right)\left(\frac{p}{q - x_D} - \frac{p}{q - x_{D+R}}\right)} \qquad (6.4)$$

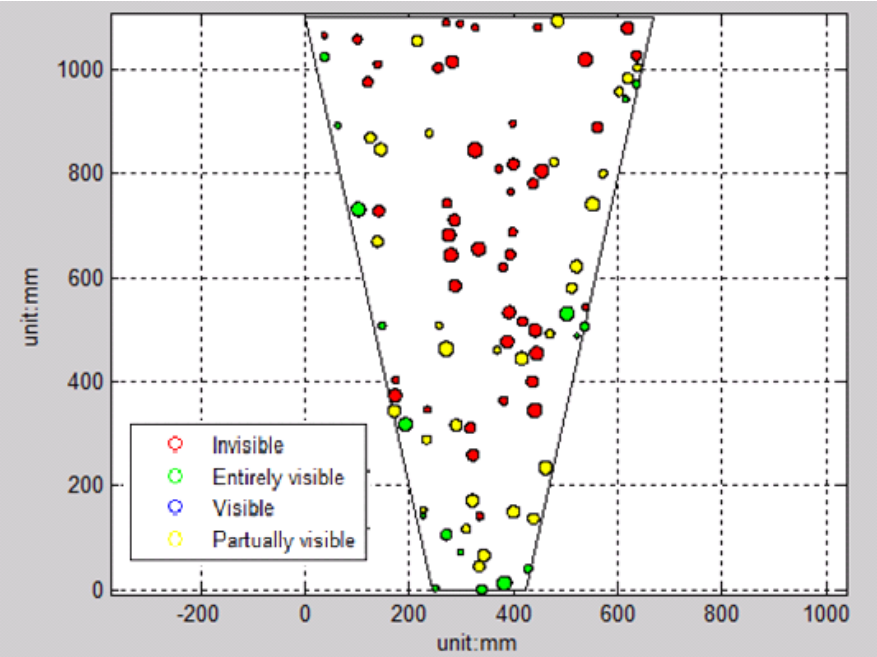


**Figure 6.2. *MxG* stem location simulation with a crop density of 200 stems/m$^2$. (top view) The spots in the figure represent MxG stems.**

## 6.4 Results and Discussion

The analysis and validation of the Monte Carlo model and the field evaluation are described in sequence in this chapter. The geometry perspective model of the sensor unit was analyzed and validated in section 5.4.1.

### 6.4.1 Analysis and validation of the Monte Carlo model

Figure 6.3 shows the Monte Carlo model. Figure 6.3(a) shows all the data points generated by the model (crop density ranging from 5 stems/$m^2$ to 500 stems/$m^2$). The green points denote entirely visible stems, yellow points denote partially visible stems, blue points are visible stems (the sum of the green and yellow points), and the red points represent invisible stems. For a certain crop density, the numbers (number entirely visible stems, partly visible stems, invisible stems) were not unique, but varied among subsequent simulation runs. However, they always fell into several ranges (around 20), and followed a random distribution overall. Figure 6.3(b) shows an example of histogram of the number of visible stems for 100 simulations for a crop density of 200 stems/$m^2$: the number of invisible stems has the same property. Thus, the mean value of the numbers for each crop density can be used to predict the crop density. Figure 6.3(c) shows the model represented by mean values of 100 simulations for each crop density. Based on the mean values, the percentages of visible stems (entirely visible and partly visible) and invisible stems are shown in *Fig.* 6.3(d).

To validate the model, the numbers of visible and invisible *MxG* stems in 10 images (randomly taken in the field) were manually counted, and compared with model predictions. The result is shown in *Tab.* 6.1.

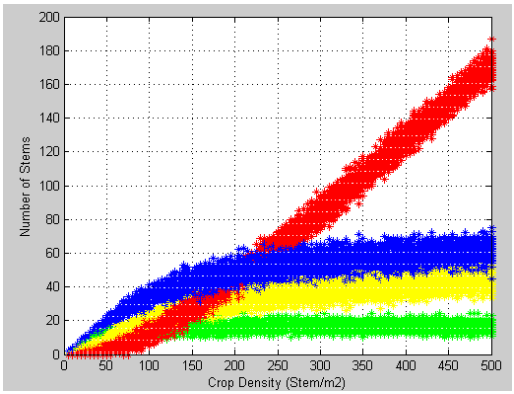


(a)

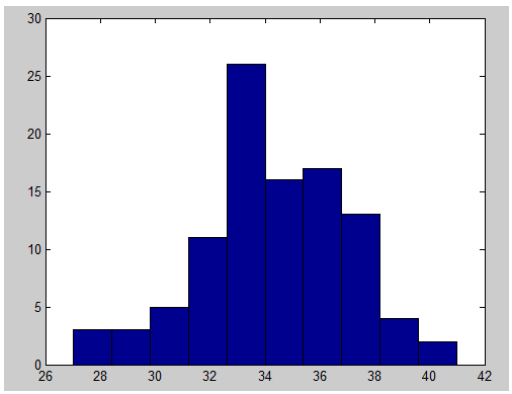

(b)

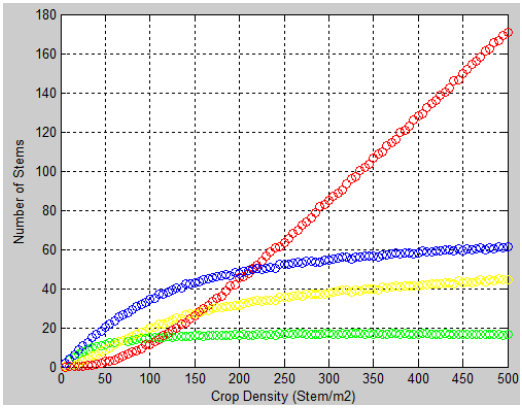


(c)

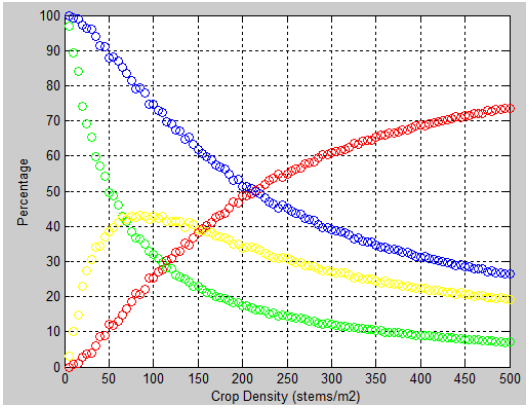


(d)

**Figure 6.3. Results of the Monte Carlo model simulation. (a) Monte Carlo model simulation representing all data points. (b) Histogram of visible stems for 100 simulations with a crop density of 200 stems/m$^2$. (c) Monte Carlo model representing mean values of 100 simulations for each crop density. (d) The Monte Carlo model representing the percentage of numbers (numbers of visible stems, entirely visible stems, partially visible stems and invisible stems). Green: entirely visible; Yellow: partially visible; Blue: visible; Red: Invisible.**

**Table 6.1. Validation of the Monte Carlo model.**

| **Density (stem/m2)** | | 53 | 43 | 28 | 62 | 46 | 62 | 51 | 67 | 71 | 65 |
|---|---|---|---|---|---|---|---|---|---|---|---|
| **Number of Visible stems** | **Manual Measurement** | 23 | 17 | 12 | 24 | 20 | 25 | 19 | 23 | 29 | 24 |
| | **Model Estimation** | 22.23 | 18.41 | 12.35 | 25.76 | 19.11 | 25.05 | 21.31 | 26.22 | 28.27 | 26.19 |
| **Number of Invisible stems** | **Manual Measurement** | 3 | 2 | 1 | 4 | 3 | 4 | 4 | 5 | 5 | 6 |
| | **Model Estimation** | 2.84 | 1.87 | 1 | 3.89 | 2.07 | 3.89 | 2.56 | 4.32 | 5.32 | 4.32 |

The error of the model estimation and manually counted result ranged from 0.05 to 3.22 stems for visible *MxG*, and from 0 to 1.68 stems for invisible *MxG*. Thus, the Monte Carlo model modeled the sensor and the field environment well.

The model is not robust when crop density is excessively high (above 200 stem/$m^2$), because a small change in the number of visible stems causes a large change in the number of invisible stems. Based on field measurements among 50 locations, the crop density (of three years old *MxG*) is lower than 100 stem/$m^2$ (73 stem/$m^2$ on average). Thus, the model is adequate among ranges found in the real field environment.

To predict the number of invisible stems, the relationship between the number of visible stems and the number of invisible stems is required. For each crop density, the mean value of the number of visible stems of 100 trails was used as the argument. Intervals of the 90% confidence for the number of invisible stems at each crop density were calculated as dependent variables. Since the Monte Carlo model was based on an assumption that the *MxG* stems were randomly distributed in field, the occurrences of *MxG* stems in the field constituted a Poisson process (Hall, 1988), which can be represented by exponential functions. Thus, a linear regression was applied to fit the points using experimental functions. Since for each crop density, the number of

invisible stems falls in an interval (90% confidence interval), the upper and lower boundaries of this interval were used as sample points to be fitted. Figure 6.4 shows the curve fitting results, where the blue curve fitted the lower boundary of the 90% confidence interval of the number of invisible stems, and the red curve fitted the upper boundary of the 90% confidence interval.

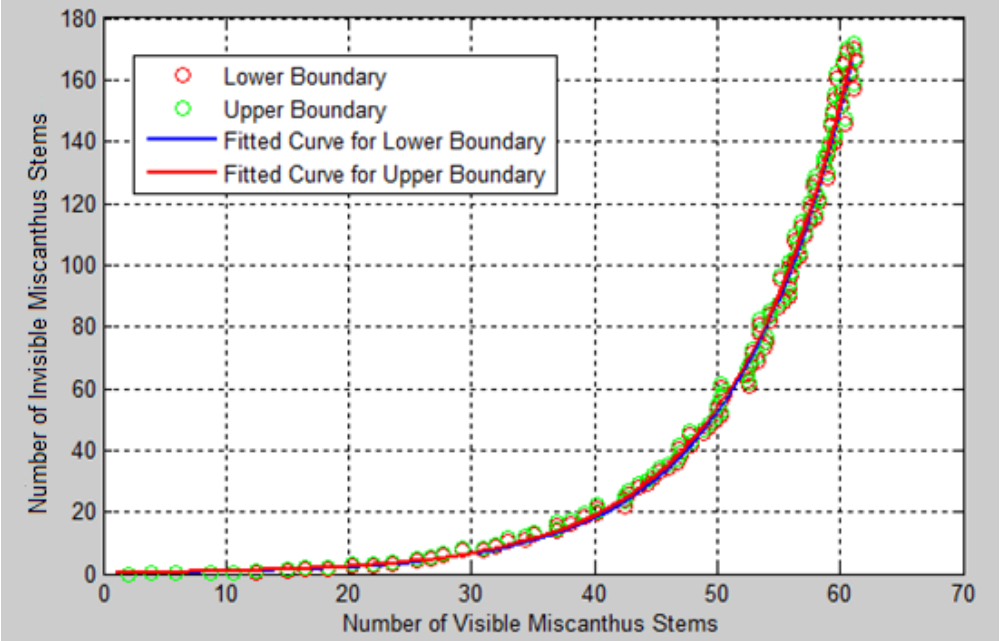


**Figure 6.4. Relationship between the number of visible stems and the number of invisible stems.**

*Eqn.* 6.5 and *Eqn.* 6.6 were the fitted functions of the lower boundary and upper boundary.

$$Uvis_L = 0.2695e^{0.1054 \cdot Vis} \quad (6.5)$$

$$Uvis_U = 0.3012e^{0.1037 \cdot Vis} \quad (6.6)$$

Where $Uvis_L$ and $Uvis_U$ are the lower boundary and the upper boundary of 90% confidence intervals of the number of invisible stems. Vis is the number of visible stems.

The crop density was predicted in an interval:

$$[Den_L, Den_U] = [\frac{Uvis_L + Vis}{S_L}, \frac{Uvis_U + Vis}{S_L}] \quad (6.7)$$

Where $Den_L$ and $Den_U$ are the lower and upper boundary of the estimated crop density. $S_L$ is the sensor coverage area based on *Eqn.* 6.2.

Since, the value calculated by *Eqn.* 6.5 and *Eqn.* 6.6 were close, the average ($Den$) of $Den_L$ and $Den_U$ is considered as an estimation of the crop density.

$$Den = \frac{Den_L + Den_U}{2} \quad (6.8)$$

### 6.4.2 Field evaluation

To evaluate the performance of the sensor unit, it was tested in a *MxG* field in Urbana, Illinois (lat/lon: 40.040963,-88.224565), during the Spring 2010, Fall 2010, and Spring 2011. 30 images were captured at randomly selected locations, and the crop densities at these locations were manually measured as references. The result is shown in *Fig.* 6.5.

The crop density of the selected locations ranged from 32 stem/m$^2$ to 92 stem/m$^2$ with an average of 57stems/m$^2$. The result of the field tests showed that the proposed method achieved an average accuracy of 91.20% with a minimum accuracy of 86.04%. To evaluate the impact of the crop density on the accuracy, the images were grouped in to three groups (10 images in each group) based on manually measured crop densities. The crop densities of the first group ranged from 32 stem/m$^2$ to 50 stem/m$^2$, and the achieved accuracy was 92.4%. The crop densities of the

second group ranged from 53 stem/$m^2$ to 61 stem/$m^2$, and this group achieved an accuracy of 91.4%. The crop densities of the third group ranged from 61 stem/$m^2$ to 92 stem/$m^2$, and the achieved accuracy of this group was 89.96%. Thus, the accuracy was inversely proportional to crop density.

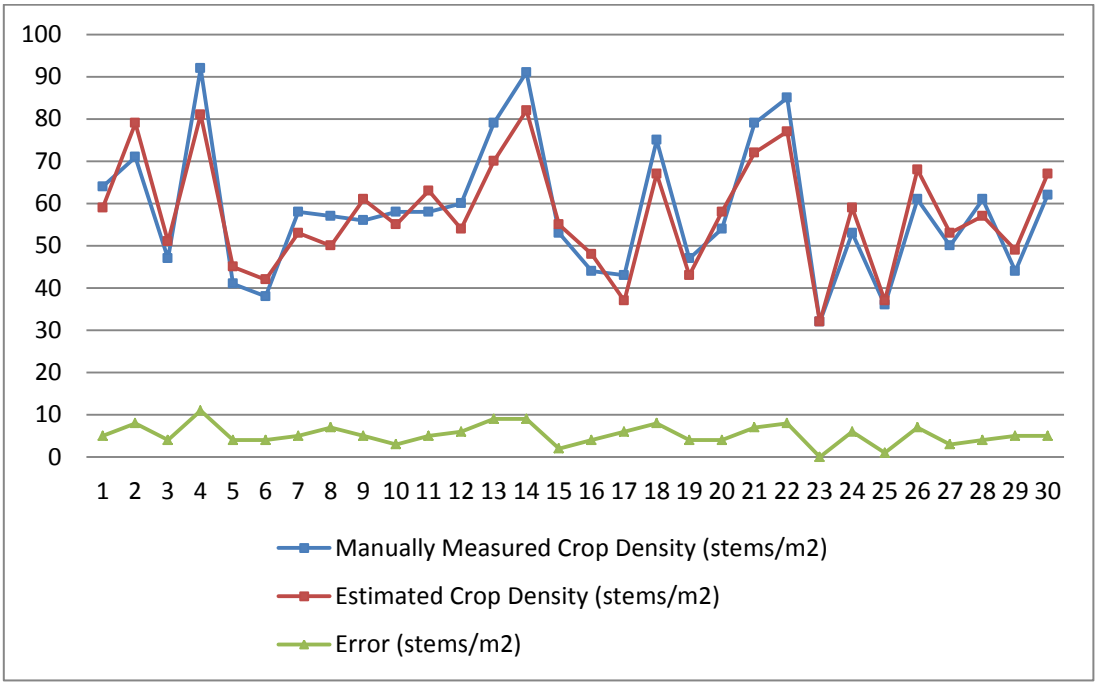


**Figure 6.5. Field evaluation result of the developed crop density sensor for *MxG*.**

### 6.4.3 Crop density based yield model

*Eqn.* 2.12: $Y = \bar{W}_{indi} \times Num = H \times \pi(\frac{D}{2})^2 \times \rho \times Num$ indicates that the relationship between the total mass in a certain area and the number of stems is linear. (In *Eqn.* 2.12 $Y$ is the yield unit in $\frac{kg}{m^2}$, $\bar{W}_{indi}$ is the average mass of *MxG* stems, $Num$ is the number of stems in a certain area, $D$ is the diameter of *MxG* stems, $H$ is the height of *MxG* stems, and $\rho$ is the material density of *MxG* stems). To validate this relationship, the mass of 130 *MxG* stems was manually measured,

and a linear function (*Eqn.* 6.9) was fitted to the relationship of total mass and the number of stems.

$$Y = f(Num) = c_6 Num \qquad (6.9)$$

Where $c_6$ is an unknown coefficient. The estimation (*Eqn.* 6.10) was obtained by linear regression:

$$Y = 35 Num \qquad (6.11)$$

The regression coefficient of this estimation was 0.99 (*Fig.* 6.6). The coefficient ($c_6$) indicates the average mass of individual *MxG* stems.

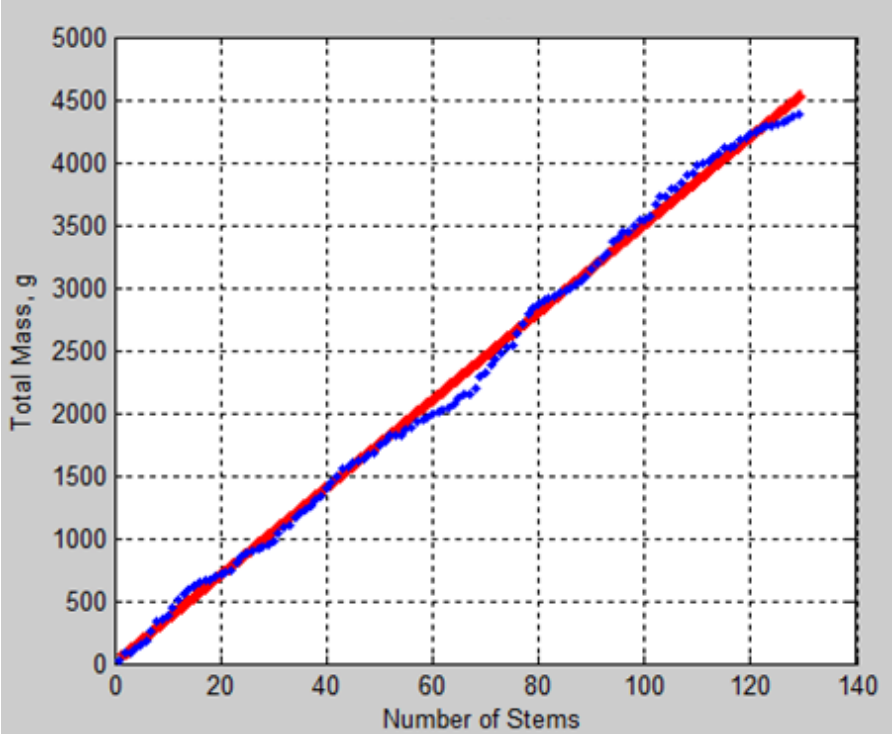


**Figure 6.6. Relationship between total mass and the number of stems.**

## 6.5 Summary and Conclusions

A machine vision and Monte Carlo model based crop density sensor was developed. The sensor unit was composed of a commercial color CCD camera (Unibrain® Fire-i 701c) and a laser sheet generator, consisting of a 50mW green laser beam and a Fresnel lens. The camera collected color images in the YCrCb color space, while the laser sheet provided identifiable features. A geometry perspective model of the sensor unit was developed and analyzed to calculate the sensor coverage area. An image segmentation based algorithm was developed to identify the features in images. To predict the crop density, a Monte Carlo model was proposed to predict the number of invisible *MxG* stems based on the number of visible *MxG* stems in images.

Both the geometry perspective model and the Monte Carlo model were validated using lab and field experiments. The field tests showed that the sensor achieved an average accuracy of 92.20% with a worst case of 86.04%. The results also showed that the accuracy is inversely proportional to the crop density. A crop density based yield model was discussed. The result showed that the total mass and the number of stems follow a linear function with the average mass of individual stems as the coefficient and zero intercept.

# CHAPTER 7
# SUMMARY AND FUTURE RESEARCH

## 7.1 Summary

Bioenergy is becoming one of the main sources of global sustainable development (Yamamoto *et al.*, 1999). It is also considered a solution to the problems of climate change and environmental damage from combusting fossil fuels (Michel *et al.*, 2011). Due to its ability to adapt to various soils and climates, low nutrition requirement and high yield, *Miscanthus Giganteus* (*MxG*) is considered one of the major energy crops worldwide (Lewandowski *et al.*, 2003; Clifton-Brown *et al.*, 2007; Michel *et al.*, 2011). Unfortunately, a yield monitoring system is not available for grassy energy crops like *MxG*. In this work, a yield monitoring system based on morphological parameters was developed. With the availability of a yield monitoring system detailed yield information can be obtained, the harvesting operation could be better organized and scheduled, and the yield data would make adaptive speed control of a harvester possible.

This research focused on the development of high accuracy morphological parameter sensors and corresponding algorithms for biomass yield estimation. The sensors were tested and evaluated in a field environment. The relationships between yield and morphological parameters (height, diameter and crop density) were discussed and analyzed.

The height of *MxG* was estimated using a LIDAR based measurement system. Two measurement modes, static and dynamic measurement, were tested. In static measurement mode, the position of the sensor was fixed, and the sensor worked in individual scan mode. In dynamic measurement mode, the LIDAR was configured to scan continuously, and the sensor traveled along the *MxG* field at a constant speed. An inclination correction algorithm was developed to improve the measurement accuracy of the sensor. The achieved average accuracy of the LIDAR base height sensor was 94.02% in static measurement mode, and 96.2% in dynamic height measurement mode compared to the manually measured heights. The relationship between individual stem mass and stem height was introduced and analyzed. The result showed that the yield and the height have a linear relationship.

The stem diameter was estimated using three approaches: LIDAR based diameter estimation, stereo vision system based and monocular vision system based diameter estimation. A LIDAR based approach was developed first. The LIDAR was placed to scan *MxG* stems horizontally. To identify the *MxG* stems in the raw LIDAR data, a region of interest was defined based on a measurement geometry model. The data within the ROI was pre-grouped by an angle continuity algorithm. Subsequently, a fuzzy clustering based method was applied to identify single stems based on the presentation of *MxG* stems in the LIDAR data. Four types of clusters were tested and different groups of cluster inputs were tested as well. The Gustafson-Kessel clustering algorithm was finally selected due to its best performance. To improve the measurement accuracy and implement the dynamic measurement of stem diameter, a binocular vision based diameter sensor was developed. Compared to a traditional binocular vision system, the sensor module developed applied a laser sheet to provide features (laser spots) on the stems. These features were used to identify the stems in images and match image pairs. The sensor

arrangement simplified the stem identification and image matching approach. The stem diameter was obtained by a disparity – depth model and a depth- horizontal covered length per pixel model. Both models were validated based on experiments. To further simplify the depth estimation in binocular stereo vision based diameter estimation approach, a monocular stereo vision diameter sensor was developed. It had the same sensor module as the binocular vision sensor, but only one image was required to estimate the stem diameters. The depth of each stem was estimated based on a geometry perspective model of the sensor. The results showed that the LIDAR based diameter sensor achieved an average accuracy of 92.5%, while the achieved average accuracy of binocular stereo vision based estimation and monocular stereo vision based estimation were 93.1% and 93.5% respectively. The relationship between individual mass and stem diameter was discussed. The result showed that the yield and the stem volume exhibit a linear relationship.

The comparison of three techniques applied to measure MxG stem diameter was shown in *Tab.* 7.1. The achieved accuracy of the stereo vision based and monocular based sensor were similar (stereo vision based sensor: 93.1% for individual stem diameter estimation and 99.8 % for average diameter estimation. Monocular vision based sensor: 93.5% for individual stem diameter estimation and 99.9% for average diameter estimation). Both of them support dynamic measurement. However, the monocular based sensor had a larger coverage area and lower computational cost. The achieved accuracy of the LIDAR based stem diameter sensor (92.5% for average diameter estimation) was lower than both stereo vision based and monocular based sensors. It also had the smallest coverage area of three sensors. The computational cost of the LIDAR based sensor was also high, and it did not support dynamic measurement. The device cost of LIDAR based sensor was around 5,000 to 6,000 U.S. dollar, while the device costs of

stereo vision and monocular based sensors were approximately 900 and 450 U.S. dollar. Thus, the monocular vision based stem diameter sensor was recommended in this research due to its higher accuracy, larger coverage area and lower cost in both computation and device.

**Table 7.1. Comparison of three sensors applied to measure MxG stem diameter.**

| | **Accuracy** | **Coverage Area** | **Computational Cost** | **Device Cost** | **Dynamic Measurement** |
|---|---|---|---|---|---|
| **LIDAR** | 92.5% | Small | High | High | No |
| **Stereo Vision** | 93.1% (99.8%) | Medium | High | Medium | Yes |
| **Monocular Vision** | 93.5% (99.9%) | Large | Low | Low | Yes |

Crop density was estimated using the same machine vision based diameter sensor. Thus, the stem diameter and crop density were obtained based on the same images. The sensor coverage area was calculated by the analysis of a perspective model of the sensor. The total number of *MxG* stems were predicted based on a Monte Carlo model. The model predicted the number of invisible stems based on the number of visible stems in images. The model was validated by comparing simulation and field measurements. The achieved average accuracy of the crop density sensor was 92.2%. The relationship between the total mass of *MxG* and the number of stems was discussed and analyzed. The result showed that the yield and the number of stems had a linear relation with zero intercept and the average individual mass as the coefficient.

In conclusion, the proposed yield sensing system achieved high accuracies of height, diameter and crop density estimations and provided a feasible solution for yield monitoring of *MxG*.

## 7.2 Future Research

Currently, the covered length of the dynamic LIDAR based height measurement was calculated by multiplying the operation time and the speed of the carrier. Its accuracy can be improved by a more accurate velocity sensor, for example, a gyroscope or a high accuracy encoder. Similarly, an accurate velocity sensor will make the dynamic measurement of LIDAR based diameter sensor possible.

Currently, the sensor system is mounted on a tractor using a steel frame (*Fig.* 7.1). The machine vision based sensor (diameter, crop density) suffered from vibrations at a relatively high velocity or on uneven surfaces due to the camera's low frame rate. A high-speed camera could reduce the influence of vibrations. In addition, a better designed sensor mount will improve the in-field stability and reduce vibrations.

Particularly for the machine vision based diameter sensor, an optimized algorithm for both binocular vision and monocular vision systems will decrease their computational cost, and increase the operational speed.


**Figure 7.1. The sensor mounted on a tractor by a cross steel frame.**

To produce yield maps, a GPS is recommended to be integrated with the current sensor system. Two sensor modules are applied in the current yield sensing system, LIDAR was applied to estimate the height, and a camera was employed to measure stem diameters and crop density. The availability of a diameter-height model could change the yield monitoring system to require only a machine vision based sensor, which is less expensive.

# REFERENCES


Annamalai, P., W. S. Lee, and T. F. Burks. 2004. Color vision system for estimating citrus yield in real-time. American Society of Agricultural Engineering (ASAE) Annual Meeting Paper Number: 043054.

Arthur, J. R., K. W. Charlotte, H. D. Brian, G. Britovsek, J. Cairney, A. C. Eckert, J. W. Frederick, Jr. P. J. Hallett, J. D. Leak, L. C. Liotta, J. R. Mielenz, R. Murphy, R. Templer and T. Tschaplinski. 2006. The path forward for biofuels and biomaterials. Science 311(5760): 484–489.

Babuška, R., P. J. van der Veen and U. Kaymak. 2002. Improved covariance estimation for Gustafson-Kessel clustering. Proceedings of the IEEE International Conference on Fuzzy Systems 2: 1081-1085.

Benjamin, C. E., P. M. Mailander, and R. R. Price. 2001. Sugar cane yield monitoring system. ASAE Annual Meeting Paper Number: 011189.

Bensaid, A. M., L. O. Hall, J. C. Bezdek, L. P. Clarke, M. L. Silbiger, J. A. Arrington and R. F. Murtagh. 1996. Validity-guided (Re) Clustering with applications to image segmentation. IEEE Transactions on Fuzzy Systems 4:112-123.

Becker, R. I., E. Vermote, M. Lindeman and C. Justice. 2010. A generalized regression-based model for forecasting winter wheat yields in Kansas and Ukraine using MODIS data. Remote Sensing of Environment 114(6): 1312-1323.

Bezdek, J. C. 1981. Pattern Recognition with Fuzzy Objective Function Algorithms. Plenum Press, MA, USA.

Bezdek, J. C. and J. C. Dunn. 1975. Optimal fuzzy partitions: A heuristic for estimating the parameters in a mixture of normal distrubutions. IEEE Transactions on Computers 8(24): 835-838.

Brosse, N., P. Sannigrahi and A. Ragauskas. 2009. Pretreatment of Miscanthus x Giganteus using the ethanol organosolv process for ethanol production. Industrial and Engineering Chemistry Research 48(18): 8328-8334.

Brown, D. C. 1966. Decentering distortion of lenses. Photometric Engineering 32(3): 444-462.

Brown, L. C. and T. O. Barnwell. 1987. The enhanced stream water quality models QUAL2E and QUAL2E-UNCAS: Documentation and user manual. NTIS Accession Number:PB87202156.

Buchsbaum, A. and H. Walter. 1975. Color TV Servicing. third edition. Englewood Cliffs, Prentice Hall, NJ, USA.

Bulanon, D. M., T. Kataoka, H. Okamoto and S. Hata. 2004. Determining the 3-D location of the apple fruit during harvest. Proceedings of ASAE International Conference on Automation Technology for Off-Road Equipment Paper Number: 701P1004.

Cai, J. and R. Walker. 2010. Height estimation from monocular image sequences using dynamic programming with explicit occlusions. IET Computer Vision 4(3): 149-161.

Chu, L., R. Masyuko, J. V. Sweedler and P. W. Bohn. 2010. Base-induced delignification of Miscanthus x Giganteus studied by three-dimensional confocal raman imaging. Bioresource Technology 101(13): 4919-4925.

Clifton-Brown, J. C., J. Breuer and M. Jones. 2007. Carbon mitigation by the energy crop Miscanthus. Global Change Biology 13(11): 2296-307.

Clifton-Brown, J. C. and I. Lewandowski. 2002. Screening Miscanthus Giganteus genotypes in field trials to optimise biomass yield and quality in southern Germany. European Journal of Agronomy 16(2): 97-110.

Criminisi, A., I. Reid and A. Zisserman. 2000. Single view metrology. International Journal of Computer Vision 40(2): 123–148.

Dammert, P. B. G. and J. Askne. 1998. Interferometric tree height observations in boreal forests with SAR interferometry. Proceedings of the IEEE International Geoscience and Remote Sensing Symposium 3: 1363-1366.

Delwiche, M. and J. Vorhees. 2003. Optoelectronic system for counting and sizing of field grown deciduous trees. Transactions of ASAE 46 (3): 877-882.

Domingos, G., P. Cerri and G. M. Paulo. 2005. Sugar cane yield monitor. ASAE Annual Meeting Paper Number: 051154.

Dunn, J. C. 1973. A fuzzy relative of the ISODATA process and its use in detecting compact well-separated cluster. Journal of Cybernetics 3(3): 32-57.

Durrence, J. S., C. D. Perry, G. Vellidis, D. L. Thomas and C. K. Kvien. 1998. Evaluation of commercially available cotton yield monitors in Georgia field conditions. ASAE Annual Meeting Paper Number: 983106.

Ehlert, D., J. Schmerler and U. Voelker. 2004. Variable rate nitrogen fertilisation of winter wheat based on a crop density sensor. Precision Agriculture 5(3): 263–273.

Ehlert, D. and H. Smith. 1996. Site-specific measuring of biomass in standing plant populations. Landtechnik 51(2): 86–87.

Fishman, G. S.. 1995. Monte Carlo: concepts, algorithms, and applications. Springer, New York.

Fraser, D. G., R. B. Jordan, R. Künnemeyer and V. A. McGlone. 2003. Light distribution inside mandarin fruit during internal quality assessment by NIR spectroscopy. Postharvest Biology and Technology 27(2): 185-196.

Fusiello, A., E. Trucco and A. Verri. 2000. A compact algorithm for rectification of stereo pairs. Machine Vision and Applications 12(1):16-22.

Garg, V., I. Chaubey and S. Singh. 2009. Evaluation of a hyperspectral optical Monte Carlo remote sensing model in a water tank study. Transactions of the American Society of Agricultural and Biological Engineering (ASABE) 52(3): 759-769.

Grift, T. E. 2003. Fundamental mass flow measurement of solid particles. Particulate Science and Technology 21(2): 177-193.

Grift, T. E., R. Ehsani, K. Nishiwaki, C. Crespi and M. Min. 2006. Development of a yield monitor for citrus fruits. ASAE Annual Meeting Paper Number: 061192.

Grift, T. E. and R. Oberti. 2006. Development of low-cost root collar diameter measurement devices for pine seedlings. Computers and Electronics in Agriculture 52(1-2): 60-70.

Gustafson, E. E. and C. W. Kessel. 1979. Fuzzy clustering with a fuzzy covariance matrix. IEEE Conference on Decision and Control 86(2): 761–766.

Hall, P. 1988. Introduction to the Theory of Coverage Processes. Wiley, New York.

Heikkilä, J. and O. Silven. 1997. Four-step camera calibration procedure with implicit image correction. In Proceedings of the IEEE Computer Society Conference on Computer Vision and Pattern Recognition: 1106-1112.

Hession, W. C., D. E. Storm and C. T. Haan. 1996. Two-phase uncertainty analysis: an example using the universal soil lossequation. Transactions of the ASAE 39(4): 1309-1319.

Hoff, S. J. and K. A. Janni. 1989. Monte carlo technique for the determination of thermal radiation shape factors. Transactions of the ASAE 32(3):1023-1028.

Ivanov, N., P. Boissard, M. Chapron and B. Andrieu. 1995. Computer stereo plotting for 3-D reconstruction of a maize canopy. Agricultural and Forest Meteorology 75(1-3): 85-102.

Jaakkola, A., J. Hyyppä, A. Kukko, X. Yu, H. Kaartinen, M. Lehtomäki and Y. Lin. 2010. A low-cost multi-sensoral mobile mapping system and its feasibility for tree measurements. Journal of Photogrammetry and Remote Sensing 65(6): 514-522.

Jin, J. and L. Tang. 2009. Corn plant sensing using color stereo vision. Journal of Field Robotics 26(6-7): 591-608.

Kwak, D., W. Lee, J. Lee, G. S. Biging and P. Gong. 2007. Detection of individual trees and estimation of tree height using LIDAR data. Journal of Forest Research 12(6): 425-434.

Lefsky, M. A., W. B. Cohen, W. B. Acker, G. G. Parker, T. A. Spies and D. Harding. 1999. LIDAR remote sensing of the canopy structure and biophysical properties of Douglas fir west hemlock forest. Remote Sensing of the Environment 70(3): 339-361.

Lewandowski, I., J. Clifton-Brown, J. Scurlock and W. Huisman. 2000. Miscanthus: European Experience with a Novel Energy Crop. Biomass & Bioenergy 19(4): 209-227.

Lin, T., W. Liao and C. Chien. 2001. 3D graphical modeling of vegetable seedlings based on a machine vision system. ASAE Annual Meeting Paper Number: 013137.

Liu, J., E. Pattry, J. Miller, H. McNairn, A. Smith and B. Hu. 2010. Estimating crop stresses, aboveground dry biomass and yield of corn using multi-temporal optical data combined with a radiation use efficiency model. Remote Sensing of Environment 114(6): 1167-1177.

Liu, Y., W. Chan and Y. Chen. 1995. Automatic white balance for digital still camera. IEEE Transactions on Consumer Electronics 41(3):460-466.

Lu, D.. 2006. The potential and challenge of remote sensing-based biomass estimation. International Journal of Remote Sensing 27(7-10): 1297-1328.

Maertens, K., P. Reyns, J. De Clippel and J. De Baerdemaeker. 2003. First experiments on ultrasonic crop density measurement. Journal of Sound and Vibration 266(3): 655–665.

Magnussen, S., P. Eggermonth, and V. L. Riccia. 1999. Recovering tree heights from airborne laser scanner data. Forest Science 45(3):407-422.

Matsumoto, Y., H. Terasaki, K. Sugimoto and T. Arakawa. 1997. Conversion system of monocular image sequence to stereo using Motion parallax. Proceedings of SPIE The International Society for Optical Engineering 3012: 108-115

McDonald, T. P., R. B. Rummer and T. E. Grift. 2003. Diameter sensors for tree-length harvesting systems. Proceedings of International Union of Forest Research Organisations The 2nd Forest Engineering Conference :45-54.

Missotten, B.. 1998. Measurement systems for the mapping and the evaluation of crop production Performance. Ph.D. Thesis. Department of Agro-Engineering and Economics, Katholieke Universiteit Leuven, Belgium.

Naidu, L. S., P. S. Moose, K. A. AL-Shoaibi, A. C. Raines, P. S. Long. 2003. Cold tolerance of C4 photosynthesis in Miscanthus x Giganteus: adaptation in amounts and sequence of C4 photosynthetic enzymes. Plant Physiology 132(3): 1688-1697.

Nilsson, M. 1996. Estimation of tree height and stand volume using an airborne LIDAR system. Remote Sensing of the Environment 56(1): 1-7.

Nishimoto, Y. and Y. Shirai. 1987. Feature-based stereo model using small disparities. Proceedings of IEEE Computer Society Conference on Computer Vision and Pattern Recognition: 192-196.

Orts, W. J., K. M. Holtman and J. N. Seiber. 2008. Agricultural chemistry and bioenergy. Journal of Agricultural and Food Chemistry 56(11): 3892–3899.

Pachidis, T. P. and J. N. Lygouras. 2007. Pseudostereo-vision system: a monocular stereo-vision system as a sensor for real-time robot applications. IEEE Transaction on Instrumentation and Measurement 56(6): 2547-2560.

Paine, L. K., T. L. Peterson, D. J. Undersander, K. C. Rineer, G. A. Bartelt, S. A. Temple, D. W. Sample and R. M. Klemme. 1996. Some ecological and socio-economic considerations for biomass energy crop production. Biomass and Bioenergy 10(4): 231–242.

Persson, Å., J. Holmgren and U. Söderman. 2002. Detecting and measuring individual trees using an airborne laser scanner. Photogrammetric Engineering and Remote Sensing 68(9): 925-932.

Popescu, S. C., R. H. Wynne and R. F. Nelson. 2003. Measuring individual tree crown diameter with LIDAR and assessing its influence on estimating forest volume and biomass. Canadian Journal of Remote Sensing 29(5): 564-577.

Poynton, C. A.. 1996. A technical introduction to digital video. Wiley, NJ, USA.

Price, R. R., J. Larsen and A. Peters. 2007. Development of an optical yield monitor for sugar cane harvesting. ASAE Annual Meeting Paper Number: 071049.

Qin, J. and R. Lu. 2007. Monte Carlo simulation of light propagation in apples. ASABE Annual meeting Paper Number: 073058.

Rovira-Más, F., Q. Zhang and F. J. Reid. 2008. Stereo vision three-dimensional terrain maps for precision agriculture. Computers and Electronics in Agriculture 61(2):133-143.

Saeys, W., B. Lenaerts, G. Craessaerts and J. De Baerdemaeker. 2009. Estimation of the crop density of small grains using LIDAR sensors. Biosystems Engineering 102(1): 22-30.

Sassenrath-Cole, G. F., S. J. Thomson, J. R. Williford, K. B. Hood, J. A. Thomasson, J. Williams and D. Woodard. 1999. Field testing of cotton yield monitors. Proceedings of National Cotton Council of American Beltwide Cotton Conference: 364-366.

Schmer, M. R., K. P. Vogel, R. B. Mitchell and R. K. Perrin. 2008. Net energy of cellulosic ethanol from switchgrass. National Academy of Sciences of the United States of America 105(2): 464–469.

Schueller, J. K., J. D. Whitney, T. A. Wheaton, W. M. Miller and A. E. Turner. 1999. Low-cost automatic yield mapping in manual-harvested citrus. Computers and Electronics in Agriculture 23(2): 145-154.

Shimada, M., Q. Muhtar, T. Tadono, H. Wakabayashi. 2001. Tree height estimation using an airborne L-band polarimetric interferometric SAR. Proceedings of IEEE International Geoscience and Remote Sensing Symposium 3: 1430-1432.

Smit, J., R. Kleihorst, A. Abbo, J. Meuleman and G. Willigenburg. 2004. Real time depth mapping performed on an autonomous stereo vision module. Proceedings of IEEE Program for Research on Integrated Systems and Circuits: 306-310.

St.-Onge, B., Y. Hu, C. Véga. 2008. Mapping the height and above-ground biomass of a mixed forest using lidar and stereo Ikonos images. International Journal of Remote Sensing 29(5): 1277-1294.

St.-Onge, B., J. Jumelet, M. Cobello, C. Véga. 2004. Measuring individual tree height using a combination of stereophotogrammetry and lidar. Canadian Journal of Forest Research 34(10): 2122-2130.

Sui, R., J. A. Thomasson, R. Mehrle, M. Dale, C. D. Perry and G. Rains. 2004. Mississippi cotton yield monitor: beta test for commercialization. Computers and Electronics in Agriculture 42(3): 149-160.

Takahash, T., S. H. Zhang and H. Fukuchi. 2002. Measurement of 3-D locations of fruit by stereo vision for apple harvesting in an orchard. Proceedings of the CIGR XVth World Congress: 1-10.

Taylor, R. K., M. L. Stone and H. W. Downs. 1986. Mapping yield potential with remote sensing. ASAE Annual Meeting Paper Number: 861619.

Technical Description Laser Measurement Systems LMS200 to LMS291, SICK® Inc., 2006.

Teoh, W. and X. Zhang. 1984. An inexpensive stereoscopic vision system for robots. Proceedings of IEEE International Conference on Robotics and Automation 3: 186–189.

Thomasson, J. A., D. A. Pennington, H. C. Pringle, E. P. Columbus, S. J. Thomson and R. K. Byler. 1999. Cotton mass flow measurement: experiments with two optical devices. Applied Engineering in Agriculture 15(1): 11-17.

Thomasson, J. A. and R. Sui. 2003. Mississippi cotton yield monitor: Three years of field test results. Applied Engineering in Agriculture 19(6): 631-636.

Thomasson, J. A., and R. Sui. 2004. Optical-reflectance-based mass-flow sensor. Patent Number. 6,809,821. Washington, D.C., USPTO.

Thomasson, J. A., R. Sui, G. C. Wright, A. J. Robson. 2006. Optical peanut yield monitor: development and testing. Applied Engineering in Agriculture 22(6): 809-818.

Tilman, D., J. Hill and C. Lehman. 2006. Carbon-negative biofuels from low-input high diversity grassland biomass. Science 314(5805): 1598–1600.

Tsai, R. Y. 1987. A versatile camera calibration technique for high accuracy 3D machine vision metrology using off-the-shelf TV cameras and lenses. IEEE Journal on Robotics Automat 3(4): 323-344.

Ulander, L. M. H. And J. O. Hagberg. 1995. Measuring tree height using ERS-1 SAR interferometry. Proceedings of the IEEE International Geoscience and Remote Sensing Symposium 3: 2189-2193.

Van der Zande, D., W. Hoet, I. Jonckheere, J. van Aardt, P. Coppin. 2006. Influence of measurement set-up of ground-based LIDAR for derivation of tree structure. Agricultural and Forest Meteorology 141(2-4): 147-160.

Vellidis, G., C. D. Perry. G. Rains, D. L. Thomas, N. Wells and C. K. Kvien. 2003. Simultaneous assessment of cotton yield monitors. Applied Engineering in Agriculture 19(3):259-272.

Wang, S. and K. Ishii. 2009. Depth perception using a monocular vision system. Lecture notes in computer science (including subseries Lecture Notes in Artificial Intelligence and Lecture Notes in Bioinformatics) 5506 LNCS (PART 1): 779-786.

Wei, H., M. A. Nearing, J. J. Stone and D. D. Breshears. 2008. A dual Monte Carlo approach to estimate model uncertainty and its application to the rangeland hydrology and erosion model. Transactions of the ASABE 51(2): 515-520.

Weng, C. -C., H. Chen, and C. -S. Fuh. 2005. A novel automatic white balance method for digital still cameras. Proceedings of the IEEE International Symposium on Circuits and Systems 4: 3801 – 3804.

Whitney, J. D., Q. Ling, W. M. Miller and T. A. Wheaton. 2001. A DGPS yield monitoring systems for Florida citrus. Transactions of the ASAE 17(2): 115-119.

Wolak, F. J., A. Khalilian, R. B. Dodd, Y. J. Han, M. Keshlkin, R. M. Lippert and W. Hair. 1999. Cotton yield monitor evaluation, South Carolina – year 2. Proceedings of National Cotton Council of American Beltwide Cotton Conference: 361-364.

Xie, X. L. and G. A. Beni. 1991. Validity measure for fuzzy clustering. IEEE Transaction of PAMI 3(8):841-846.

Yamamoto, K., T. Takahashi, Y. Miyachi, N. Kondo, S. Morita, M. Nakao, T. Shibayama, Y. Takaichi, M. Tsuzuku and N. Murate. 2010. Estimation of mean tree height using small-footprint airborne LIDAR without a digital terrain model. Journal of Forest Research: 1-7.

Zhang, Z. 1999. Flexible camera calibration by viewing a plane from unknown orientations. Proceedings of IEEE International Conference on Computer Vision: 666-673.

Zhao, H. and J. K. Aggarwal. 2000. 3-D reconstruction of an urban scene from synthetic fish-eye images. Proceedings of the 4th IEEE Southwest Symposium on Image Analysis and Interpretation: 219-223.

Zub, H.W., S. Arnoult and M. Brancourt-Hulmel. 2011. Key traits for biomass production identified in different Miscanthus Giganteus species at two harvest dates. Biomass and Bioenergy 35(1): 637-651.

# VITA

Lei Zhang was born on June 11, 1982 in Harbin, the city of ice and snow, Heilongjiang, China. He earned his B. Eng. degree in 2005 and his M. Eng. degree in 2007 both in Electronic Engineering from Harbin Institute of Technology. His completed his undergraduate project in the research of joint source-channel coding algorithm of JPEG2000. He completed his Master research project in embedded system based motion JPEG 2000 image and video compression system.

In Fall 2007, Lei decided to come to the University of Illinois at Urbana- Champaign to pursue a Ph.D. degree instead of being a researcher in Department of satellite application, China Academy of Space Technology. During working as a research assistant in the department of Agricultural and Biological Engineering, he worked as a teaching assistant for four courses. His doctoral research is focused on the development of a yield monitoring system for *Miscanthus Giganteus*. Lei holds a certification of electronic laboratory from Rockwell Co. and Fundamental teaching certification from university of Illinois at Urbana- Champaign.

Following the completion of his Ph.D., Lei will begin his career in Microsoft Co. as a software developer engineering of its search engine team in on-line serveries division